ReactorSTM : imaging catalysts under realistic conditions

Herbschleb, C.T.

ReactorSTM

Imaging Catalysts under Realistic Conditions

Proefschrift

ter verkrijging van
de graad van Doctor aan de Universiteit Leiden,
op gezag van Rector Magnificus prof. mr. P.F. van der Heijden,
volgens besluit van het College voor Promoties
te verdedigen op dinsdag 10 mei 2011
klokke 10:00 uur

door

Cornelis Thaddeus Herbschleb

geboren te Leeuwarden
in 1983

Promotiecommissie:

Promotor:	Prof. Dr. J.W.M. Frenken	Universiteit Leiden
Leden:	Prof. Dr. I. Chorkendorff	Danmarks Tekniske Universitet
	Prof. Dr. S. Speller	Radboud Universiteit Nijmegen
	Prof. Dr. J.M. van Ruitenbeek	Universiteit Leiden
	Prof. Dr. B.E. Nieuwenhuys	Technische Universiteit Eindhoven
	Prof. Dr. J.W. Niemantsverdriet	Technische Universiteit Eindhoven
	Dr. B.J. Nelissen	Albemarle Catalysts BV.

The work described in this thesis was performed at the Kamerlingh Onnes Laboratory, Leiden University, P.O. Box 9504, 2300 RA Leiden. This research has been financially supported firstly by NanoNed, a technology program of the Dutch Ministry of Economic Affairs via the foundation STW (www.nanoned.nl), and secondly by NIMIC, part of the SmartMix program (www.realnano.nl).

ISBN 978-90-8593-098-3
Casimir PhD series, Delft-Leiden, 2011-8

"We are the music makers, and we are the dreamers of dreams"

- Arthur O'Shaughnessy (1874)

Contents

Chapter 1

Introduction

One of the driving forces behind our modern society is the phenomenon of catalysis. Catalysts are, for instance, applied in the pharmaceutical industry and petrochemical industry to produce clean and specific products. Another important application is the field of pollution control, for example to reduce the emission of hazardous gases from vehicles and power plants. The development of the modern use of catalysts was initiated in the early nineteenth century by Kirchhoff, H. Davy, E. Davy, Döbereiner and Faraday, who were the first ones to study this phenomenon, in which chemical reactions were aided by the presence of other materials, which were not consumed in the process. Twenty years after its initial reporting, it was Berzelius who in 1836 named this phenomenon as "catalysis" [1]. The second half of the nineteenth century was filled with discoveries, and the development of numerous catalysis based reaction systems; an example is the Deacon process (1860), in which Cl_2 was produced from HCl, over a $CuCl_2$ catalyst [2, 3]. The first big industrialized and researched catalytic system was for the synthesis of NH_3, an important basic ingredient for making fertilizers. The research led, in particular, to the introduction of high-pressure reactors, in order to shift the chemical equilibrium of the NH_3 synthesis reaction towards higher product yield. During the same period, science became involved in catalysis, and began studying, for instance, the active sites of a catalyst, the sticking probability of molecules on a catalyst surface, and the kinetic mechanisms of catalytic systems. The increasing use of fuel during the twentieth century, and consciousness about the necessity of controlling the composition of the gases emitted into the atmosphere, to decrease our impact on the environment, have led to the exponential development of catalysts, as well as the development of the research field of catalysis worldwide. To emphasize the importance of this research field, Gerhard Ertl was awarded the Nobel Prize in chemistry in 2007, for his work in this field [4].

The work I present in my thesis adds knowledge and interpretation to a subsection of the wonderful and indispensable phenomenon of catalysis. This first chapter gives an overview of the theory behind catalysts, the different research techniques which engage our increasing fundamental understanding of catalysts, a short introduction to crystallography, as well as the ins and outs of the specific technique I used (Scanning Tunneling Microscopy (STM)) during my research.

1.1 Catalysts: theory and experiment

1.1.1 Catalysis

A catalyst is defined as a material which is directly and actively involved in accelerating a selected chemical reaction, without being consumed itself. It can accelerate a chemical reaction by lowering the activation energies involved in this reaction, which is schematically shown in figure 1.1. The catalyst can lower the activation energy by providing alternate pathways for a reaction to take place, e.g. by enabling adsorption, diffusion, and chemical rearrangements of reactants, and desorption of the reaction products. Next to just accelerating a reaction, the catalyst also has to be selective, i.e. it should only lower the energy barriers for the desired reaction to occur.

Catalysis can be divided in two categories: homogeneous and heterogeneous catalysis. In the former case, both the catalyst and the reactants are in the same phase. Examples of this type of catalysis are the hydroformylation of alkenes into aldehydes, which are an important basic product for many detergents (liquid phase) [7], and the decomposition of ozone in the atmosphere by halogenoid radicals (gas phase) [8]. Yet the vast majority of catalyzed reactions fall within the scope of heterogeneous catalysis, in which reactants and catalyst are in different phases. In most heterogeneously catalyzed reactions, liquid or gaseous reactants react on the surface of a solid catalyst. Therefore, the key to understanding how heterogeneous catalysis works is to understand how the surface behaves, under the presence of the reactants, at pressure p and temperature T. The reactivity of a catalyst scales directly with the number of active sites, and since many of the catalyst materials consist of precious transition metals, in industry the catalysts generally are dispersed as nano-particles on a porous grid, made out of a cheap support material (e.g. Al_2O_3), in order to optimize the surface-to-volume ratio. The production of plastics, medicines, and fuels are well-known examples

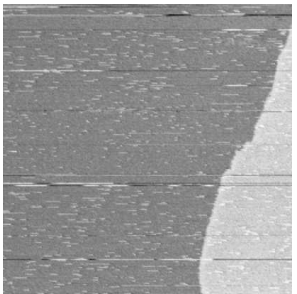

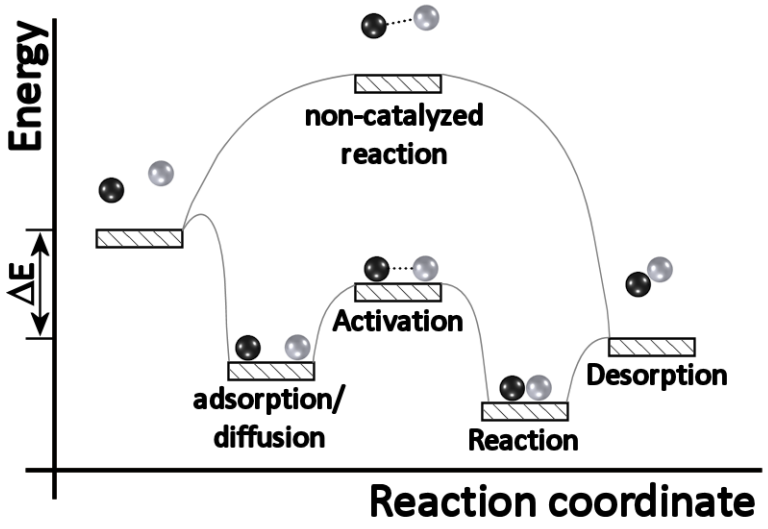

Figure 1.1: Schematic energy diagram for a catalyzed and non-catalyzed reaction. ΔE is the energy gained by the total reaction.

of heterogeneous catalysis; this work consists solely of heterogenic catalytic systems.

The main field of catalysis, on which this thesis is built, is the field of minimizing our environmental impact, while combusting fuels in transportation. This can be approached from two directions. The *ingoing* fuel can be cleaned as well as possible by, for instance, catalytic removal of sulfur (chapter 5) and nitrogen from carbon hydrates containing these elements. Catalytic removal of hazardous gases from the *outgoing* exhaust gas composition, after the fuel has been combusted in the engine, is the other option. The typical gas composition, from the exhaust of a spark ignition engine in a car, consists of three types of compounds: (1) oxidant chemical compounds (O_2, NO_x), (2) reducing chemical compounds (CO, H_2, unburnt hydrocarbons), and (3) other compounds (N_2, H_2O, CO_2) [9]. The three-way catalyst of a car exploits three reactions: NO_x reduction (chapter 3), CO oxidation (chapter 4), and oxidation of unburnt hydrocarbons.

1.1.2 Langmuir theory of adsorption

During a catalyzed chemical reaction, one or more of the reactants form a bond to the surface of the catalyst by a process called adsorption. There are two kinds of adsorption: associative and dissociative adsorption. For the

latter, the adsorbate molecule splits when bonded to the surface, whereas for associative adsorption, it does not. The theory of gases adsorbed on a solid surface at equilibrium can be described by the Langmuir theorem of adsorption. In this theory, a combination of assumptions has been made:

- The solid surface is uniform, and consists of equivalent sites, which can be occupied by only one gas molecule.
- The equilibrium between the gas and adsorbate state is dynamic.
- When a gas molecule collides with the surface and hits an empty site, it is bonded; otherwise it is reflected.
- Adsorbed molecules are localized.

The fractional coverage of the surface ϑ depends on the number of occupied sites N_S and the total number of sites N: $\vartheta = \frac{N_S}{N}$. Since in our experiments, we control the fractional coverage of gas M by altering the pressure of the gas offered to the surface, it is instructive to write the dependence of ϑ on the pressure p. For determining the fractional coverage of associative adsorption, we first write down its general reaction between surface and gas, $M_{(g)} + * \rightleftharpoons M_{(ads)}$. Here $*$ stands for a free site on the surface, and $M_{(ads)}$ is the complex of the adsorbed molecule and the site it occupies. From the reaction equation, we can determine the adsorption rate A and the desorption rate D: $A = k_a p(1-\vartheta)$, in which k_a is the adsorption rate constant and $(1-\vartheta)$ the relative density of free sites on the surface; $D = k_d\vartheta$, in which k_d is the desorption rate constant. At equilibrium $A = D$, so that $\vartheta(p)$ reads

$$\vartheta = \frac{Kp}{1+Kp}, \tag{1.1.1}$$

in which K is the equilibrium constant defined by $\frac{k_a}{k_d}$, and in this case can be interpreted as the affinity of the molecules for the surface: when K increases, k_a gets larger relative to k_d, implying that adsorption becomes more favorable than desorption. Equation 1.1.1 is called the Langmuir adsorption isotherm, and predicts how the fractional coverage changes with the pressure.

In the same way, the Langmuir adsorption isotherm for dissociative adsorption can be determined. Let us consider the example of a homonuclear, diatomic molecule M_2. In this case, the reaction equation is given by $M_{2\ (g)} + 2 * \rightleftharpoons 2\ M_{ads}$, yielding adsorption rate $A' = k'_a p(1-\vartheta)^2$ and desorption rate $D' = k'_d\vartheta^2$. Following the same calculation as for associative adsorption, the Langmuir dissociative adsorption isotherm becomes

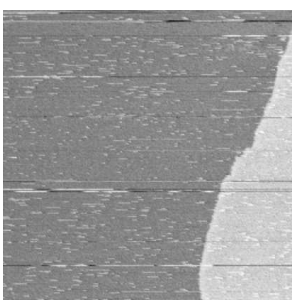

$$\vartheta = \frac{\sqrt{K'p}}{1+\sqrt{K'p}}. \tag{1.1.2}$$

At low pressures, $K^{(')}p \ll 1$, resulting in the linear expression $\vartheta(p) = K^{(')}p$, which is known as Henry's law. If we look at the extreme $p \to \infty$, we obtain $\vartheta = 1$, implying that at elevated pressures, which is our working domain, the solid surface will be completely covered by a monolayer of adsorbed gas molecules.

1.1.3 Reaction mechanisms

Investigations on adsorption and desorption of gas molecules at a catalytically active surface, and interaction of these molecules with each other on this surface, as well as with the surface itself, have yielded various reaction mechanisms. The main reaction mechanisms, two of which are also encountered in this work, are shown in figure 1.2.

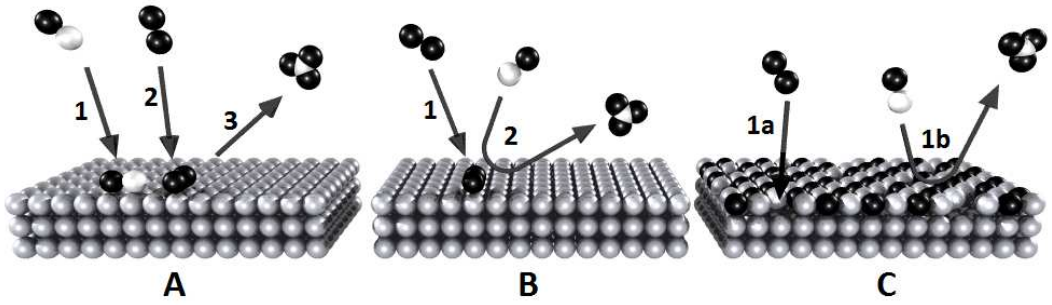

Figure 1.2: (A) Langmuir-Hinshelwood mechanism, (B) Eley-Rideal mechanism, (C) Mars-Van Krevelen mechanism

Part A in figure 1.2 shows the Langmuir-Hinshelwood mechanism. In this reaction mechanism, both reactants first adsorb onto the surface (reaction 1 and 2), before a reaction takes place. Surface diffusion facilitates interaction between adsorbed molecules; the reaction product desorbs from the surface (reaction 3). Generally, the reaction rate between adsorbent 1 and 2 is given by $R_{LH} = k\vartheta_1\vartheta_2$, provided that the reaction at the surface is the rate limiting step, in which k is the reaction constant. Its dependence on the pressure is given in equation 1.1.3, which is derived from the Langmuir adsorption isotherm derived in section 1.1.2.

$$R_{LH} = k\frac{K_1p_1 \cdot K_2p_2}{(1+K_1p_1+K_2p_2)^2}. \tag{1.1.3}$$

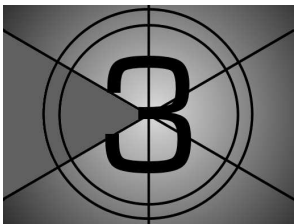

In this type of mechanism, the reactivity is highest when a stoichiometric amount of reactant is adsorbed on the surface, and both reactants are fully dispersed over the surface. The vast majority of catalytic reactions follow this mechanism. An example is the reduction of NO by CO on Pt(100), which is described in detail in chapter 3.

A second mechanism, the Eley-Rideal mechanism, is shown in part B of figure 1.2. In this case, only one of the reactants adsorbs onto the surface (reaction 1), after which the other reactant interacts with the adsorbed species directly from the gas phase, followed by the desorption of the reaction product (reaction 2). The reaction rate is therefore given by $R_{ER} = k\vartheta_1 p_2$, which translates to equation 1.1.4 if we substitute the Langmuir adsorption isotherm.

$$R_{ER} = k\frac{K_1 p_1}{1 + K_1 p_1} p_2. \tag{1.1.4}$$

A higher coverage of the adsorbed species, as well as a higher pressure of the other gas, yields a higher reaction rate. An example of a reaction following the Eley-Rideal mechanism is the hydrogenation of CO_2 during formate synthesis [25], in which H_2 is the adsorbed species.

Finally, in part C of figure 1.2, the Mars-Van Krevelen mechanism is depicted. In this mechanism, the surface itself is an active part in the reaction: one reactant forms a chemical bond with the catalytic surface (reaction 1a), forming a thin surface layer of Metal-Reactant. Examples are metal oxides, carbides, and sulfides. The other reactant now reacts directly from the gas phase with the atoms from the chemically bonded reactant on the surface (reaction 1b), yielding a reaction rate of $R_{MvK} = k\vartheta_{1a} p_{1b}$. This has the same mathematical form as Eley-Rideal kinetics. When the reaction product desorbs, a vacancy is left behind in the surface. This vacancy will be filled again by the first reactant (reaction 1a). In principle, in the mechanism as described by Mars and Van Krevelen in 1954 [26], the vacancy created by the reaction is filled by a reactant atom from the bulk, rather than the gas phase. In my view, however, it is purely a semantic discussion whether the supply of atoms filling the vacancies originate from the bulk or the gas phase, since this difference does not influence the relevant processes within the reaction mechanism. An example of the Mars-Van Krevelen reaction mechanism is CO-oxidation under high oxygen pressure on platinum – the surface forms a surface oxide with which the CO interacts [27]. In this particular case, roughening of the surface takes place; when an oxygen vacancy is created, the uncoordinated platinum atom becomes highly mobile, and starts diffusing

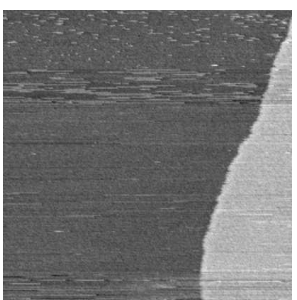

on the surface, until a reaction with an oxygen molecule from the gas phase fixes it to its position. Under certain conditions, this leads to spontaneous reaction oscillations [28].

1.1.4 The traditional surface science approach

Catalysts in real working conditions are very complex systems. Many factors determine the activity and selectivity of a catalyst. A large surface-to-volume ratio, and adding certain additives, increase its yield. Often high temperature and pressure conditions are necessary for maximum productivity. On the other hand, catalysts experience degradation. At high temperatures, dispersed catalytic nano-particles undergo sintering, and small pollutions within the reactants or byproducts of the reaction can poison the surface of a catalyst, by blocking the active sites. Many of the catalysts used nowadays have been developed by trial and error; however, the fundamental approach towards understanding heterogeneous catalysis became a major field in surface science. Traditionally, simplified model catalysts, such as single crystals polished in a certain orientation (section 1.2), are studied under ultrahigh vacuum (UHV) conditions. Numerous surface sensitive techniques have been developed for catalyst characterization at different levels, of which a few are mentioned here. Auger electron spectroscopy and X-ray photo spectroscopy can be used for chemical characterization. Scanning tunneling microscopy, atomic force microscopy, surface X-ray diffraction, scanning and transmission electron microscopy, and low energy electron diffraction can be used for characterization of the surface structure of the catalyst. Infrared spectroscopy and high-resolution electron energy loss spectroscopy provide information about the vibrational properties of the surface. For theoretical studies, density functional theory and Monte Carlo simulations are common methods. Most of these surface sensitive techniques actually require the use of UHV. In order for information carriers such as ions, electrons, and photons to interact with the surface of a crystal, rather then the bulk, their energy should be low. To maintain a long mean free path for these low-energy carriers, they should not interact with gaseous molecules between source, substrate, and detector, hence the necessity for UHV. Moreover, the UHV provided a clean and well controllable environment for performing experiments [5, 6]. This approach has two substantial shortcomings, since catalysts in industry mostly consist of alloyed nano-particles, dispersed on a highly porous support material exposed to high pressures of reactants. These shortcomings are defined as the “pressure gap” and the “materials gap”, which will be discussed more thoroughly in the next section. Despite these disadvantages, these techniques did contribute substantially to our fundamental understanding of catalysts,

giving insights into the functioning of catalysts at the atomic level, the influence of steps, kinks, dangling bonds, uncoordinated atoms and surface dynamics, reaction mechanisms, and catalyst degradation mechanisms.

1.1.5 Gaps

The Pressure Gap

As mentioned in the previous section, surface sensitive techniques often require ultrahigh vacuum conditions, whereas, in industrial catalysis, high pressures are common. Recent investigations at high gas pressures have yielded knowledge which could not be predicted by extrapolating the low-pressure results [27, 36, 47, 48]. This discrepancy between science and industry is called the pressure gap [49, 50]. To illustrate the effect of a gas on the surface free energy γ, we define in equation 1.1.5 the Gibbs model, which states that the interface between two bulk phases, with a uniform concentration, can be seen as a surface of zero thickness, the Gibbs dividing surface. This surface describes the real system by accounting for the excess entropy, energies, and material [24].

$$\gamma = f^s - \sum_i \mu_i \Gamma_i. \tag{1.1.5}$$

In this equation, f^s is the Helmholtz free energy for the Gibbs dividing surface per unit area, while the sum describes the contribution of gas i by its chemical potential μ_i. Γ_i is the adsorption of component i. The chemical potential of gas i is given by equation 1.1.6, from which can be seen that it depends on the gas partial pressure p_i and the temperature T. μ_i^0 and p_i^0 are its reference potential and pressure; k_b is the Boltzmann constant.

$$\mu_i = \left(\frac{\partial F}{\partial n_i}\right)_{T,V,n_j} = \mu_i^0 + k_b T \ln \frac{p_i}{p_i^0}. \tag{1.1.6}$$

Via equation 1.1.6, we can now estimate the difference between the contributions of the gas to the surface free energy, when working in UHV or at ambient pressure. In comparison with adsorption experiments performed in UHV, with typically $p \approx 10^{-9}$ bar, the pressure is 9 orders of magnitude higher at ambient pressure, so the extra contribution per gas molecule, will be $9 \cdot 2.35kT \approx 0.54$ eV at room temperature, which irrefutably is a significant contribution to the surface free energy. One could argue that the same effect, of the chemical potential on the surface free energy, can be achieved by decreasing the temperature, instead of increasing the pressure, meaning that in terms of thermodynamics, the situation with high (T,p) is equal to

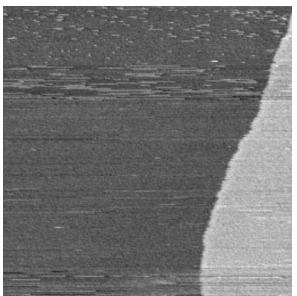

low (T,p) – so why push surface science techniques to the limit, by exposing them to extreme environments, if you can make life much simpler by cooling down your sample in ultrahigh vacuum? The answer to that question is catalytic activity. At a very low temperature, the surface of the catalyst will not be active at all, since the activation energies for separate reaction steps will be too high for them to occur at the surface in that situation. Another argument is the smearing of phase boundaries, between different surface terminations, under realistic conditions, as has been shown by kinetic Monte Carlo simulations [29]. At low (T,p), these boundaries will remain sharp. At present, much effort is being made to overcome both the materials and the pressure gaps, as will be described in more detail in chapter 2.

As an example of a pressure gap effect, a theoretical study, consisting of a constraint thermodynamics study, in combination with kinetic Monte Carlo simulations [29, 30] on CO oxidation on Pd(100), has shown that, under relevant reactant feed conditions, i.e. a stoichiometric supply of CO and O_2 at ambient pressures, the most stable phase is a surface oxide. However, this situation is close to a phase boundary, with a CO-covered metallic Pd(100) surface. Slight variations in temperature and pressure can easily shift the equilibrium across this phase boundary, initiating a phase transition. This means that coexistence of surface oxide patches and CO-covered metallic patches are plausible, even under steady state conditions. Oscillations in this situation are conceivable, so in order to understand the whole catalytic system, both phases, and the transition between these phases, have to be studied under ambient conditions.

The Materials Gap

A second drawback, the materials gap, was mentioned in section 1.1.4, next to the pressure gap. Industrial catalysts often consist of metal alloys dispersed as nano-particles on oxides. Additionally, the catalyst is usually enriched by promoters to increase its yield. The two main reasons to disperse catalysts as nano-particles are firstly, the maximization of the available active sites for the reaction, and secondly, the reduction of the amount of catalyst material needed, since many of the catalytically active transition metals are expensive. These complex cocktails of materials are too complicated to study with surface science techniques, which necessitates simple model systems, often in the form of bulk single crystals. The following differences between industry and science arise from this simplification step. Step, edge, and kink sites contribute significantly to the surface area of nano-particles. On single crys-

tals, the number of these types of sites is relatively small, which can cause a strong decrease in activity. Moreover, the boundary between support material and catalyst, and between various facets on catalyst nano-particles, influence the electronic structure, and therefore the activity towards certain reactions. When using a single crystal surface, these interactions are totally absent. Furthermore, the activity of a catalyst can be strongly size-dependent, as for instance is the case with gold – bulk gold is inert, whereas gold nano-particles exhibit high catalytic activity [31–33]. The materials gap comprises these differences between real catalysts used in industry and model catalysts used in research.

1.1.6 Suitable techniques for realistic conditions

In the present study, different surface analysis techniques have been adapted to operate under realistic conditions. Examples, which will be briefly discussed in this section, are infrared reflection adsorption spectroscopy (IRAS) [34], X-ray photoemission spectroscopy (XPS) [45, 46], transmission electron microscopy (TEM) [51], surface X-ray diffraction (SXRD), [52], scanning tunneling microscopy (STM) [50, 53, 54], and atomic force microscopy (AFM) [55]. Of course, theory should also be mentioned here, since methods including density functional theory and kinetic Monte Carlo simulations provide considerable insight into the operation of catalysts in realistic conditions, and create a basis on which new experiments can be planned and the experimental results obtained can be explained.

In situ IRAS, under reaction conditions, has been facilitated by the construction of a high-pressure micro-cell, with CaF_2 walls. These are transparent for infrared light, and have been integrated in an ultrahigh vacuum system [34, 35]. IRAS is a technique, which can distinguish between different molecules adsorbed on a surface, by the vibrational characteristics of the bonds in each molecule. For characterizing catalytic reactions, this technique can be valuable: concentrations of reactants and reaction products can be measured, from which turn-over frequencies and reactivity of a catalytic sample can be determined. The major drawbacks of IRAS are its insensitivity to the surface and its insensitivity to metal-adsorbate bonds, since the vibrational frequencies of metal-adsorbate bonds are often lower (< 600 cm^{-1}) than the operational frequency range of IRAS.

X-ray photoemission spectroscopy is a very powerful technique in catalysis, because of its surface sensitivity. The surface elemental composition can be determined by core-level peak intensities, while a shift in these intensities

provides information about the chemical bonds at the surface. Traditionally, this technique had been limited to ultrahigh vacuum conditions, because of scattering of the emitted photoelectrons in the gas phase. The development of a differentially pumped electrostatic lens system enables this technique to operate under relatively high pressures, up to 5 mbar [45, 46]. This number also illustrates one of its disadvantages: although a huge step, from UHV to the millibar range, has been made, the technique cannot (yet) operate under realistic conditions.

Nano-reactors, which fit into the tip of a standard TEM, are under development, to realize in situ TEM studies at ambient conditions, including heterogeneous catalysis. This particular field in TEM is called environmental TEM (ETEM). The nano-reactors are based on MEMS[1] technology, and their windows are (1) electron transparent, and (2) placed very close to each other, in order to minimize the loss of intensity of the electron beam within the nano-reactor. Using the nano-reactors, it is possible, for example, to study the properties of catalytic nano-crystals on oxide supports, under reaction conditions. At the moment of writing, carbon contamination of the reactors is a major issue: the windows of the nano-reactors can be blocked and presumably also the nano-particles can be covered with multiple layers of carbon.

SXRD is also very suitable for studying catalytic surfaces, under realistic conditions, since the interaction between X-rays and gases is very weak. The technique provides structural information about symmetrical surface geometries on a catalyst. This can be linked to reactivity if residual gas analysis is performed simultaneously. A dedicated instrument for this type of in situ study of catalyst surfaces has been developed, and is discussed in detail in [52]. With this technique, nano-particles on a flat support can be studied, as long as the surface is reflective for the X-rays.

Scanning tunnelling microscopy is a suitable technique for bridging the pressure gap, since it is operable under UHV and high pressure conditions, as well as for temperatures ranging from 4 K to >1000 K [56]. This type of microscope can provide real space, atomically resolved, images of the catalytic surface, opening the possibility of studying the surface structure under the influence of different gas environments, of indicating active sites, and studying the role of possible promoters. In addition, the STM has a weak and local interaction with the surface, and will therefore not influence the properties of

[1] Micro-Electro Mechanical Systems

the catalyst. The difficulties of this technique lie in the fact that everything has to be kept small. It also needs a stable environment, in which drift, due to temperature differences, and noise, due to mechanical and acoustical vibrations, have to be kept to a minimum. Additionally, only conducting surfaces can be investigated, which excludes oxide-supported nano-particles.

Atomic force microscopy falls into the same category as STM, but since its operational principle is based on the repulsive force between sample and a cantilever, insulating surfaces can also be studied. This opens the way to studying catalytic nano-particles supported by non-insulating materials. A high-pressure ReactorAFM is in development [55].

Although all the techniques described in this section already approach the realistic working conditions of a catalyst, they all have their limitations, either in sensitivity towards some aspects of the structure or reactivity of a catalyst, or in only partially bridging the materials and/or pressure gaps, depending on which sample and environmental specifications are demanded by the specific technique. Eventually we want to be able to study alloys, nano-particles on porous materials, and catalytically active materials in combination with promoters. Some of the surface sensitive techniques certainly have the potential to be developed in that direction.

1.2 Crystallography

To describe the structure of a crystal, which consists of regularly ordered atoms, a unit cell is defined, after choosing a set of coordinate axes and an origin. This unit cell is spanned by three lattice vectors **a**, **b**, and **c**, with lengths u, v, and w, and mutual angles α, β, and γ. The concept of a unit cell is illustrated in figure 1.3. Figure 1.3 A shows a conventional unit cell for a face-centered cubic crystal[2], defined by $\mathbf{r} = u\mathbf{a} + v\mathbf{b} + w\mathbf{c}$. One of the angles between the vectors is indicated by ϕ; in this case, $\alpha = \beta = \gamma = 90°$. The properties of a unit cell are that it be translationally invariant, and that it should contain all the information necessary to build up the bulk crystal lattice, as shown in figure 1.3 B and C. By translating the unit cell a unit of distance along each of the lattice vectors, it will always place itself in a position equivalent to the position at the origin. The smallest possible unit cell, which still holds all the crystal's information, is called the primitive unit

[2]The different types of crystal structures will be discussed below; I have chosen the face-centered cubic crystal lattice as an example in this section because all the crystals used in this research exhibit the face-centered cubic structure.

cell. This is different from the conventional unit cell. The geometry of the primitive unit cell can be complicated, which makes the use of the conventional unit cell preferable.

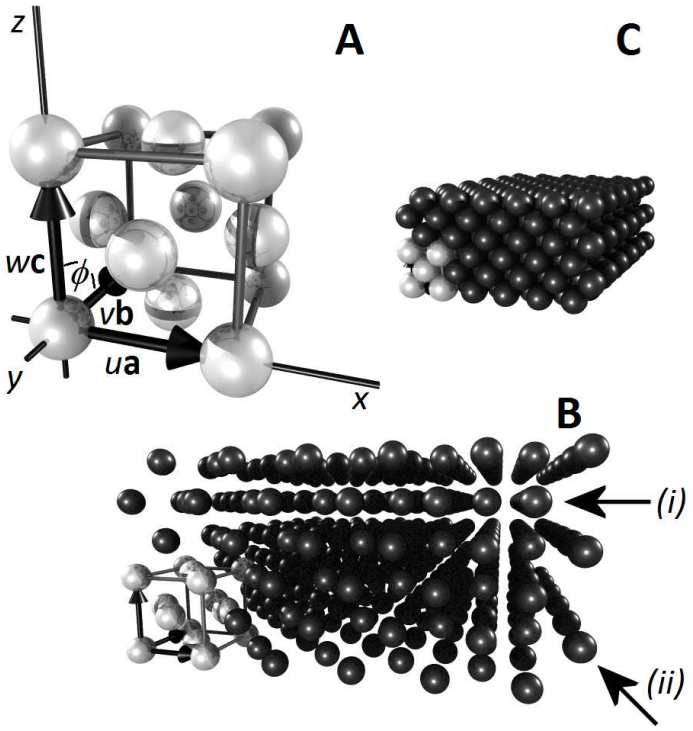

Figure 1.3: Example of a unit cell: the face-centered cubic crystal. (A) Unit cell with lattice vectors $u\mathbf{a}$, $v\mathbf{b}$ and $w\mathbf{c}$; one angle ϕ is indicated. (B, C) The unit cell projected in the bulk crystal lattice.

Looking at figure 1.3 B, one can easily see that it is possible to define sets of equally spaced parallel planes, in different directions through the crystal, two of which are indicated by arrows (i) and (ii). These planes have identical atomic densities. A crystal can be cut and polished along one of these planes, which creates a surface with a specific atomic arrangement and geometry[3]. Different surfaces have different properties; in catalysis, for example, a different surface geometry will provide different adsorption sites and energies, which can influence the reaction rate or selectivity towards a chemical reaction strongly. To name and group all possible plane orientations, Miller

[3]As an example: the various facets on a polished gem, like a diamond, can be grouped according to such planes

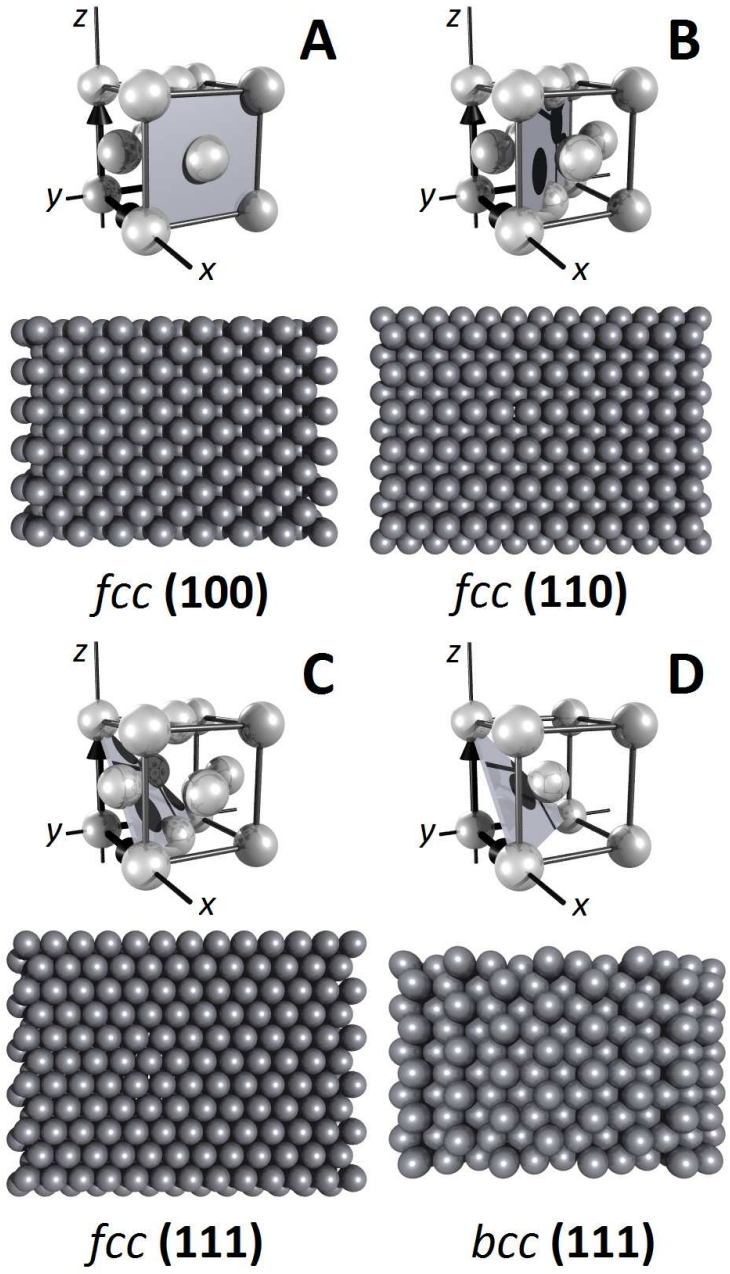

Figure 1.4: (A) The face-centered cubic unit cell, in which the (100) Miller index plane is shown (top), with corresponding surface termination (bottom). (B) The (110) Miller index plane and surface. (C) The (111) Miller index plane and surface. (D) The (111) Miller index plane and surface for the body-centered cubic lattice.

indices were introduced, which are defined as intercepts of the (Miller) plane on the crystal axes closest to the origin, and therefor consist of three digits. As an example, figure 1.4 shows three different geometries for such a plane for the face-centered cubic lattice, in combination with the corresponding surface termination. The top part of figure 1.4 A shows the (100) plane for the crystal: the plane cuts through the x-axis at $x = 1$, and runs parallel along the y and z-axis, hence (100). The bottom part shows the geometry of the surface when a crystal is cleaved along this direction. Similarly, figure 1.4 B shows the (110) plane, and figure 1.4 C the (111) plane. As can be seen, the surface termination of a crystal varies strongly with the orientation of the Miller plane. Polishing a crystal along higher Miller index planes, e.g. (553), creates stepped and vicinal surfaces [37].

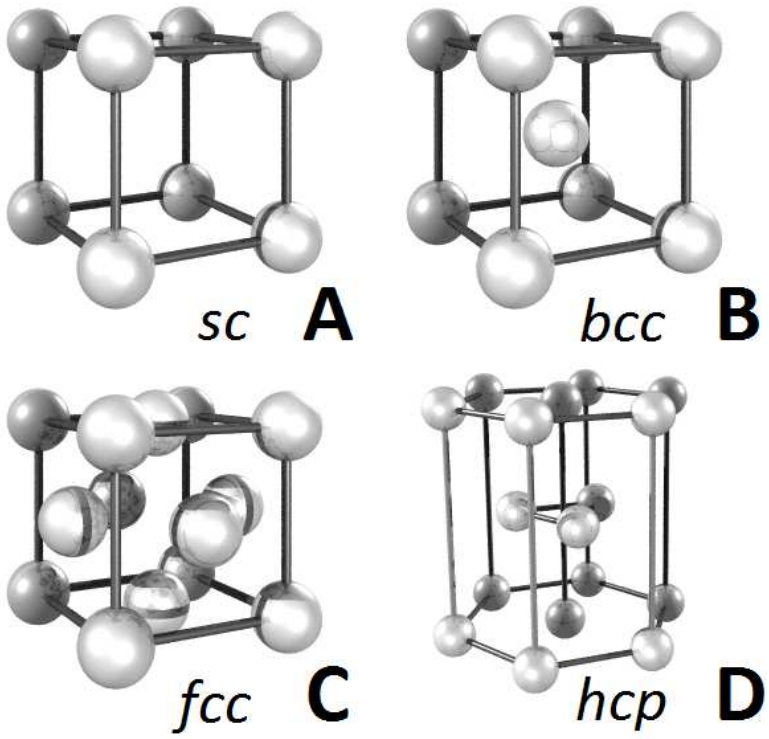

Figure 1.5: (A) The simple cubic lattice, (B) the body-centered cubic lattice, (C) the face-centered cubic lattice, and (D) the hexagonal close-packed lattice

In figure 1.3 and 1.4, the face-centered cubic crystal structure is used as an example. More structures exist, of which the conventional unit cells of the most common ones are illustrated in figure 1.5 – nearly all metals have

one of these structures. The first structure shown is the simple cubic lattice (sc), in which the unit cell contains exactly one atom. Polonium is reported to have this structure. The unit cell of the body-centered cubic (bcc) structure, containing two atoms, is shown in figure 1.5 B. Examples of metals having this crystal structure are iron, tungsten, and sodium. And finally, the face-centered cubic (fcc) structure, is depicted in figure 1.5 C. This unit cell contains four atoms, and exhibits the closest possible packing for cubic lattices. Nickel, silver, and gold are examples of metals with this structure. In addition to cubic stacking, there is also the possibility of stacking the atoms hexagonally, which is shown in figure 1.5 D. This is called the hexagonal close-packed (hcp) structure. Examples are zinc, titanium, and cobalt [38]. The crystal structure also influences the surface termination, which is illustrated in figures 1.4 C and D; both show a (111) Miller index plane. In figure 1.4 C, the (111) plane is for an fcc lattice, and in figure 1.4 D, the (111) plane for a bcc lattice.

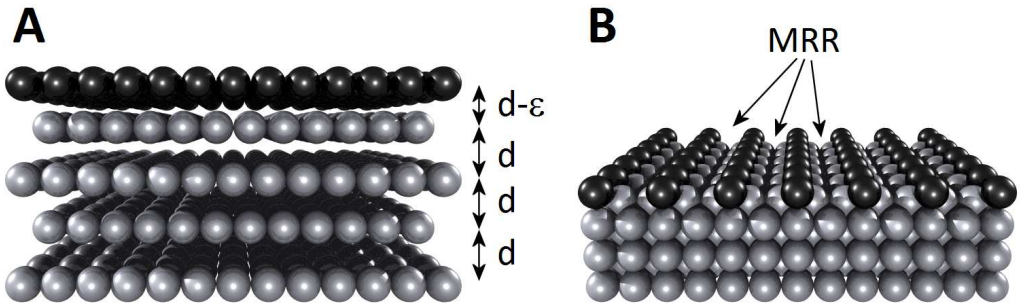

Figure 1.6: Examples of surface relaxation and reconstruction, using the fcc (110) surface. (A) Relaxation: the distance between the surface layer and the layer below is contracted by ϵ with respect to the bulk distance d. (B) Reconstruction: the surface layer termination is different from the bulk crystal. In the fcc (110) lattice, every second row of atoms on the surface is missing, creating the so-called missing-row reconstruction (MRR).

In the bulk of a crystal, the forces exerted on the equilibrium positions of the individual atoms by their surroundings are equal. At the surface, however, these forces change, which can lead to relaxation or reconstruction of the atoms at the surface. When the surface undergoes relaxation, the entire surface shifts with respect to the bulk, without changing the other interatomic distances at the surface. Since there is an attractive force towards the bulk, relaxation often induces the top layer to decrease its distance to the bulk, resulting in a different inter-layer distance than that within the

bulk itself (fig. 1.6 A). This type of relaxation is common for most metals. Reconstruction, on the other hand, also includes rearrangement of atoms on the surface layer, resulting in a different surface geometry, with respect to the bulk [39]. This happens, for instance, at the lower Miller index planes of the late 5d metals gold, iridium, and platinum, due to a significantly larger tensile surface stress in these metals than in the related 3d and 4d metals. This causes the 5d metals to reconstruct, rather than just to relax. It is believed that, next to the electron density within the 5d metals, the stronger bonding of low coordination atoms is caused by competition between the s and d electrons, arising from relativistic effects [40–42]. The surface reconstructions occurring are, for instance, hexagonal close packing on the (111) surface, a missing-row reconstruction on the (110) surface (fig. 1.6 B), and a quasi-hexagonal restructuring of the (100) surface. Due to the difference in symmetry between the unreconstructed and reconstructed lattices, the periodicity of these surface structures is usually quite large; typical commensurate unit cells are (1x5) or (5x20) [43].

When two similar grids are overlayed at an angle, or when two slightly different grids are overlayed, an interference pattern is created, called a Moiré pattern. The effect is illustrated in figure 1.7. When the two grids are rotated with respect to each other, the interference pattern can clearly be seen as a recurring structure, with a larger periodicity than the separate grids (B), whereas it cannot be observed when they overlay at the same angle (A) [44].

This phenomenon also occurs on the atomic scale, for instance when the surface of a crystal has a different orientation or structure, with respect to the bulk, as in the case for the surface reconstructions just discussed[4], or when two different materials are superimposed on each other, which have the same lattice structure, but different interatomic spacing[5]. The patterning effect can be observed by a scanning tunneling microscope. When the surface is only liable to relaxation, which would be similar to the situation in figure 1.7 A, no pattern formation will occur.

[4]This is the case for Pt(100), which we have used for NO reduction in chapter 3

[5]This happens when MoS_2 is evaporated onto Au(111), which is discussed in chapter 5

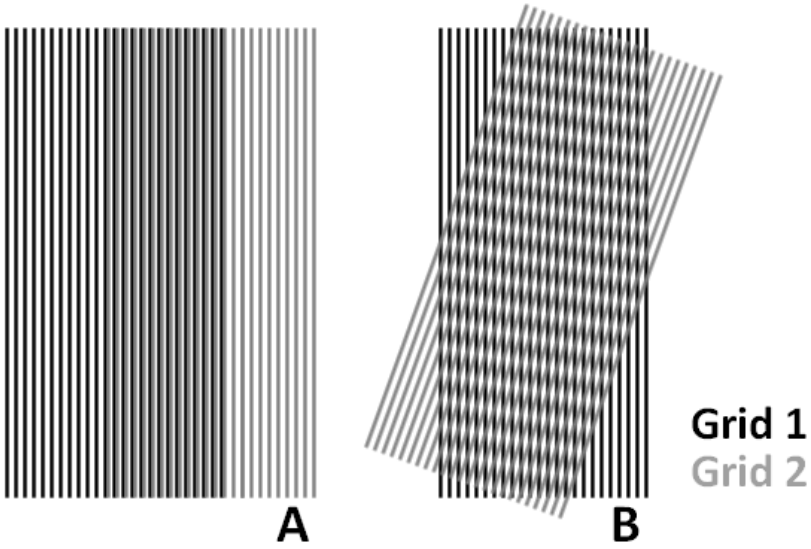

Figure 1.7: (A) Two grids overlayed at the same angle exhibit no interference pattern. (B) When rotated with respect to each other, an interference pattern can be observed, superimposed on the two grids

1.3 Scanning Tunneling Microscopy

1.3.1 STM in general

The concept of scanning tunneling microscopy was invented in 1981 by Binnig and Rohrer [10], for which they were awarded the Nobel Prize in physics in 1986. The technique enabled both high resolution imaging and manipulation of individual atoms on conducting surfaces, routinely. The basic elements of an STM are shown in figure 1.8.

A sharp tip, usually made out of chemically etched tungsten or mechanically sheared platinum iridium, and a conducting sample are brought together, to within a few atomic distances ($\sim$5 Å) of each other, such that the electron wave functions of sample and tip overlap. If, in this situation, a bias voltage V_b is applied between the tip and the sample, quantum mechanics predicts that there is a nonzero probability for electrons to tunnel through the vacuum barrier. This yields an electrical current between tip and sample, the tunneling current I_t (eqn. 1.3.1). This current depends exponentially on the distance between tip and sample d, which leads to the extremely high resolution of the STM: when the distance between tip and sample is increased by 1 Å, the tunneling current decreases one order of magnitude [11, 12].

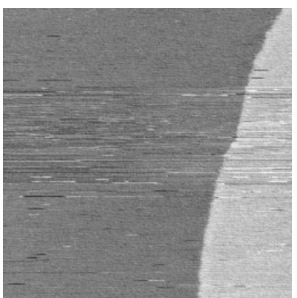

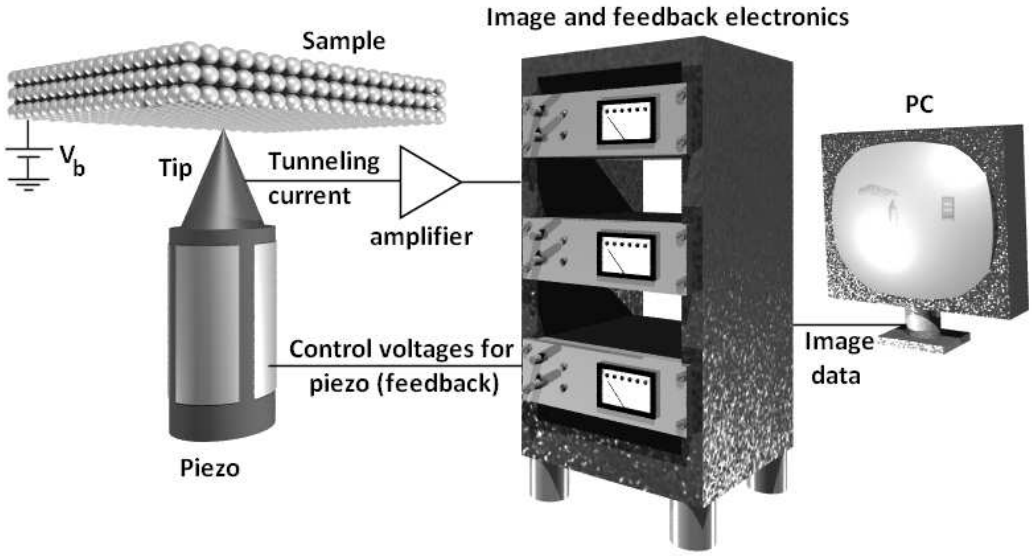

Figure 1.8: The concept of a scanning tunneling microscope

$$I_t \propto V_b \exp\left(-2\sqrt{\frac{2m\Phi}{\hbar^2}}\, d\right). \tag{1.3.1}$$

The usual modus operandi of an STM is raster-scanning the tip across the surface, while the tunneling current is monitored at a fixed bias voltage. The motion of the tip in x, y, and z is controlled by a piezo[6] tube, containing separate piezoelectric elements for each direction. By applying a sawtooth voltage to the x piezo and a voltage ramp on the y piezo, the raster-scanning motion can be generated. During scanning, a feedback circuit can regulate the STM in two modes: the constant current mode and the constant height mode. In the constant current mode, the feedback circuit regulates the voltage on the z-piezo to adjust the distance between tip and sample, maintaining a constant tunneling current during scanning motion. The feedback signal, which is directly related to the z position of the tip and stored as a function of the x and y position, translates into a topographical image on the computer screen. In constant height mode, the z position of the piezo is kept constant. In this way the tunneling current can be directly correlated to surface structure, which as a function of x and y translates again into a topographical image. The choice between the two feedback modes is determined by the target of the research: the constant current mode provides higher image res-

[6] A piezoelectric material is a material that contracts or expands under the influence of an applied voltage.

olution, whereas the constant height mode enables faster data acquisition. To gain high resolution with an STM, it is important to make the system as insensitive to vibrations as possible. This can be achieved by, on the one hand, constructing the STM to be as rigid as possible, and, on the other hand, by using active and passive damping systems, such as, for instance, an Eddy-current damping mechanism for damping external mechanical and acoustic vibrations [11, 13].

STM is a very powerful technique, as it can be operated in very diverse environments: under ultrahigh vacuum and high pressure environments, low (mK range) and high (10^3 K range) temperature environments, and in various liquid environments. The fields in which STM is being used include thin film growth [14–16], self assembled monolayers [17–19], electro chemistry [20–22], and catalysis [12, 23, 27].

1.3.2 ReactorSTM^{TM}

ReactorSTM^{TM}: The concept

In figure 1.9, a conceptual drawing of the ReactorSTM^{TM} is presented. Given is a reactor volume V, with inert walls, to which two thin gas lines are connected: (1) gas inlet and (2) gas outlet. The inlet is connected to a gas system, which can mix gases A and B in a chosen ratio to flow this into the reactor volume. The outlet leads to a quadrupole mass spectrometer, for residual gas analysis of the exhaust. Only the STM tip is exposed to the reactor volume: a ring R_1 separates the rest of the approach motor from the reactor volume. In this way, the reactor volume is kept small, to enhance refresh rate and response time, and so that the different elements of the approach motor are not exposed to high pressures of violent gases. A ring R_2, on which the sample is pressed, seals the reactor volume from the UHV environment surrounding it. Along these lines, the sample surface, which can be heated from the back, is exposed to the high gas pressures, and can be approached by the tip.

ReactorSTM^{TM}: The setups

The work in this thesis has been performed in two different ReactorSTM's, which will be distinguished by adding "Mark I" or "Mark II" to the name. ReactorSTM Mark I was developed approximately a decennium ago and is briefly described in this section. An in depth description of this microscope

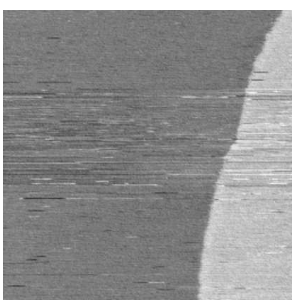

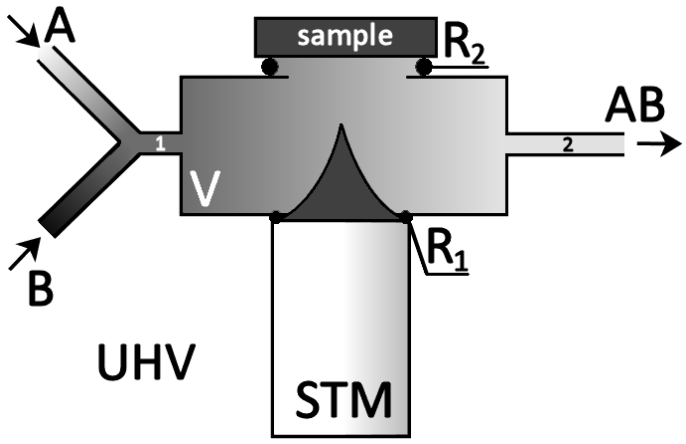

Figure 1.9: Conceptual drawing of the STM. (V) Reactor volume, (A), (B), (AB) gases, (R_i) flexible rings.

can be found in [53]. Chapter 2 is fully dedicated to the newly designed ReactorSTM Mark II; its development was part of the work described in this thesis.

The experiments described in chapter 3 and part of the experiments described in chapter 5 of this thesis have been carried out in the ReactorSTM Mark I. A 3D impression of the vacuum system in which it is housed, in combination with a technical drawing of the STM itself, is shown in figure 1.10.

With the ReactorSTM^{TM}, model catalyst surfaces can be imaged at elevated temperatures and atmospheric pressures [27, 53]. The instrument features an STM integrated with a small (0.5 ml) flow reactor cell (1), through which a variety of clean gas mixtures can be allowed to flow, at pressures up to 2 bar. The construction of the STM-reactor combination is such that only the STM-tip and its holder (2) are inside the reactor, while the other STM components, such as the piezo element (3), are outside. The entire ReactorSTM^{TM} system is housed in an ultrahigh vacuum (UHV) chamber (4). This enables us to prepare and characterize the sample surface by state-of-the-art surface-science techniques (see below). After preparation, the sample (5) is pressed firmly against the flow reactor. In that geometry, it forms one of the walls of the reactor. A Kalrez ring, between the sample and the rest of the reactor serves as a nearly UHV-tight seal between the reactor volume and the vacuum chamber (6). In order to measure the gas composition inside the reactor, and thus derive the catalytic conversion rates, we take

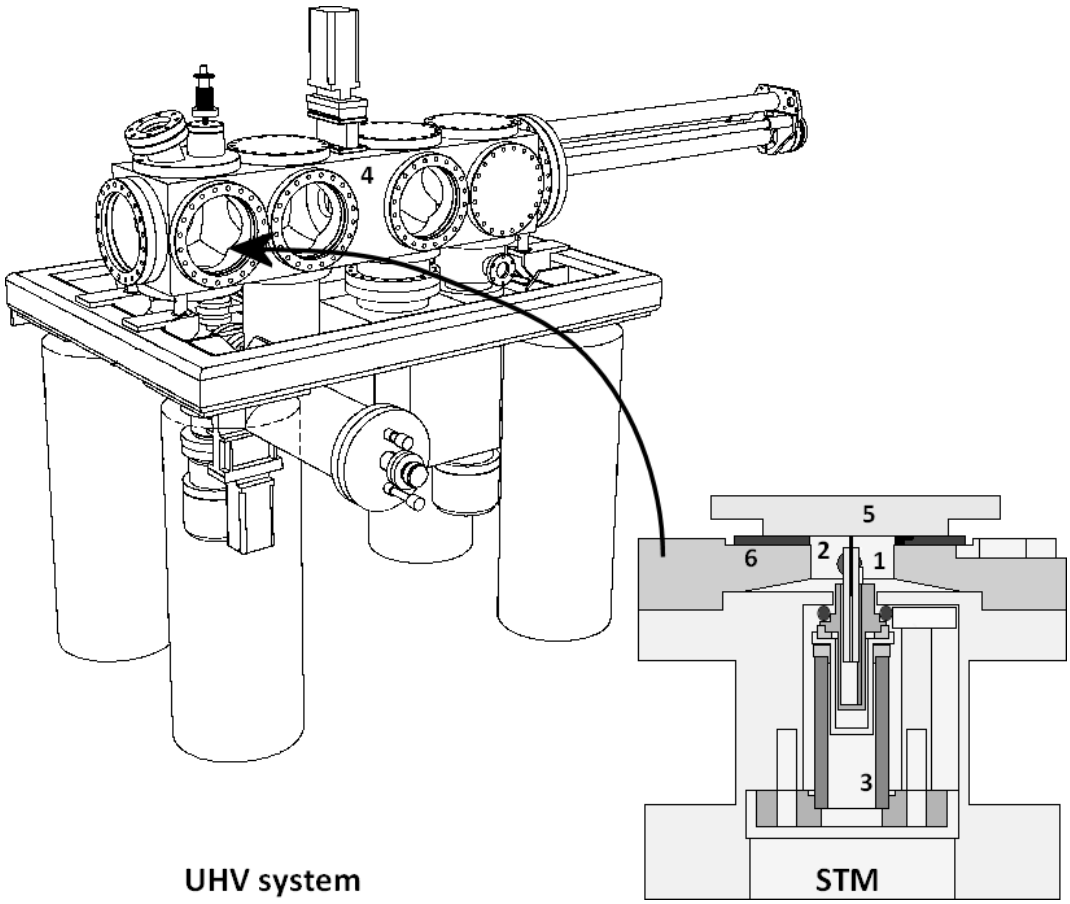

Figure 1.10: The UHV system and cross-section of the ReactorSTM Mark I.

advantage of the small gas leak over the Kalrez seal into the UHV chamber, which is equipped with a quadrupole mass spectrometer (QMS). The sample holder contains a filament, located directly behind the model catalyst. With this, the sample can be heated, both for preparation purposes and during actual experiments, when the sample is placed on the reactor.

The flow, pressure, and composition of the gas mixtures are controlled by a gas system combining a series of mass flow controllers before the reactor, one for each high-purity gas, and a back-pressure controller behind the reactor. This configuration allows us to vary the composition without changing total pressure. In our experiments, the total pressure was fixed at 1.25 bar and the flow rate was set to 8 ml_n per minute, corresponding to a refresh time of the reactor volume of 4 sec.

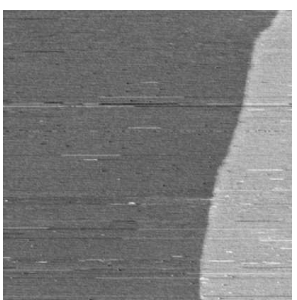

Chapter 2

ReactorSTM^{TM} Mark II: Design and performance

2.1 Introduction

As described in chapter 1, when research into the physical mechanisms underlying catalytically activated reactions at the surface of a catalyst was initiated, these were performed under ultrahigh vacuum (UHV) conditions. The then-existing techniques did not allow the introduction of a realistic environment to which a catalyst would normally be exposed [5, 6]. Recent investigations, at high gas pressures, have yielded knowledge which could not be predicted by extrapolating the low-pressure results [27, 36, 47, 48]. Therefore, it is important to adapt surface science techniques to operation under realistic reaction conditions.

This chapter covers the specifications, design, and performance of the newly built ReactorSTM^{TM} Mark II. It consists of a 0.5 ml flow reactor, housed in a dedicated ultrahigh vacuum (UHV) system. The reactor can be operated up to a total pressure of 5 bar (reactants plus products) and up to a sample temperature of 600 K. The UHV system enables us to combine the high-pressure experiments with traditional, high-quality sample preparation and analysis, for example with ion sputtering, metal deposition, LEED, AES, and XPS. In situ study of the structure and reactivity of a catalytic surface is facilitated by simultaneous STM and mass spectrometry. In this chapter are presented: (1) the requirements and technical layout of the STM, (2) the design and layout of the UHV system and a dedicated experimental gas handling system, and (3) the imaging performance of the instrument. Atomic resolution images of HOPG, showing increased imaging speed, and Au(111)

are shown, in combination with atomic row resolution images of Pt(110), under high-pressure and high-temperature conditions.

The development of this high-pressure, high-temperature STM, which has been called the ReactorSTM^{TM} Mark II, occurred within the framework of the NIMIC (Nano-Imaging under Industrial Conditions) consortium, consisting of several universities and research institutions, as well as industries [57]. The consortium and the hands on experience with the previous prototype [53] created a basis for developing a high-quality, robust microscope.

2.2 Specifications

For high-quality sample preparation and analysis techniques, such as ion sputtering, metal deposition, vacuum annealing, low energy electron diffraction (LEED), Auger electron spectroscopy (AES), and X-ray photo spectroscopy (XPS), we needed a standard ultrahigh vacuum (UHV) system. We did not want to expose the prepared samples to contaminating environments, during transfer to the high-pressure environment; therefore, we needed to combine a high-pressure cell inside the vacuum system, which could be sealed off. Since some of the equipment should be stored under very clean vacuum, we needed to separate the UHV system into more than one chamber.

To approach industrial conditions during our STM measurements, we needed to operate the STM in a controllable, high-pressure (up to 5 bar) gas flow, which could refresh the reactor volume within a few seconds. This translated into a flow of typically 10 ml_n/min. To activate the catalytic surface, we needed to heat it, aiming at a maximum temperature of 600 K at the sample. Furthermore, we wanted to atomically resolve typical catalytic surfaces, such as, for example, platinum. This implied that a stable STM, with a short mechanical loop, an active damping mechanism, a low noise level, and good temperature stability, to suppress thermal drift, was needed. The noise level should not be larger than a fraction of the atomic corrugation, i.e. in the images, it should be smaller than 0.1 Å variations, both in height and in the plane of the atoms. To image fast processes at the surface, under reaction circumstances, fast imaging was also needed. Our first aim was to scan one image per second. In order to correlate surface structure with reaction rate, it was necessary to operate the STM simultaneously with a quadrupole mass spectrometer (QMS), which should have a response time in the order of seconds. This involves leading part of the exhaust gas line of

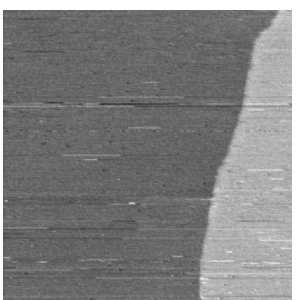

the reactor volume to the QMS without creating a large dead volume, and without influencing the control over pressure and flow.

To allow gases to flow through the reactor volume in a certain desired ratio of flow and pressure, we needed a dedicated gas handling system. This system should be able to mix four different types of gases in any combination, in ratios ranging from 1:1 to 1:100. Flow (0 to 10 ml_n/min) and pressure (0.5 to 5 bar) should be mutually and independently controllable. For fast and reliable operation, the volume of the system should be minimal, and dead volume non-existent. The system had to be able to deliver a sharp pulse of gas, of the same volume as the reactor volume, to the surface quickly, while influencing flow and pressure minimally. Furthermore, the system had to be bakeable up to 70℃, to acquire high cleanliness, and it needed to be fully computer controlled and interfaced.

These ambitions have been itemized in the following list of requirements:

- Atomic resolution on transition metal surfaces at high pressure and temperature: z-resolution of 0.1 Å
- Imaging speed: 1 image per second
- Pressure range in the reactor: 0.5 to 5 bar
- Temperature stability: drift in $z < 1$ μm/h (piezo range); drift in x, y < 50 nm/min
- Flow range in the reactor: 0 to 10 ml_n/min
- Gas ratio range: 1:1 to 1:100
- Temperature range of the catalyst: room temperature to 600 K
- Response time of changing gases in the gas handling system: < 5 seconds
- Response time of the mass spectrometer: < 5 seconds

These system specifications were just at the edge of industrial conditions, i.e. within the pressure and temperature scope of our requirements, there are only a few catalytic systems which we can study in the environment in which they would also operate in real life. In the end, it was our goal to increase these numbers, such that we could go to real industrial conditions

for a wide range of catalysts. Our efforts to date, however, have not been in vain. One might argue that we have "only" made the step from vacuum to 1 bar, whereas in industry, the pressures are often hundreds of bars. This means that, in terms of pressure, we only improved by 1%. But, the relevant number to look at is the chemical potential, discussed in section 1.1.5, which depends on the logarithm of pressure. So from the typical UHV experiments at 10^{-9} bar to 10^{2} bar in industry, we covered 9 of the 11 orders of magnitude, meaning we improved by 80 %. This number means that, in 80% of our studies, what we observe is 100% correct (and 100% wrong in 20 % of the cases), since the processes we observe are first order phase transitions. This is a significant improvement.

Combining these requirements, an ultrahigh vacuum system, with different chambers for preparation, analysis, and STM purposes was needed. The STM had to include a sealing mechanism, to open and close the reactor volume, to enable sample transfer in UHV. This sealing mechanism had to withstand high pressures and temperatures. To minimize mechanical vibrations from the surroundings coupling into the STM, in addition to introducing active damping, we needed to avoid using mechanical equipment during STM measurements. This meant not using turbomolecular pumps, and separating the QMS from the UHV system, since it has a cooling fan. We also have had to use thin capillaries to feed gases into the reactor, to prevent coupling of the damping mechanism, from which the STM is suspended, to the vacuum system, and to ensure a fast response time of the gas handling system.

With the ReactorSTM^{TM}, we wanted to study model catalysts under reaction conditions, including oxidation/reduction catalysts [27, 36, 58] and synthesis reactions in the petrochemical industry, such as Fischer-Tropsch synthesis [59] and hydrodesulphurization [60].

2.3 Design

This section shows the general architecture of the UHV system, and a detailed description of the ReactorSTM^{TM} Mark II and gas handling system.

2.3.1 UHV system

Figure 2.1 shows the design of the UHV system. The system consists of three chambers [61], separated by valves [62]: the analysis chamber (1), the

preparation chamber (2) and the SPM chamber (3). Every chamber can house a sample holder in different translational and rotational orientations, for accessing the various pieces of mounted equipment. The sample holders can be moved from one chamber to another by means of a transfer rod [61] (4). An ion pump, in combination with a Ti sublimation pump [63] (5), is connected to all chambers to maintain UHV. The preparation chamber is connected also to a turbo molecular pump [64]: firstly, to pump down the system during the starting up operation, and secondly, to pump away gases used to backfill the chamber during sample preparation. To inhibit mechanical vibrations from the turbo pump coupling into the STM, the UHV system should be pumped solely by the ion pumps during STM operation. To reach UHV, the system can be baked to 150℃, by installing a bake-out tent [65] and heating the system by two heating fans.

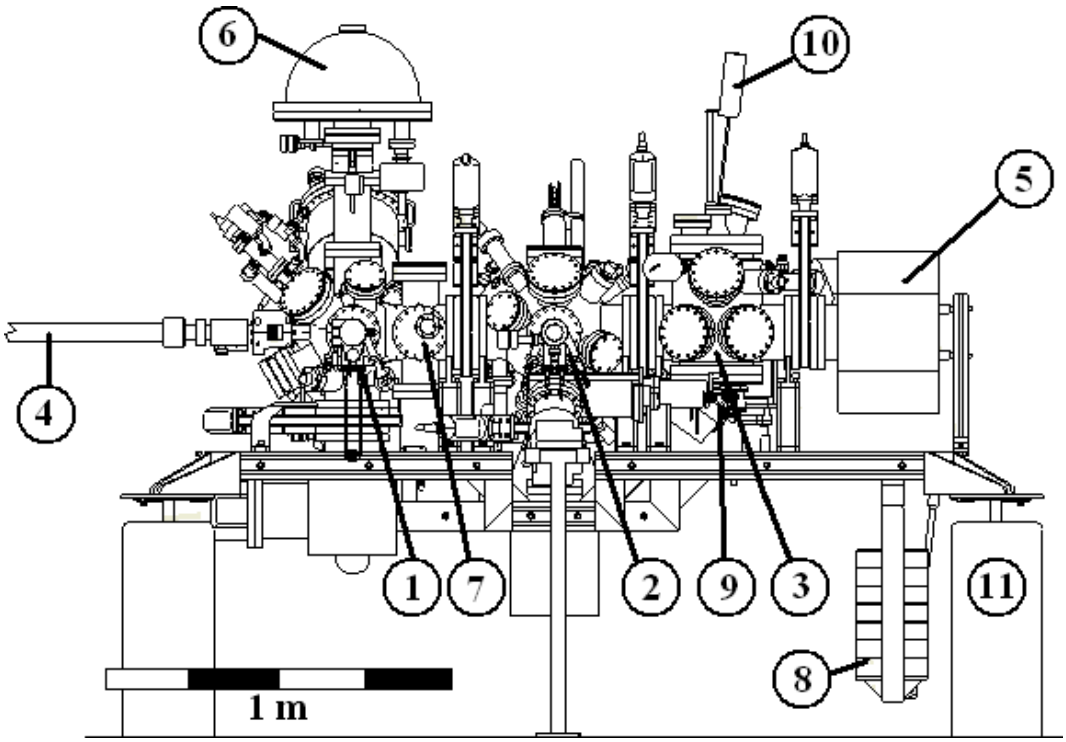

Figure 2.1: The UHV system. (1) Analysis chamber, (2) preparation chamber, (3) SPM chamber, (4) main transfer rod, (5) ion pump in combination with a Ti sublimation pump, (6) XPS, (7) sample library, (8) counterweight, (9) STM, (10) wobble stick, and (11) air legs.

The analysis chamber was designed to house an X-ray Photo Spectroscopy

(XPS, 6) [66] apparatus and a sample library (7). The XPS can be used to study the chemical composition on the sample surface, which can be combined with the STM and mass spectrometry data during analysis. The sample library can house two additional sample holders, opening the possibility for quickly changing samples. A counterweight (8), mounted onto the SPM chamber, counteracts the weight of the XPS, to balance the UHV system.

The preparation chamber houses a manipulator, which can translate and rotate the sample surface, to face it toward the various instruments mounted onto the chamber. The equipment includes a sputtering gun [67], for ion bombardment of the surface, an E-beam evaporator [68], to enable creation of nano-particle catalysts on a support, and LEED/AES [69], to investigate the cleanliness of the surface. The LEED/Auger can be separated from the preparation chamber by a valve, to prevent exposure to background gases used during sample preparation. A small gas system is able to backfill the preparation chamber with argon, oxygen, or hydrogen.

The SPM chamber contains the high-pressure STM (9). On the top flange, a seal library has been installed, along with a wobble stick (10), to allow the possibility of exchanging the reactor seals between experiments, as described in the next section. To minimize external mechanical vibrations from coupling into the UHV system during STM operation, it was suspended on air legs (11) [70]. In the near future, a reactor AFM will also be installed. For this, a copy of the existing UHV system has been made [55].

2.3.2 STM

In figure 2.2, part A shows a cross-section of the sample holder (1) and the STM (2) enclosing the reactor volume (3), a small volume of 500 μl. This volume is sealed from the UHV environment by two elastic rings. At the top, it is sealed by a special designed Kalrez ring (4), metal bonded to a stainless steel holder [71], which is clamped between the catalyst sample (5) and the STM body (6). The STM body is made out of Zerodur [72], a glass with a low thermal expansion coefficient, to ensure low drift properties during temperature changes. Furthermore, we choose, glass since part of the STM body is included in the wall of the reactor volume; glass is inert to the gases to be used during high-pressure experiments. At the bottom, the reactor volume is sealed by a Viton O-ring (7), which is clamped between the STM body and the top part of the approach and scan actuator (8). In this way, the piezo motor is not exposed to the high-pressure environment. The hat-shaped sample is held in position in the sample holder by a tan-

talum spring. A filament (9) mounted behind the sample enables sample heating. A sapphire shield (10) thermally isolates the filament from the rest of the sample holder. A type K thermocouple is laser spot-welded to the sample, for accurate temperature reading. Furthermore, the sample holder provides the electrical connections (11) to power the filament, read out the thermocouple voltage, and to provide a bias voltage to the sample, which is electrically isolated from its surroundings. Just as for the STM body, the sample holder body is constructed of zerodur, for the same reasons. Its support is of stainless steal, to provide mechanical strength. Three adjustment screws (13) provide a short mechanical loop between the sample and the tip, improving the stability and vibration insensitivity of the STM. The length of the adjustment screws is set to a value such that the compression of the Kalrez ring, when closing the reactor, is 20 % of its original thickness, specified to provide a leak tight seal. Two thin gas lines (14; just one of them is indicated) are connected to drilled channels in the STM body to feed the reactor volume with gases. In the bottom part of figure 2.2, a series of photos of the different reactor parts, as indicated in the cross section in part A, are shown.

Figure 2.3 shows the approach and scan actuator in more detail, rotated 90 degrees around its y-axis, with respect to figure 2.2. The tip (1) is clamped in a gold plated steel tip holder (2), which is pulled against two gold plated steel tracks (3) by a SmCo magnet [73] (4), glued to a support (5). The magnetizable steel parts are gold coated to ensure chemical inertness. The magnetic force, determined by the distance between the tracks and the magnet, is tuned in such a way that the piezo (6), an EBL2 [74], can overcome this force to move the tip holder up or down along the tracks. The tip is connected electrically to the tip holder and the tracks, which are clamped in an aluminium holder (7). In addition to carrying the tunnelling current, this aluminium holder is part of the wall of the reactor; aluminium is also chemically inert for the reactions we want to study. Electrical shielding is provided by an additional hat-shaped aluminium piece (8). Both aluminium pieces are electrically shielded from each other and the piezo tube by two insulating Macor rings (9, 10). The piezo is glued to a low-expansion Invar base (11), to minimize thermal drift during temperature changes.

The STM assembly in figure 2.2 is mounted onto the STM insert, as depicted in figure 2.4. The backbone (1), which holds the various components of the STM, is directly mounted onto a CF200 flange (2), which can be mounted into the SPM chamber on the UHV system from the bottom. The STM portal (3), containing the STM/ Kalrez seal/ sample holder combina-

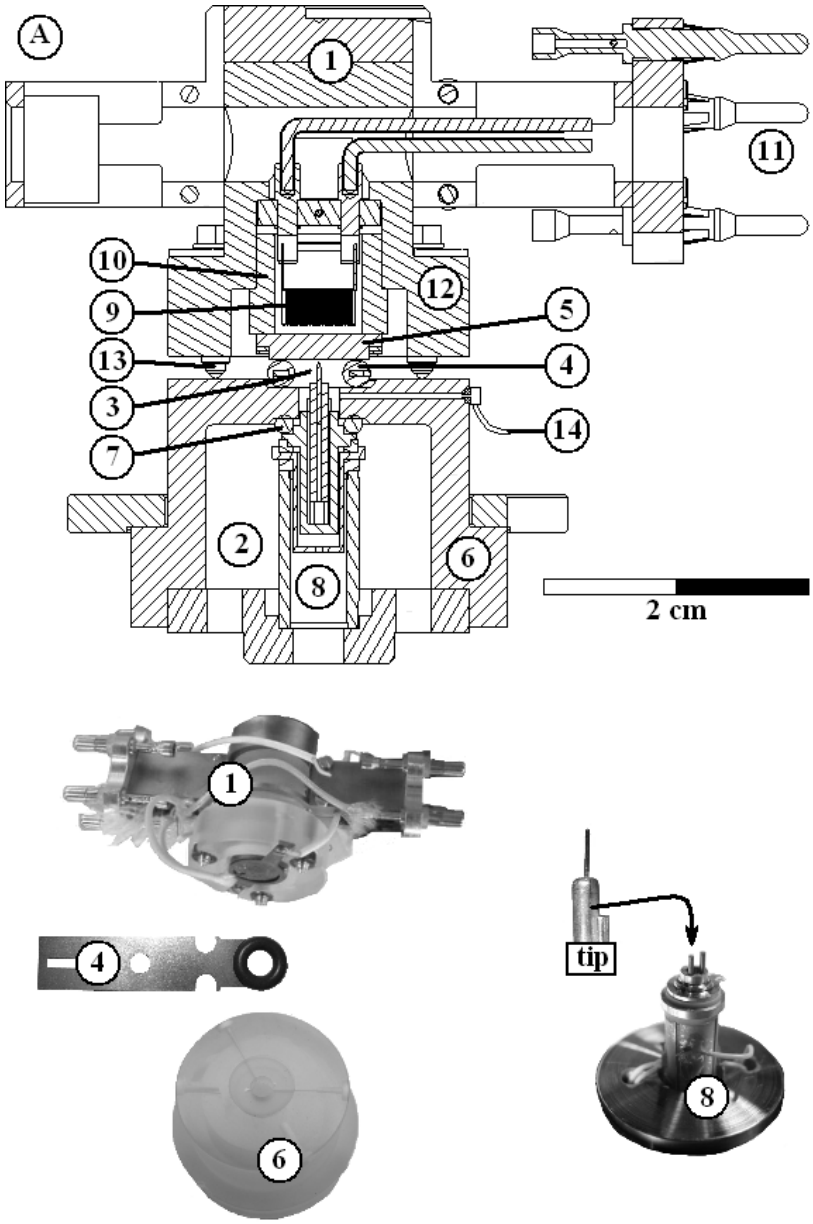

Figure 2.2: Cross section of the ReactorSTM^{TM}. (1) Sample holder, (2) STM, (3) reactor volume, (4) Kalrez seal, (5) sample, (6) STM body, (7) Viton O-ring, (8) approach and scan actuator, described in detail in figure 3, (9) filament, (10) sapphire heat shield, (11) electrical connections, (12) sample holder body, and (13) adjustment screws. Of parts (1), (4), (6), and (8) photos are shown below the drawing.

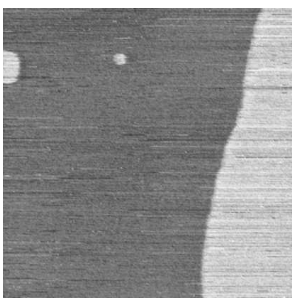

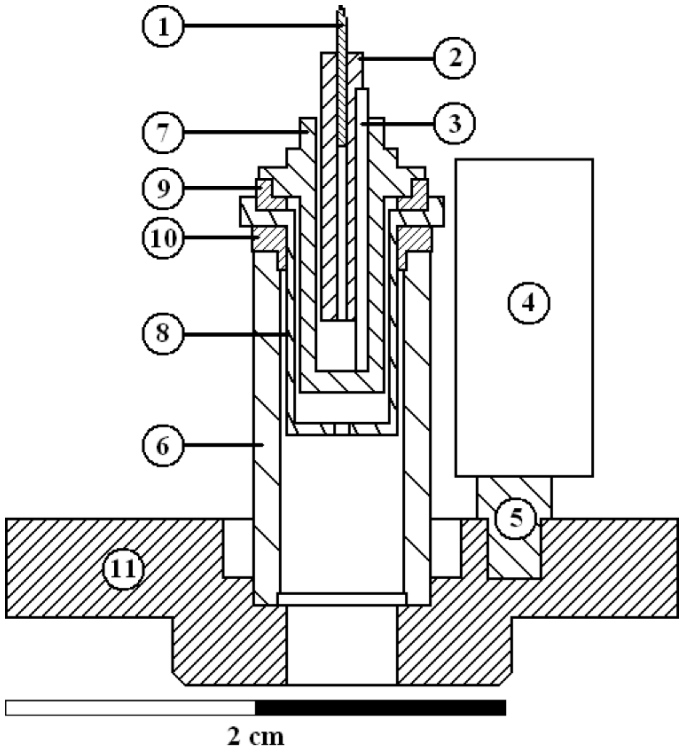

Figure 2.3: Cross section of the approach and scan actuator (photo (8) in figure 2.2). (1) Tip (for a photo, see figure 2.2), (2) tip holder, (3) tracks, (4) magnet, (5) magnet support, (6) piezo, (7) aluminium holder, (8) hat-shaped aluminium piece; electrical shield, (9) and (10) insulating Macor ring, and (11) Invar base.

tion (4), is suspended from an Eddy-current damping mechanism (5). Thin, silica coated capillaries (6) lead from a gas feedthrough (7) on the flange to the reactor volume. The silica again provides chemical inertness. In order to facilitate the transfer of the sample holder into and out of the STM, (I) the reactor has to be opened, as shown in part D of figure 2, and (II) the STM portal should be mechanically locked to the backbone. This can be done by a combination of two bellows (8, 9), which can be separately inflated and deflated. Inflating bellow I (8) closes the reactor, whereas deflating opens it. Inflating bellow II (9), the STM portal is locked to the backbone, deflating it releases the STM portal to the springs of the Eddy-current damping system. The volume of the bellows is separated from the UHV; bellows I is fed via a capillary connected to the gas feedthrough (7), and bellows II has a separate, direct feedthrough (10). The capillaries connecting the inlet and exhaust of the reactor volume and bellow I are wound as weak springs around the por-

tal, to prevent mechanical vibrations from coupling into the ECD and the STM during operation.

We use fast electronics, provided by Leiden Probe Microscopy BV [75], so as not to limit the maximum scan speed by the electronics.

2.3.3 Gas manifold

For residual gas analysis with the QMS, we wanted a fast response time and accurate reading of the measured spectra of the reactants and reaction products. This implied that, for the layout of a gas manifold, one should not include dead or badly refreshed volumes, which could contaminate the QMS measurements and flatten out sharp peaks. For applications in gas chromatography and high performance liquid chromatography, for example, a wide range of commercially available tubing, connection pieces and cross pieces, filters, and several types of valves have been developed, which have extremely low dead volume. Figure 2.5 shows the layout of such a valve in cross section, a 3D rendition, and a photo. The crucial element is a rotor (fig. 2.5 B) with a conical polymer surface, containing an engraved pattern. This rotor is pressed inside a metal body, to ensure a leak tight seal. Rotation of the rotor accesses different channels drilled in a symmetric radial pattern of the metal body. These channels connect to each other via the engraved pattern on the polymer body. Figure 2.5 C shows different flow path possibilities in such a valve, in which the arrows indicate the flow path. As can be seen, no dead volume inside the valve is enclosed at any time by the channels not in use. To fit our specific needs, as mentioned in the specifications section, the engraving on the polymer surface of the rotors had to be modified [83].

Due to the choice of working with GC valves, the outer diameter tubing size was fixed to 1/16". Concerning the inner diameter, a too small diameter would require large pressure differences and be hard to shape mechanically, whereas a too large diameter would also include a large volume and possible buckling during shaping.

To control the flow and pressure inside the reactor volume in the STM, we used mass flow controllers (MFC) and back pressure controllers (BPC), which were provided by Bronkhorst Hi-Tech [84]. The controllers used are the ones with highest accuracy and lowest ranges available at the time of writing. We used two types of MFC's: ones with a laminar flow element (0 to 30 ml_n/min), and ones without (0 to 10 ml_n/min). They have a full scale accuracy of 0.1 % and, for flows >1 mln/min, a full scale accuracy of

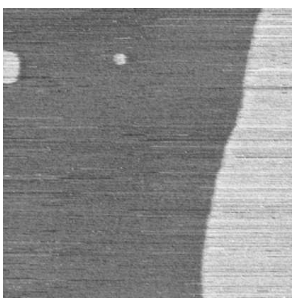

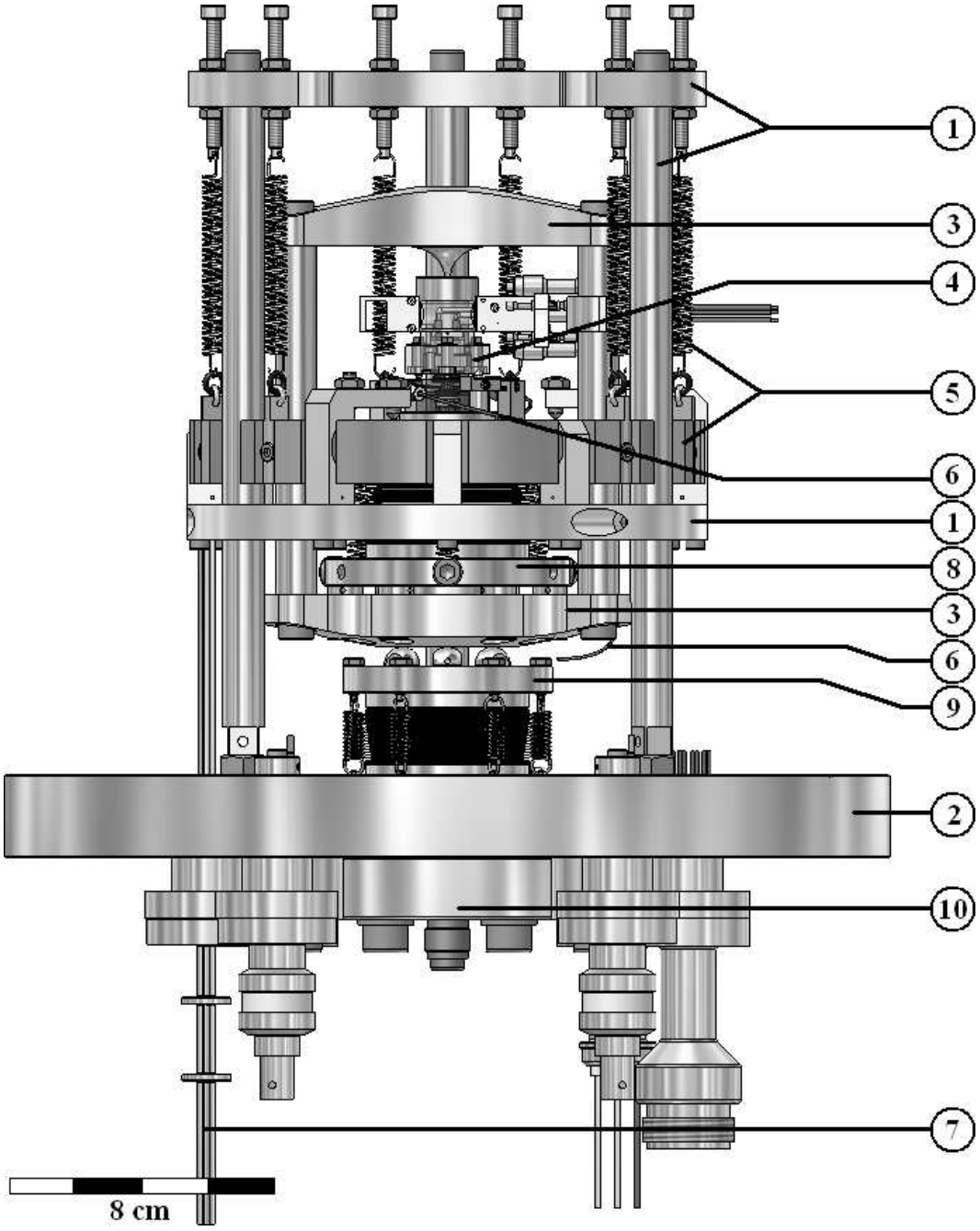

Figure 2.4: STM insert. (1) Backbone, (2) STM flange, (3) STM portal, (4) STM/ Kalrez seal/ sample holder combination (photo's (1), (4), and (6) in figure 2.2), (5) Eddy-current damping mechanism, (6) capillaries, (7) gas feedthrough, (8) bellow I, (9) bellow II, (10) gas feedthrough for bellow II.

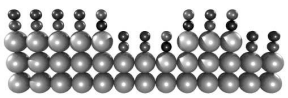

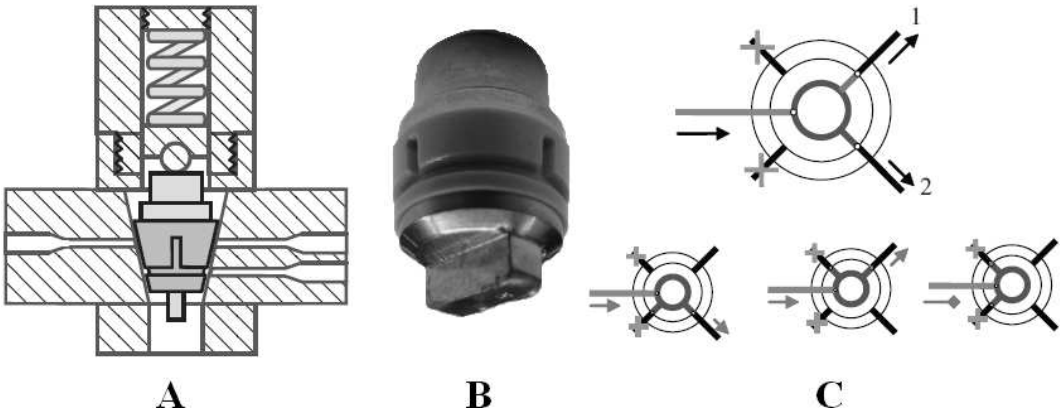

Figure 2.5: (A) Schematic cross section of a Valco multiposition GC valve, (B) photo of the actual rotor, showing the engraving, (C) flow schemes through a custom GC valve.

1 %. The BPC has an accuracy of 0.5 % full scale and a lower limit of 2 mbar.

Using these components, the topography of the gas system took shape as in figure 2.6. The gases oxygen, CO, NO, and hydrogen, stored in compressed gas tanks, first pass a reduction valve. Then, the flow through valve (1) may select one of the gases to store it in the pulse line. A set of MFC's sets a flow for each gas before this gas enters the mixing valve (2), which selects the gas mixture desired in the reactor. The layout of the mixing valve is such, that the non-used gases do not generate a dead volume. The flow exiting the mixing valve is the sum of the flows from the individual selected gases entering the RS valve (3). This valve provides the possibility for gas flow through the reactor, a shunt line, or both. By using the shunt line, in combination with the reactor line, extreme gas ratios are available to the reactor, which would otherwise need extreme MFC settings – the biggest part of the gas mixture then being pumped away via the shunt line. The pressure in the reactor is controlled by a back pressure controller, exiting into a pump, which creates the flow. The injection valve (4) allows us to deliver a sharp pulse of gas to the surface quickly. The volume of the twisted gas line in the schematic is as large as the volume of the reactor, and since this volume is included in the gas line to the reactor, upon actuating the injection valve, flow and pressure will still be fully controlled, delivering the pulse. On the reactor exhaust line, a capillary taps a small part of the exhaust gas for residual gas analysis with a QMS, which will be described in the next paragraph.

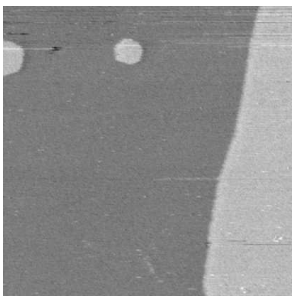

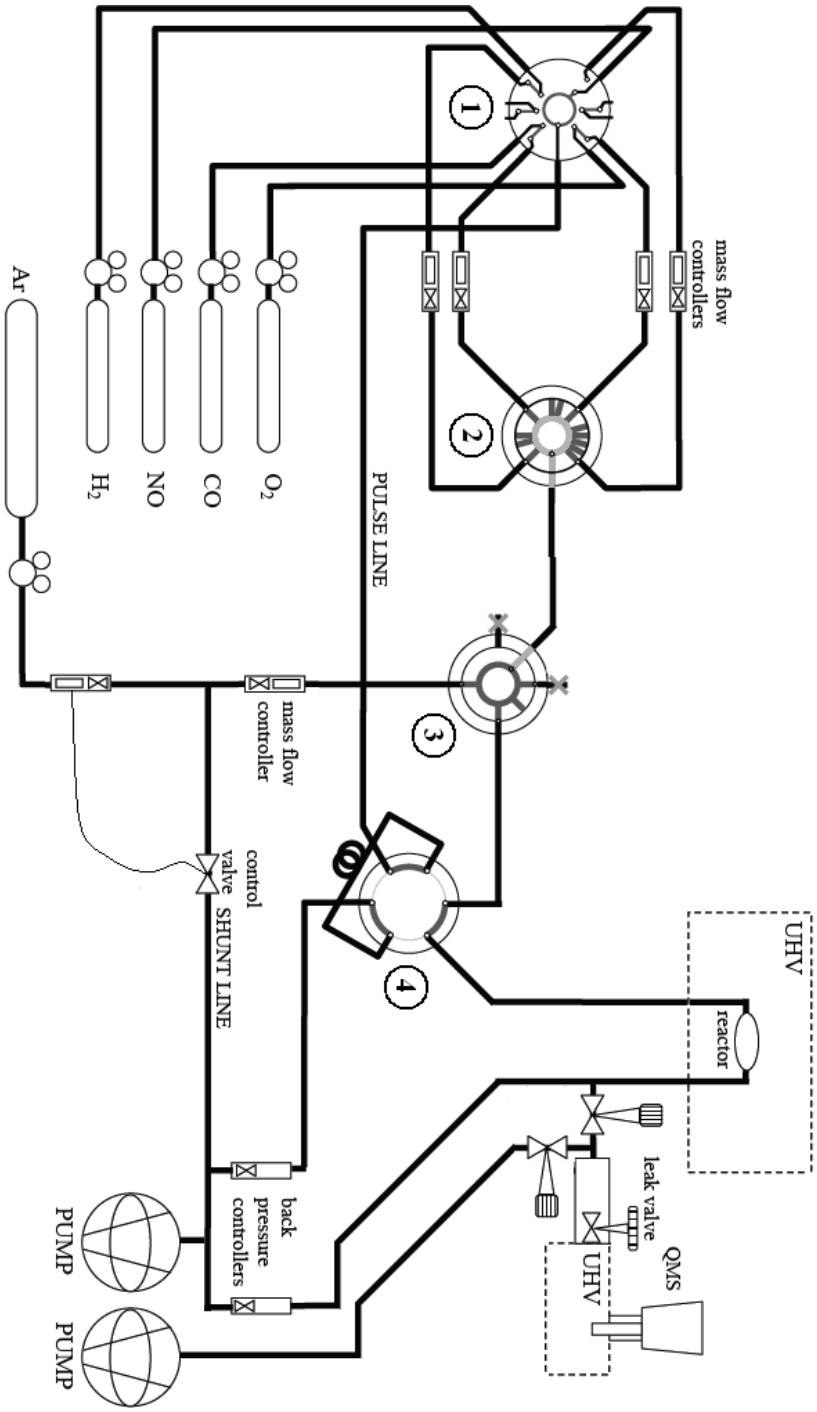

Figure 2.6: Gas manifold layout. GC valves are (1) flow through valve, (2) mixing valve,(3) RS valve, and (4) injection valve.

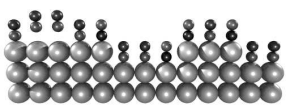

2.3.4 Residual gas analysis

Given that we wanted to correlate changes in the structure of a catalyst surface with changes in the reaction rate, we wanted to perform residual gas analysis with a QMS, simultaneously with the STM measurements, as described in the specifications section. The easiest method is to connect the QMS to the UHV system, and then leak a fraction of the exhaust gas into the chamber, either by creating a non-perfect reactor seal, or by guiding part of the exhaust line to a leak valve on the vacuum chamber. This, however, is not a desirable solution, because of two flies in the ointment. Firstly, the QMS has a cooling fan, which couples mechanical vibrations into the STM, and secondly, the chamber is solely pumped by ion pumps during an STM experiment. Ion pumps actually produce CO, which is one of the gases we want to use during an experiment. Worse still, this production also contains a memory effect: the amount is not constant in time, and thus separation from the gases used in an experiment is unfeasible. Also, ion pumps show great differences in pumping efficiency for different gases – O_2 is pumped about five times as efficiently as CO – which makes them impractical for use during residual gas analysis. Realizing this, we mounted the QMS on a separate small UHV chamber, with a pressure gauge and a gas line tapped from the reactor exhaust. This is the QMS chamber, which can be seen in figure 2.6 in the gas manifold layout. The gas line has a large resistance, in order not to influence pressure and flow control of the main line. Just before entering the QMS chamber, via a leak valve, a rotary pump creates a flow, keeping the response time down.

2.4 Performance

The first high-pressure experiment performed with the instrument was the catalytic oxidation of CO by oxygen on a Pt(110) surface. Since this is a well-known reaction system [27, 76–82, 125], it serves as a useful experiment to investigate the STM performance. Images from this experiment will be used here for this purpose only; further interpretation of this experiment will be discussed in chapter 4. Before describing the STM performance, we will start with the performance of the UHV system and gas manifold.

2.4.1 UHV system and gas manifold

The UHV system routinely reaches its base pressure of $1 \cdot 10^{-10}$ mbar after a bake-out of 48 hours at 120℃. During high-pressure experiments, the Kalrez

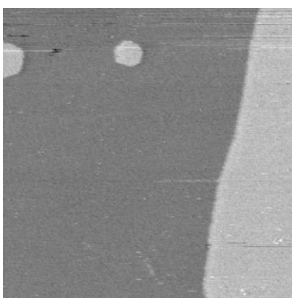

ring provides a leak tight seal – the pressure in the chamber does not exceed $1 \cdot 10^{-8}$ mbar. The bellows used to open and close the reactor, and to lock the STM into, and release the STM from, the Eddy-current damping mechanism are fully leak tight and operate smoothly. A pressure of 1.5 bar is needed to inflate them, while the end pressure of a small roughing pump is enough to deflate them. Additional springs are needed to pull down the bellows, compensating for the absence of air pressure on the bellows in the UHV environment.

The time constant of gas composition changes in the reactor depends on the total volume of the gas system. This depends primarily on the inner diameter choice of the tubing. The main consideration for this is that the tubing can withstand 0 to 5 bar under a 10 bar·ml/min flow, without a large pressure drop. Secondly, the impedance of the tubing should not be too large, since this will eventually lead to a lower flow. The dependence of the pressure drop over the tubing can be determined from the friction factor, which is defined as f in $F_k = AKf$, with F_k the force exerted on the tubing, A the inner area of the tubing, and K the characteristic kinetic energy for the gas flowed. The friction factor can be expressed as a function of the Reynolds number, which provides information about pressure drops. The flow rate depends on the impedance Z of the tube, given by equation 2.4.1 [85]. Control valves can be seen as increasing impedance when they gradually close.

$$Z = \frac{128\eta}{\pi} \frac{L}{D^4 \overline{\overline{P}}}. \tag{2.4.1}$$

Taking these considerations into account for the tubing inner diameter choice (0.53 mm), we obtain a response time between changing the gas composition in the reactor line and a change in readout of the QMS of 6 to 30 seconds, depending on the flow and pressure settings. In figure 2.7, a typical time trace, measured during CO oxidation, is shown. As can be seen, a full switch from a CO-rich to an O_2-rich environment takes 3.5 seconds, indicating the low volume within the gas system and low mixing between interfaces of different gas compositions.

The modified GC valves, after having been rotated a few hundred times, still exhibit a leak rate of 10^{-9} mbar·l/s. Further lifetime determination has to be investigated during use. The valve actuation was chosen to be electromotive, because of its simplicity relative to gas actuated motion. We chose high torque switching over high speed switching, because high torque guarantees a continuous leak tightness of the valves. The switching times

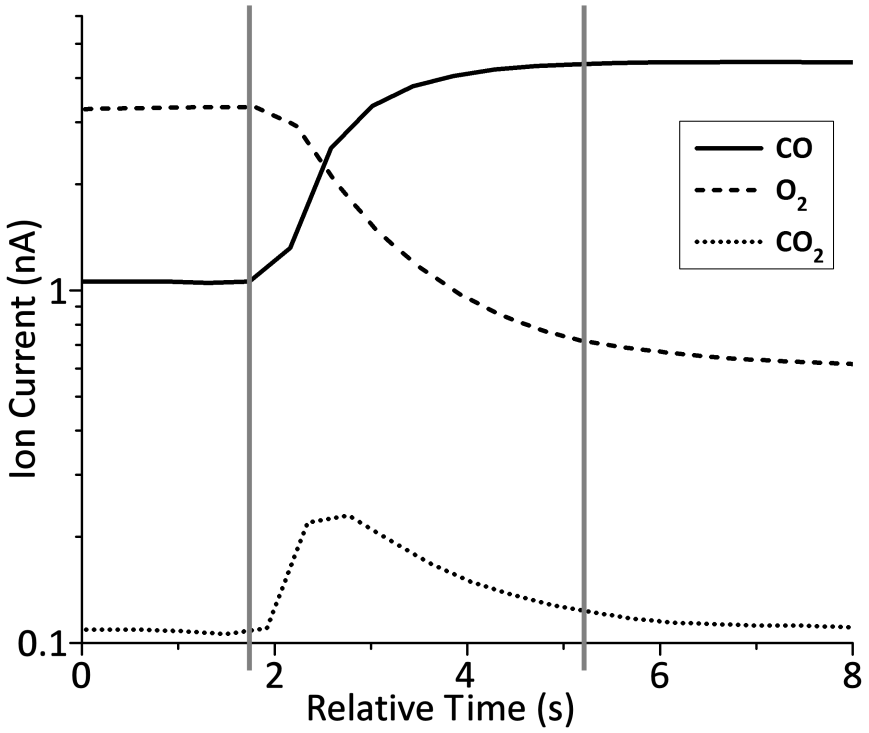

Figure 2.7: Time trace of the gas cabinet – gas cabinet performance

are between 0.1 and 1 second. The flows are interrupted and affected by switching the valves, mainly caused by this long switching time. However, at present, the effects of these are buffered in the volume of the gas lines, so that sudden large changes in pressure in the reactor due to valve switching do not lead to tip crashes.

2.4.2 STM

In testing the performance of the STM, we have used the standard surfaces of HOPG and Au(111), as well as the Pt(110) surface under CO oxidizing conditions. Using figure 2.8, which shows eight STM images taken under the various conditions, the STM performance will be discussed in this section.

Starting from images A and B, showing the Au(111) surface at a scale of 25 nm x 25 nm and 2.5 nm x 2.5 nm, the z-resolution of the microscope can be determined. In the large scale image A, the STM clearly identifies the well known herringbone reconstruction[1] occurring on Au(111), with a surface

[1]I will discuss the herringbone reconstruction on the Au(111) surface in more detail in

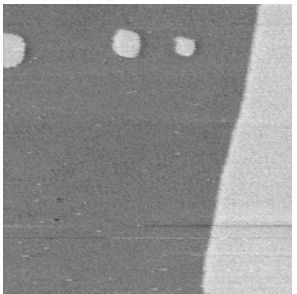

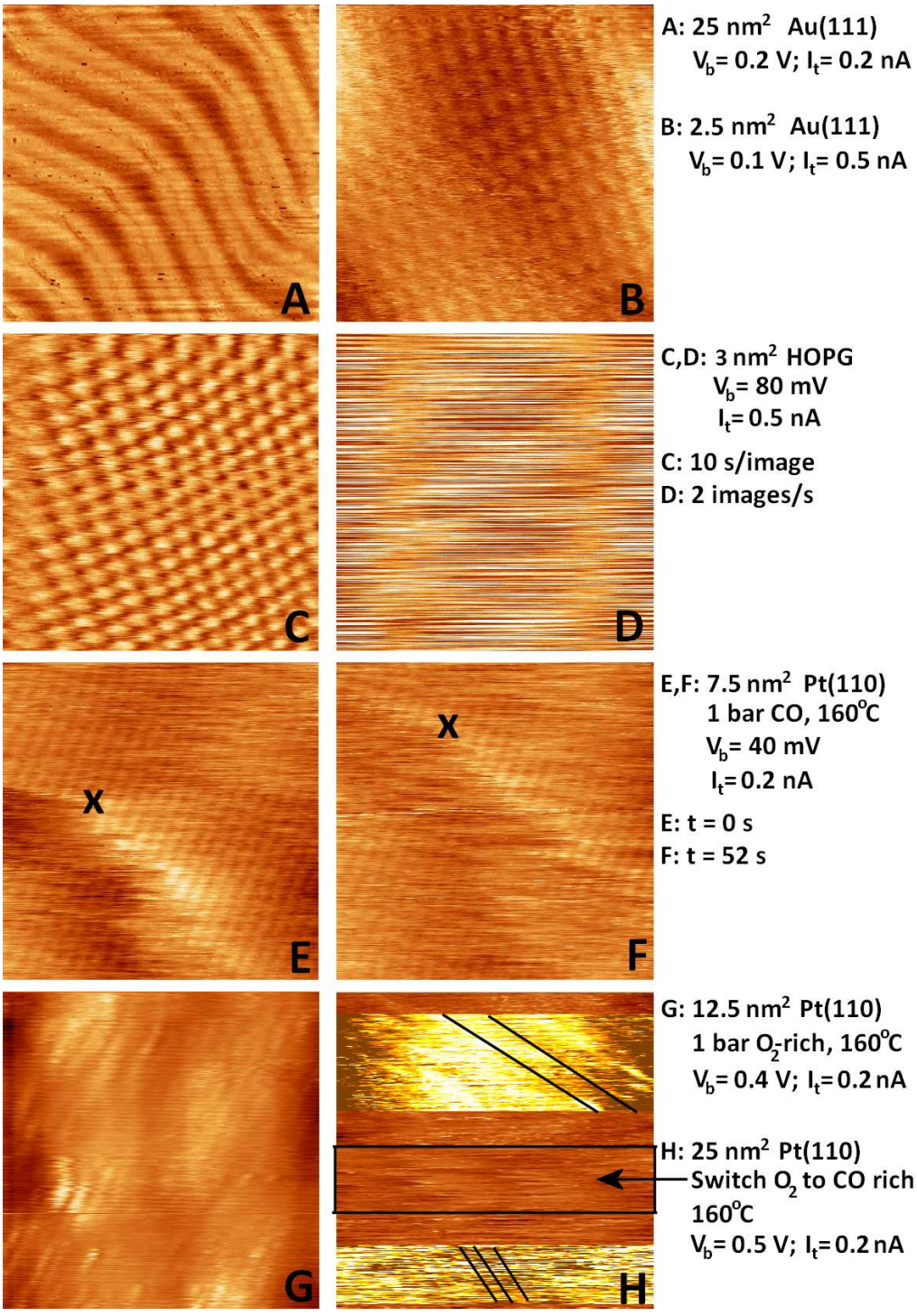

Figure 2.8: STM performance.

chapter 5

corrugation of 35 pm. Within the reconstruction, as can be seen in the small scale image B, our STM is capable of resolving the atoms, which have a surface corrugation of 6 pm (0.06 Å). In terms of real height sensitivity, however, we need to quantify the current noise level. To determine this quantity, a height profile of the current signal from the preamplifier was measured on a very flat, small area on the surface. In this way, only the noise in the STM contributed to the "structure" in the current image. The current sensitivity, or minimum corrugation resolution, can now be determined via equation 2.4.2 [86].

$$\frac{\Delta I}{I} = 2K\Delta d \approx \sqrt{\Phi}\Delta d. \tag{2.4.2}$$

ΔI is the peak to peak current variation, I the current set point, K the characteristic exponential inverse decay length, Δd the height sensitivity, and Φ the work function. From image B, the peak to peak value was determined to be I_{RT} = 40 pA at a current set point of 0.5 nA. In combination with the work function for gold of 5.1 eV [87], this leads to a height sensitivity Δd_{Au} = 0.035 Å. This surpasses our requirement of 0.1 Å, but it should be kept in mind that these images were obtained at room temperature in an undefined vacuum – the vacuum was undefined, since the reactor volume, which during scanning was separated from the UHV environment, was not being pumped – and we want the requirement fulfilled under realistic catalytic conditions, which will be discussed later in this section.

Images C and D, in figure 2.8, show the atomically resolved HOPG surface. Image C is a typical image, taken at a speed of 20 seconds per image. We increased the scan speed until the point where the atomic corrugation would not be too much predominated by the increasing noise level, resulting in image D. This image was obtained with a speed of 2 images per second, thereby fulfilling our goal of 1 image per second.

A very important issue in STM is thermal drift. Firstly, I would like to mention the choice of very low thermal expansion coefficient materials, such as zerodur, in the design of the sample holder and the reactor. This allowed us to stabilize the microscope within 15 minutes from the point where we started heating the sample to temperatures above 150℃, starting from room temperature. In our type of experiments, we can also expect slight temperature variations because of increased or decreased reactivity of a catalyst, for instance, after a phase transition has occurred at the surface. The way in which we minimize the influence of modest temperature changes at the surface, during a reaction, is a configuration in which we have to put a lot

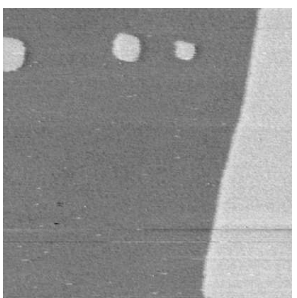

of power into heating the sample. The modest heating created by changing properties of the catalyst will therefor not exhibit a heavy effect on the total temperature of the system, leading to a thermally stable environment, with low drift. This effect can be seen in images E and F, which show the Pt(110) surface, exposed to a flow of 1 bar of CO at 430 K. However, let me first point to the fact that, as can be seen from images E and F, we atomically resolve this surface under reaction conditions; using equation 2.4.2, with a measured $I_{HT,P}$ of 60 pA at a current set point of 0.2 nA, and a platinum work function of 5.84 eV [87], the minimum corrugation resolution $\Delta d_{HT,P}$ = 0.12 Å, which matches our requirement of 0.1 Å under realistic conditions. Coming back to the thermal drift, the time elapsed between image E and F is 52 seconds, during which time the step on the surface, marked by x, has moved 1.8 nm. This means that the drift is 2.1 nm/min, which is significantly lower than the number we aimed for. The drift in the z direction, obtained by scanning until we had to retract the tip manually, because it hit its contraction limit, is about 0.5 μm/h, also satisfying our wish. All in all, in terms of thermal stability, the STM behaves better than we had initially aimed for and expected.

Finally, image G and H show the effects on the imaging during various and changing gas compositions. Image G shows the same Pt(110) surface under a flow of oxygen, while image H was made during a transition from an oxygen rich flow to a CO rich flow. It can immediately be seen that the image quality is compromised with respect to the other sets of images in figure 2.8. This is mainly caused by the tip, in this case a cut platinum iridium tip, which also oxidizes and participates in the reaction.

In conclusion, the ReactorSTM^{TM} Mark II fully meets the specifications as we have defined them in section 2.2 fully, which make this a very versatile machine. It is the only one of its kind which can atomically resolve catalytic surfaces under realistic conditions, with fast switching times, and has fast response times of the gas manifold and the quadrupole mass spectrometer.

2.5 Outlook

At present, we are studying various catalytically activated reaction systems, such as oxidation/ reduction processes, Fischer-Tropsch synthesis, and hydrodesulphurization, with the ReactorSTM^{TM} Mark II. The system, as has been shown, for instance, in images G and H of figure 2.8, also has its limitations. Firstly, the maximum operating temperature (600 K) and pressure

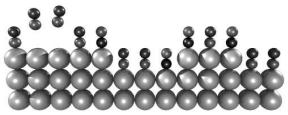

(5 bar) range of the machine is just within the scope of industrial conditions. The main reasons are the use of Kalrez seals and joints, which cannot withstand more temperature or pressure. Our next set of requirements, for ReactorSTM^{TM} "Mark III", is to be able to atomically resolve the structure of a catalyst at pressures $>$ 100 bar and temperatures $>$ 900 K, opening a world of interesting catalytic systems, which can then be studied under relevant conditions. In addition, we want to be able to scan at video rate or faster, which might be assisted by the use of MEMS-based scanners, currently under development within our research group and the NIMIC consortium [88].

Another limitation is the type of tips we use at this moment – image quality is often compromised by the instability of the tip apex, caused by high atom mobility on the tip, reactivity of the tip, or surface transitions to, for example, surface oxides on the tip. Ideally we would like to use a sharp, etched, inert tip. Tungsten is easy to etch and is a very stiff material generally used in ultrahigh vacuum STM experiments, but in our case we cannot use tungsten, because of its instability in certain gas ratios. In an oxygen rich gas flow, for instance, it will immediately be covered by a thick insulting tungsten oxide. Currently we are investigating the options of using gold tips, gold plated tungsten (or other materials) tips, and etched platinum iridium tips. But so far the results are not satisfying enough to replace the simple recipe of mechanically sheared PtIr tips.

As a final remark, we are currently developing and constructing a high-pressure AFM, which can be integrated into an already existing copy of the UHV system. This instrument will allow us to investigate, for example, supported catalytic active nano-particles on non-conducting materials, bridging the materials gap, which is impossible for the STM, since it needs a conducting surface. We also plan on eventually developing an STM/AFM combination. Both the ReactorSTM^{TM} and ReactorAFM^{TM} will become commercially available from Leiden Probe Microscopy [75].

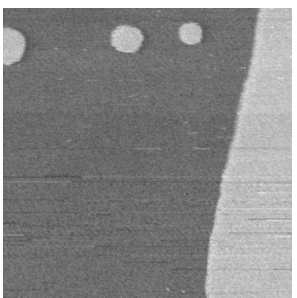

Chapter 3

NO reduction on Pt(100), using the ReactorSTM Mark I

This chapter covers an investigation of the reduction of nitric oxide by carbon monoxide, on a Pt(100) model catalyst, at atmospheric pressure (1.25 bar). A combination of high-pressure scanning tunneling microscopy (Mark I) and simultaneous mass spectrometry has been used to correlate observations of the surface structure with the reaction rate and reaction mechanism. The STM images suggest that, depending on the precise composition of the reactant gas mixture, the Pt(100) surface switches between the quasi-hexagonal structure, characteristic for this surface in vacuum, and the bulklike (1x1) structure, which is 20% less dense. The reaction rates, which were observed, are interpreted in the framework of classical Langmuir-Hinshelwood kinetics, on both surface structures.

3.1 Introduction

Platinum is a good catalyst for many chemical reactions, such as CO oxidation and NO reduction. These are two of the three classes of reactions that take place in the three-way car catalyst, in which small, supported platinum, palladium, and rhodium particles are the active elements [5, 91, 92]. In this chapter, we have concentrated on NO reduction, i.e. the conversion of nitric oxide by carbon monoxide to nitrogen and carbon dioxide. Although rhodium is the main catalyst for this reaction, the (100) surface of platinum is also known to reduce NO [93, 94]. Both experimental and theoretical studies have been devoted to this reaction system. The experimental studies include temperature programmed desorption [95–97], low energy

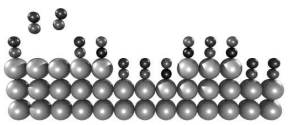

electron diffraction (LEED) [95, 98, 99], infrared reflection-adsorption spectroscopy [100], single-crystal adsorption calorimetry [99], scanning tunneling microscopy (STM) [101, 102], X-Ray photoelectron spectroscopy [103], mass spectrometry [104], molecular beam studies [97], and 3D atom probe measurements [105]. Theoretical studies include density functional theory and Monte Carlo simulations, providing various models for the active sites and the reaction mechanisms [99, 106–111].

Pt(100) can catalyze the complete conversion of NO and CO to N_2 and CO_2. The reaction is autocatalytic, and it has been proposed to be promoted by reaction intermediate species or structures like step sites [95, 101].

Clean Pt(100) exhibits a surface reconstruction, which features a quasi-hexagonal monolayer on top of the square lattice below [102, 109]. This reconstruction makes the top layer 20% denser than the unreconstructed surface. The quasi-hex reconstruction is lifted by exposing the surface to adsorbates, for instance CO, O_2, and NO, adding steps to the surface by creating adatom or vacancy islands and terrace roughness [97, 107, 114]. At low pressures, dissociation of NO only takes place on the square lattice [96] – Pt(111), which resembles the reconstructed Pt(100) surface, is not very reactive. The reaction is believed to be active above 400K; below this temperature, NO dissociation does not occur at low pressures [96, 100, 103, 107].

Most previous experiments, with surface-science techniques on the NO-CO reaction, have been performed at low pressures, since most of the employed techniques cannot tolerate high pressures. However, practical catalysts, such as the three-way catalyst, operate at high pressures, for example at and above atmospheric pressure. Recent studies on CO oxidation have revealed a strong pressure-gap effect between the traditional low pressures and the regime of atmospheric pressures. An alternative catalytic mechanism was identified at high pressures, accompanied by a significant change in the reaction rates [27, 36, 112, 113]. In the light of these observations, the present study on NO reduction by CO on Pt(100) has been performed at elevated temperature and atmospheric pressure.

3.2 Reaction Kinetics

The reduction of NO by CO is believed to proceed via Langmuir-Hinshelwood (LH) kinetics, described by the following reaction equations [93, 94, 104, 106, 108, 110].

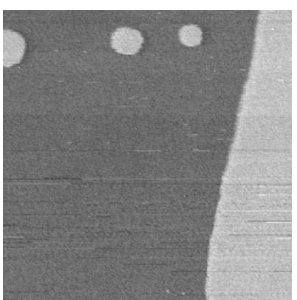

$$
\begin{array}{lll}
CO_{(g)} + * & \rightleftharpoons_{k_{-1}}^{k_1} & CO_{(ads)} \quad (1),\\
NO_{(g)} + * & \rightleftharpoons_{k_{-2}}^{k_2} & NO_{(ads)} \quad (2),\\
NO_{(ads)} + * & \rightleftharpoons_{k_{-3}}^{k_3} & N_{(ads)} + O_{(ads)} \quad (3),\\
N_{(ads)} & \rightleftharpoons_{k_{-4}}^{k_4} & \frac{1}{2}N_{2\ (g)} + * \quad (4),\\
CO_{(ads)} + O_{(ads)} & \rightleftharpoons_{k_{-5}}^{k_5} & CO_{2\ (g)} + 2* \quad (5).
\end{array}
$$

We will refer to this pathway for the formation of N_2 as pathway I. An alternative pathway (II) for the creation of N_2 is:

$$
\begin{array}{lll}
NO_{(ads)} + N_{(ads)} & \rightleftharpoons_{k_{-6}}^{k_6} & N_2O_{(ads)} + * \quad (6),\\
N_2O_{(ads)} & \rightleftharpoons_{k_{-7}}^{k_7} & N_{2\ (g)} + O_{(ads)} \quad (7),\\
N_2O_{(ads)} & \rightleftharpoons_{k_{-8}}^{k_8} & N_2O_{(g)} + * \quad (8).
\end{array}
$$

In reaction step i, k_i, and k_{-i} are the rate constants for the forward and reverse directions, respectively; a free site at the surface is indicated by $*$. For this combination of reaction steps, it is straightforward to derive the following equations for the formation rates of CO_2 and N_2 in the quasi-stationary regime[1].

$$
R_{CO_2} = k_3 \frac{k_2}{k_{-2}} \frac{p_{NO}}{\left(1 + \frac{k_1}{k_{-1}} \cdot p_{CO} + \frac{k_2}{k_{-2}} \cdot p_{NO}\right)^2}. \tag{3.2.1}
$$

$$
\begin{aligned}
R_{N_2} = \quad & \frac{k_2 p_{NO}}{4k_{-2}k_4 \left(1 + \frac{k_1}{k_{-1}} p_{CO} + \frac{k_2}{k_{-2}} p_{NO}\right)^2} \\
& \times \left[\left(\frac{1}{2} - \frac{k_8}{k_7 + k_8}\right) k_6^2 \frac{k_2}{k_{-2}} p_{NO} \right. \\
& - \left. \left(\frac{1}{2} - \frac{k_8}{k_7 + k_8}\right) k_6 \sqrt{1 + \frac{8k_4k_3k_{-2}}{k_6^2 k_2 p_{NO}}} \right] \\
& + \frac{k_3 k_2 p_{NO}}{2k_{-2} \left(1 - \frac{k_1}{k_{-1}} p_{CO} + \frac{k_2}{k_{-1}} p_{NO}\right)^2}.
\end{aligned} \tag{3.2.2}
$$

In these equations, we have made the assumptions (1) that the reaction products immediately leave the surface, thus $k_{-4} = k_{-5} = k_{-7} = k_{-8} = 0$, (2) that the coverages of N and O are negligibly small, (3) that NO and CO adsorption and desorption directly reach their equilibrium state, and (4)

[1]The derivation of R_{CO_2} and R_{N_2} according to equations 3.2.1, 3.2.2, and 3.2.3 is included in the appendix ("LH calculation") at the end of this chapter

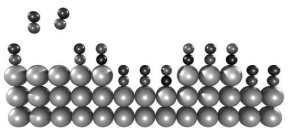

that thus the remaining reaction constants determine the overall reaction rate. The more complex structure of the formation rate for N_2 reflects the fact that it combines both pathways (reactions 4 and 7), whereas the CO_2 is only formed via pathway I (reaction 5). It is instructive to consider the N_2 formation rate in two limiting situations, namely when all N_2 is formed via the first pathway (k_4 dominant), or when all N_2 is formed via the second (k_4 negligible). In these two cases, equation 3.2.2 reduces to

$$R_{N_2} = \begin{cases} \dfrac{k_3}{2}\dfrac{k_2}{k_{-2}}\dfrac{p_{NO}}{\left(1+\frac{k_1}{k_{-1}}\cdot p_{CO}+\frac{k_2}{k_{-2}}\cdot p_{NO}\right)^2} & k_4 \text{ dominant} \\ \dfrac{k_3 k_8}{k_7+k_8}\dfrac{k_2}{k_{-2}}\dfrac{p_{NO}}{\left(1+\frac{k_1}{k_{-1}}\cdot p_{CO}+\frac{k_2}{k_{-2}}\cdot p_{NO}\right)^2} & k_4 \text{ negligible.} \end{cases} \tag{3.2.3}$$

Interestingly, in each of these two limiting situations, the N_2 formation rate varies with the partial pressures of NO and CO, in precisely the same way, identical to the dependence of the formation rate of CO_2 on these partial pressures. Combining the relevant reaction rate constants in three parameters K_i ($i = 1..3$), equations 3.2.3 and 3.2.1 can be rewritten, giving

$$R_{N_2}, R_{CO_2} = K_1^{N_2,CO_2}\frac{p_{NO}}{\left(1+K_2\cdot p_{CO}+K_3\cdot p_{NO}\right)^2}. \tag{3.2.4}$$

For reaction pathway I, $K_1^{N_2} = \frac{k_3 k_2}{2k_{-2}} = \frac{1}{2}K_1^{CO_2}$. For reaction pathway II, $K_1^{N_2} = \frac{k_3 k_8 k_2}{(k_7+k_8)k_{-2}}$, and $K_1^{CO_2} = \frac{k_3 k_2}{k_{-2}}$ (the same as for pathway I). This means that $K_1^{N_2}$ and $K_1^{CO_2}$ depend, in all cases, directly on the NO dissociation rate (k_3), and on the reaction constant $\frac{k_2}{k_{-2}}$, for NO adsorption/desorption. In the case of pathway II, $K_1^{N_2}$ is also determined by the ratio between the rate constants for N_2 and N_2O formation, via the factor $\frac{k_8}{k_7+k_8}$. The only difference between $K_1^{N_2}$ for the N_2 formation rates at high and low k_4 is a mere factor $\frac{2k_8}{k_7+k_8}$. For intermediate k_4-values, we have been forced to return to the more complex form of equation 3.2.2. In all cases, $K_2 = \frac{k_1}{k_{-1}}$ is the reaction constant for CO adsorption/desorption, and $K_3 = \frac{k_2}{k_{-2}}$ is the reaction constant for NO adsorption/desorption.

Since the form of the equations, for R_{N_2} for both pathways and R_{CO_2}, are the same, this form will be used later, in an attempt to fit the experimental N_2 and CO_2 formation rates, using the K_i's as fitting parameters. As mentioned, the formation rate for CO_2 is double the first N_2 formation rate

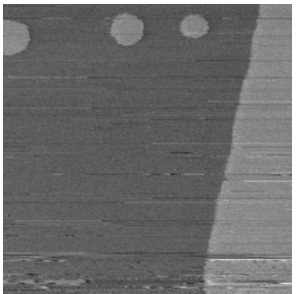

of equation 3.2.3, so that, if the N_2 formation rate is dominated by the first pathway, $R_{CO_2} = 2R_{N_2}$.

We close this section by noting that a more complete description of the set of reaction rates might require the introduction of non-linear elements in one or more reaction rates, since at low pressures, bi-stability and oscillations have been observed [97–99, 111, 115].

3.3 The Pt(100) sample

In this work, a platinum single crystal, cut and polished with the (100) surface orientation, was used. It was prepared in the UHV chamber by multiple cycles of (1) argon ion sputtering, at an ion energy of 600 eV, (2) annealing in a $1 \cdot 10^{-6}$ mbar oxygen atmosphere at 1000 K, and (3) flash annealing to a somewhat higher temperature in UHV. Low energy electron diffraction (LEED), in combination with Auger electron spectroscopy, was used to verify the crystalline quality and the cleanliness of the sample surface, prior to transferring it to the ReactorSTM. A typical LEED pattern is shown in figure 3.1 A.

Pt(100) reconstructs into a 20% denser quasi-hexagonal lattice, with reported overlayer periodicities of (1x5), (5x20) and (5x25) rotated 0.7° with respect to the underlying lattice [116, 117, 121]. This can generally be written in matrix form as $\left(\begin{smallmatrix} N & 1 \\ -1 & 5 \end{smallmatrix}\right)$. A ball model of this structure is depicted in figure 3.1 B. Because the symmetry of the quasi-hexagonal overlayer is different from the symmetry of the square lattice below, a Moiré pattern is obtained, when imaging the reconstructed surface. Figure 3.1 C shows a 50.1 nm x 50.1 nm STM image exhibiting this Moiré pattern clearly, from which we can determine the commensurate unit cell. The unit cell is defined by the rectangle (d_1, d_2), which includes two lines of the Moiré pattern in the direction of d_1. The reason for this can be seen in figure 3.1 D: every second segment along d_1, in between two pattern lines d_2, has a broader appearance in the STM image, so in order for the unit cell to be commensurate, we have to include $2d_1$. To determine the number of platinum atoms n_i along d_i, we count the number of lines N_i along a distance D_i, for $i = 1, 2$, and use the equation $n_i = D_i/(N_i d_{Pt,i})$, in which $d_{Pt,i}$ is the distance between the platinum atoms. For direction d_1, the inter platinum distance corresponds to the bulk distance, which is 2.77 Å [118]. For direction d_2, we have to take the hexagonal packing into account, which leads to $d_{Pt,2} = 0.5\sqrt{3} \cdot 2.77 = 2.40$ Å. Doing the exercise, a periodicity of (4x25) for the commensurate unit cell

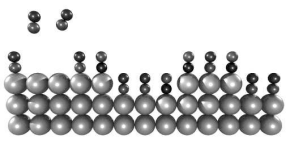

was obtained, coinciding well with the literature.

Figure 3.1 E shows a height profile of image C along the line (B), exhibiting a (monatomic) step height on Pt(100) of 2 Å. This coincides with the reported monatomic step height on Pt(100) [121]. Furthermore, figure 3.1 F shows an STM image in which atomic row resolution on the clean Pt(100) crystal was obtained. A row distance of 5.1 Å, which corresponds to twice the distance between the hexagonal packed rows, has been found. Atomically resolved STM images, obtained under UHV conditions, have shown that every second atomic row along this direction appears higher than its neighboring rows [120]; this indicates that only the higher rows were imaged with the ReactorSTM.

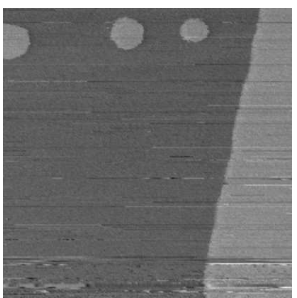

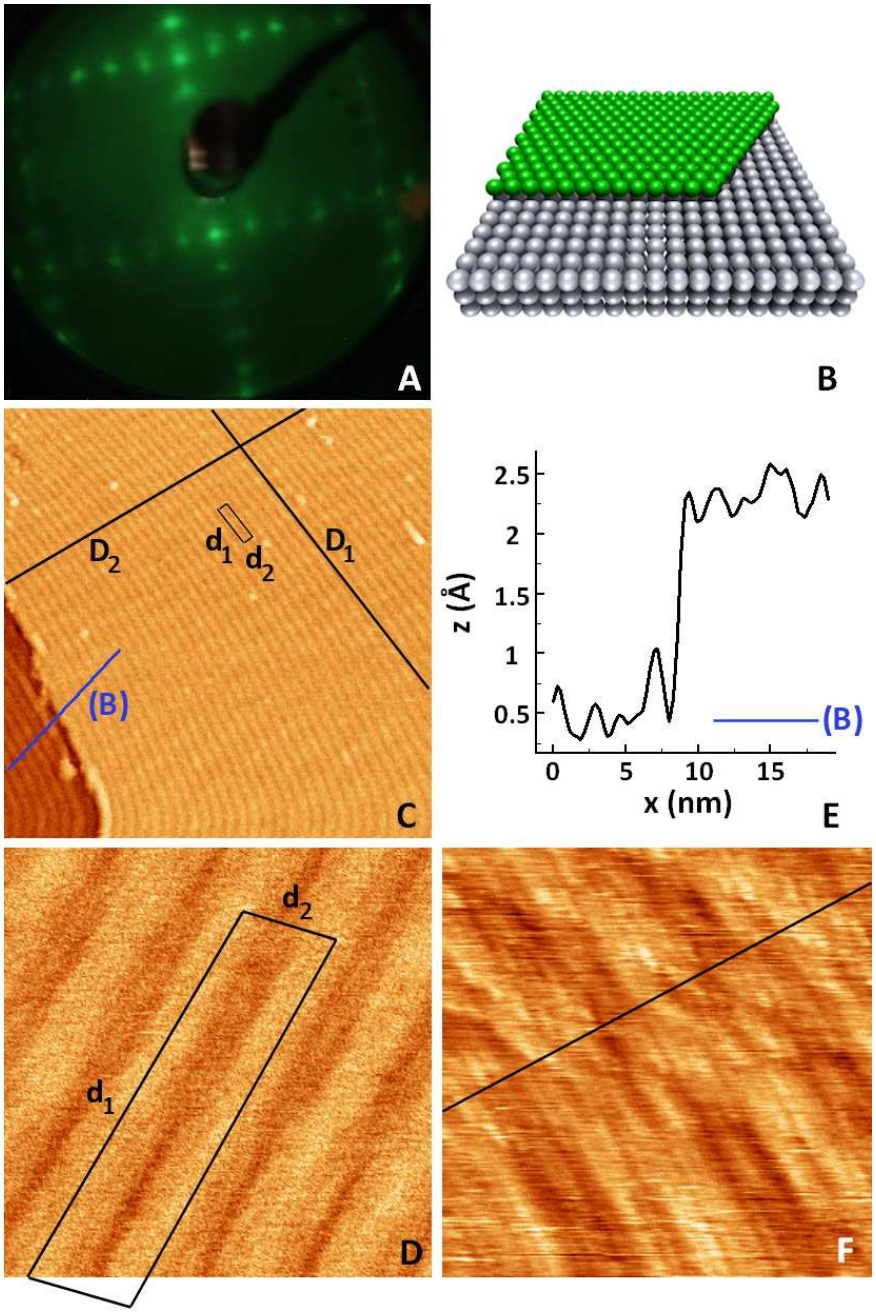

Figure 3.1: (A) A typical LEED pattern for clean Pt(100). Due to the incommensurate overlayer, with respect to the bulk, the spots are split. (B) A ball model of the reconstructed Pt(100) surface showing the quasi-hexagonal overlayer on the square lattice below. (C) A 50.1 x 50.1 nm^2 STM image of the reconstructed Pt(100) surface. (D) A 5.5 x 5.5 nm^2 STM image, indicating the unit cell of the quasi-hexagonal overlayer (d_1, d_2), also indicated in image C. (E) The height profile of line (B) in image C, showing a step height of 2 Å on Pt(100). (F) A 5.5 x 5.5 nm^2 STM image of Pt(100), on which we obtained atomic row resolution on the reconstructed Pt(100) surface. For all STM images shown here, $V_b = -100$ mV, and $I_t = 0.2$ nA.

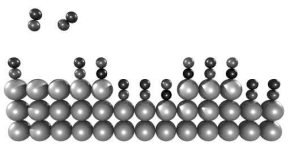

3.4 Results & Discussion

3.4.1 STM images

In this section, STM images taken by the ReactorSTM Mark I in different NO/CO partial pressure ratios, at elevated temperatures, are presented. Figures 3.2 and 3.3 show STM images obtained at 382 K and 395 K, in combination with the gas compositions to which the surface was exposed. The numbers in the partial-pressure graphs refer to the corresponding STM images. Image A, in figure 3.2, is an overview of the surface when it has been exposed to an NO-rich environment at 382 K, a few minutes after having been in a CO-rich mixture. The switch to the high partial pressure of NO has resulted in a high density of vacancy islands on the originally flat surface. The vacancy islands have a depth corresponding to the monatomic step height of platinum, 2.0 Å [112, 119]. Images B, C, & D are three consecutive images, zoomed in on the area indicated by the black square in image A. They demonstrate the high surface mobility; the vacancy islands disappear, and the wavy terrace edges straighten. Image E has been zoomed out again, and shows that the surface recovery has also taken place on a larger scale. Image A, in figure 3.3, is the flat surface in an NO-rich environment at 395 K. Image B was recorded during the switch to a CO-rich environment. As can be recognized in images B and C, the surface roughened, under these conditions, by the introduction of adatom islands, and waviness in the terrace edges. Minutes later, the roughness was observed to decay, as can be seen in images D and E.

The changes in the STM images can be interpreted in terms of a surface phase transition between NO-rich and CO-rich conditions. We propose that the surface is reconstructed into the quasi-hexagonal termination, when exposed to the NO-rich mixture, whereas the surface reconstruction is lifted to the (1x1) periodicity, when the mixture is switched to CO-rich. There are four pieces of evidence in support of this interpretation. Firstly, the structure observed under NO-rich conditions differs from a surface oxide. The height differences in the images all occur as steps, with the regular monatomic step height of metallic platinum, as shown in images A and B, and the height profiles D_1 to D_3, in part I of figure 3.4. For comparison, in image C, we also show an image of the same surface, with an oxygen-induced surface oxide. This was observed in a separate experiment, where we saw that oxidation makes the surface much rougher, and the height variations are not quantized in units of the metallic step height. Secondly, the quasi-hex surface termination is more dense than the (1x1) lattice, implying that reconstructing the

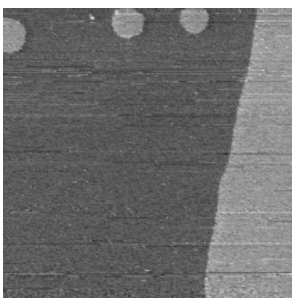

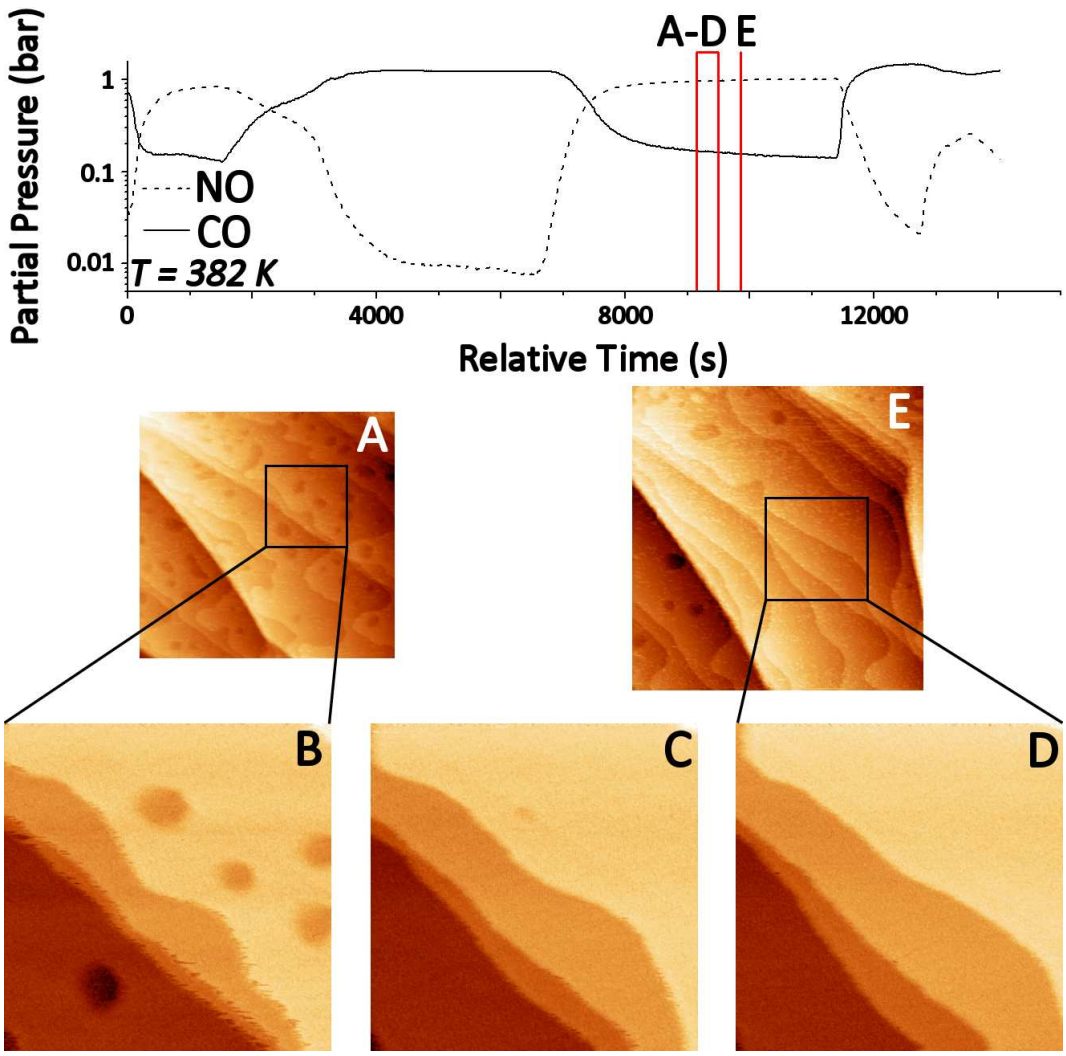

Figure 3.2: The gas compositions and STM images of Pt(100), in a flowing mixture of NO/CO, at a total pressure of 1.25 bar at 382 K; V_{bias} = 0.08 V; I_{tunnel} = 0.2 nA. A: 310 x 300 nm^2; B to D: 120 nm^2; E: 350 x 370 nm^2.

surface, starting from the unreconstructed surface, should yield vacancy islands. This is what has indeed been observed systematically, for example in figure 3.2. Similarly, de-reconstructing the surface, from quasi-hex to (1x1), should yield adatom islands, again in accordance with repeated STM observations. In both cases, after the phase transition occurred, we observed that surface diffusion slowly reduced the roughness. This shows that the observed roughness does not reflect the equilibrium structure, neither under NO-rich nor CO-rich conditions; rather, it should be regarded as a temporary, i.e.

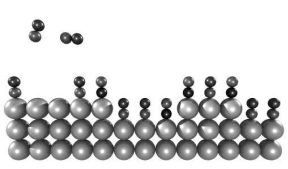

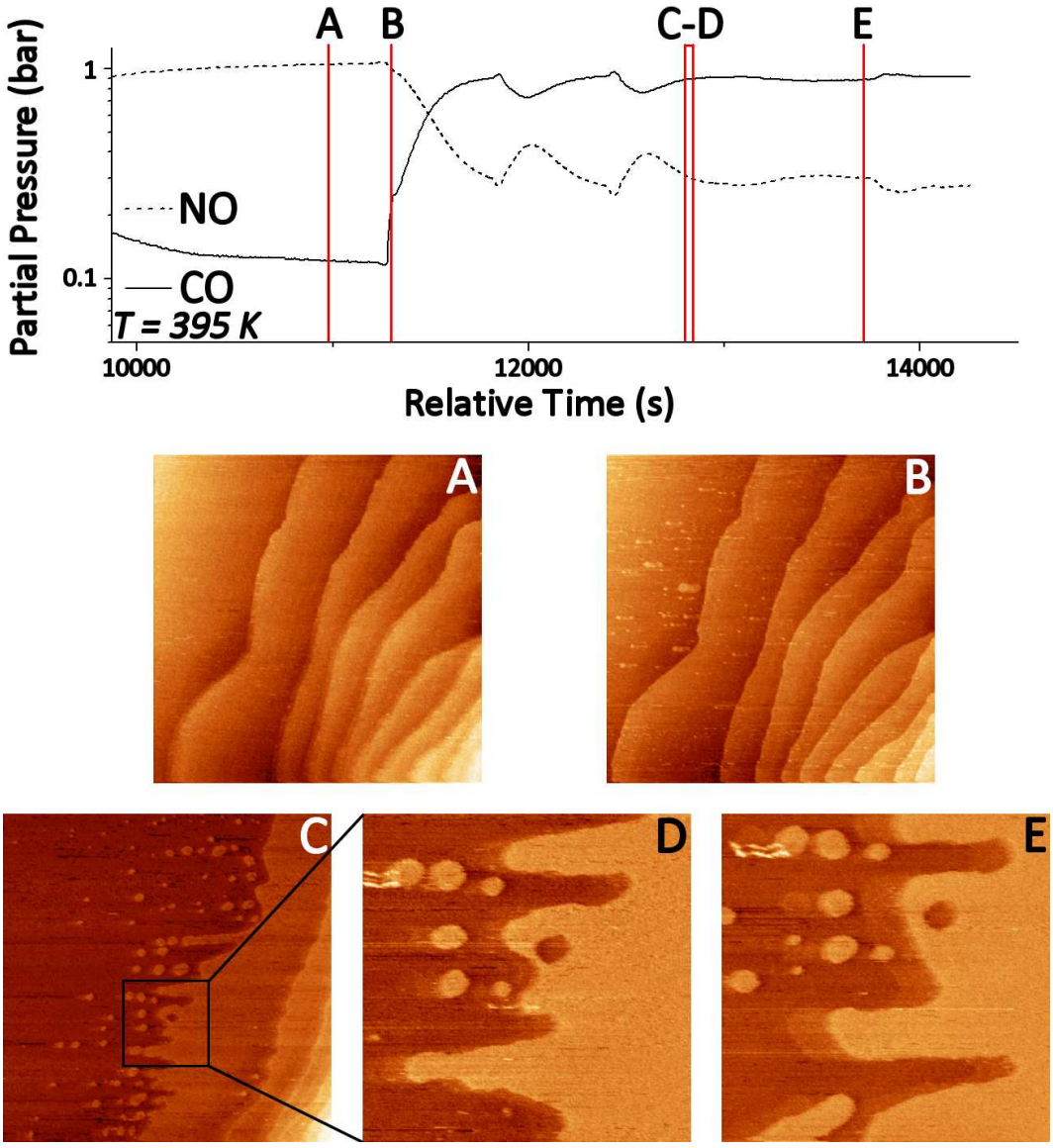

Figure 3.3: The gas compositions and STM images of Pt(100), in a flowing mixture of NO/CO, at a total pressure of 1.25 bar at 395 K; V_{bias} = 0.08 V; I_{tunnel} = 0.2 nA. A, B, C: 400 nm^2; D, E: 120 nm^2.

non-equilibrium structure, necessary to accommodate a surface density mismatch of the Pt atoms between the two structures. Thirdly, we observed that the surface temporarily responded significantly to its interaction with the STM tip, when the gas composition switched from NO-rich to CO-rich. This is demonstrated in part II of figure 3.4. Image E shows the Pt(100)

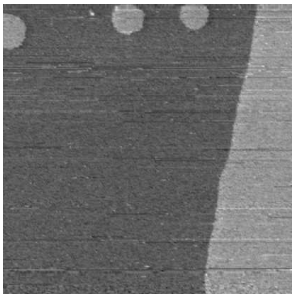

surface, just after the switch to a CO-rich mixture. As discussed before, the switch in gas composition leads to the formation of adatom islands. In the consecutive images, such as image F of figure 3.4, the tip is observed to drag material over the surface, which is evidenced by the alignment of the adatom islands and the terrace roughness along the scanning direction of the STM tip (this is the horizontal direction in all images). We believe this to be the consequence of the presence of a high density of mobile adatoms and small adatom islands, generated by the quasi-hex to (1x1) transition. This situation is temporary – after a few minutes, the surface no longer responds to the tip, while the adatom structures and the step roughness slowly decay, as can be seen in the lower part of figure 3.2. The final piece of evidence for the quasi-hex to (1x1) transition is the observation, in part III of figure 3.4, that the adatom and vacancy islands exhibit a weak hexagonal symmetry in NO-rich atmospheres, as shown in images G and H, whereas the vacancy islands, observed under CO-rich conditions, exhibit a weak square symmetry, as shown in image I. Our proposal of Pt(100) reconstructing in an NO-rich environment is at variance with earlier research on this reaction system, in which NO is lifting the reconstruction rather than stabilizing it [97, 119]. This difference is attributed to the fact that the surface was exposed to a high (ambient) pressure of NO, instead of a more traditional, low pressure of e.g. 10^{-6} mbar. In other words, this difference should be regarded as a *pressure gap* effect.

Since the surface density of the quasi-hex lattice is 20% higher than that of the (1x1) substrate lattice of Pt(100), we should expect the area of vacancy or adatom islands, created upon switching gas composition, to be 20% of the total area. Although our STM images are certainly consistent with this, the quality of many of our images is not sufficiently good to quantify the relative adatom or vacancy island coverage accurately. Another complicating factor is the role of the steps, which can easily accommodate adatoms or vacancies, and can therefore locally reduce their numbers. Furthermore, as observed in our images, surface diffusion was efficient in quickly removing the height variations, which made only the very first images, immediately after the switching, have the full adatom or vacancy island density. Unfortunately, the characteristic moiré pattern of the hex-reconstructed Pt(100) surface [121], which we observe under room temperature and vacuum conditions, could not be resolved in NO-rich atmospheres, probably due to the NO-induced loss of image resolution.

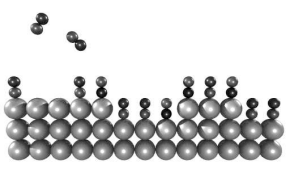

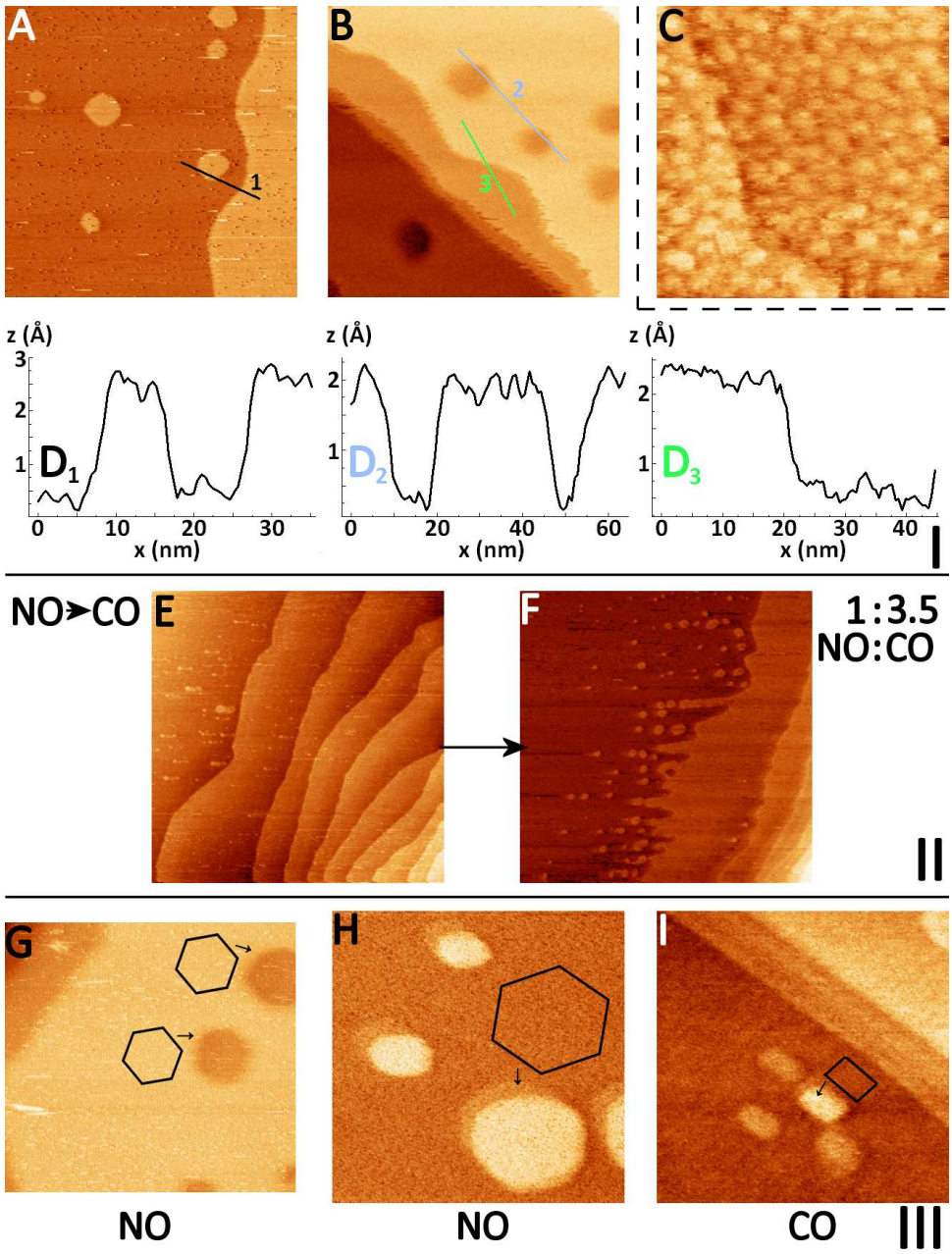

Figure 3.4: Part I: Images A and B were taken in an NO-rich flow. The lines labelled 1,2, and 3 refer to the three height profiles in D_1 to D_3, each showing height differences corresponding to the step height of Pt(100). For comparison, image C shows the roughness on this surface when it is oxidized in an O_2-rich flow. Part II: Two images illustrating the high surface mobility induced by the STM tip immediately after switching from an NO-rich to a CO-rich gas composition. Part III: STM images indicating weak hexagonal and square symmetries of vacancy and adatom islands in NO-rich and CO-rich environments, respectively.

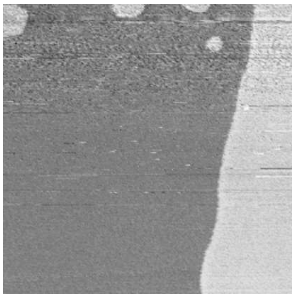

3.4.2 Interpretation of QMS signals

Since CO and N_2 have the same molecular mass, 28 amu, the mass spectrometer cannot distinguish between the two directly. In order to obtain the partial pressure of the N_2 that was produced in the reaction, we combined the convoluted signal S_{28}, at mass 28, with the signal S_{12} for atomic carbon (^{12}C), which is directly proportional to the partial pressure of CO.

$$p_{N_2} = c \cdot [S_{28} \; - \; n \cdot S_{12} \; - \; m \cdot S_{30}]. \tag{3.4.1}$$

Here, c is a calibration factor, relating the QMS signals to actual pressures. The factor n is a normalization constant, which corrects for the sensitivity ratio between the signals, at masses 28 and 12, to the partial pressure of CO. This factor was determined to be $n = 1.23$, from measurements under CO-rich conditions, when the formation rate of N_2 was negligible. Equation 3.4.1 also contains a term to correct for the contamination of the NO gas, used in the experiment, by a trace amount of $m = 5 \cdot 10^{-4}$ of N_2. This contribution scales with the signal S_{30} of NO.

3.4.3 Kinetics

In this section, the reaction kinetics, as measured with the QMS during the acquisition of the STM images, will be scrutinized. As concluded in the previous section, the surface exhibits either a hexagonal or a square structure, depending on the ratio between the partial pressures of NO and CO. These structures are thought to be two different terminations of the metal crystal, each with its own configuration of adsorbed species. Since the surface contains no special, reacted materials, such as a platinum oxide layer, we do not expect special reaction mechanisms, such as the Mars-van-Krevelen mechanism [27]. It has been assumed that the reactions simply proceed according to LH-kinetics, under both NO-rich and CO-rich conditions. In this section, therefore, the equations derived in section 3.2 for the formation rates of N_2 and CO_2 have been used, in an attempt to fit the measured partial pressures for both cases. It must be emphasized that the quasi-hexagonal structure and the square (1x1) structure differ significantly, both in atomic density and in geometry and symmetry. This should have an effect on the bonding geometries, and the corresponding binding energies, for the reactant and product molecules on the surface, and for reaction energy barriers. Such differences should be accompanied by differences in the kinetic parameters in the rate equations, for both situations. Before introducing separate values for the kinetic parameters for NO-rich and CO-rich conditions, we will first

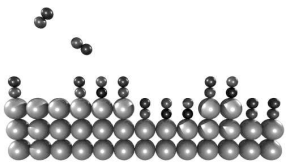

attempt to fit the measurements with a single set of parameter values.

In figure 3.5, the top graph shows the CO/NO compositions, to which the surface was exposed, and the production of N_2 and CO_2 measured at each stage. The signatures of LH-kinetics are clearly visible in the reaction rates. The reaction rates are low in both CO- and NO-rich atmospheres, and they maximize for intermediate mixtures.

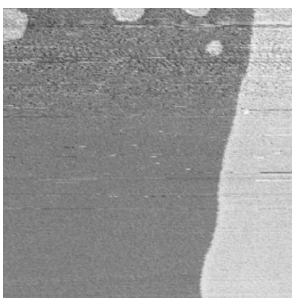

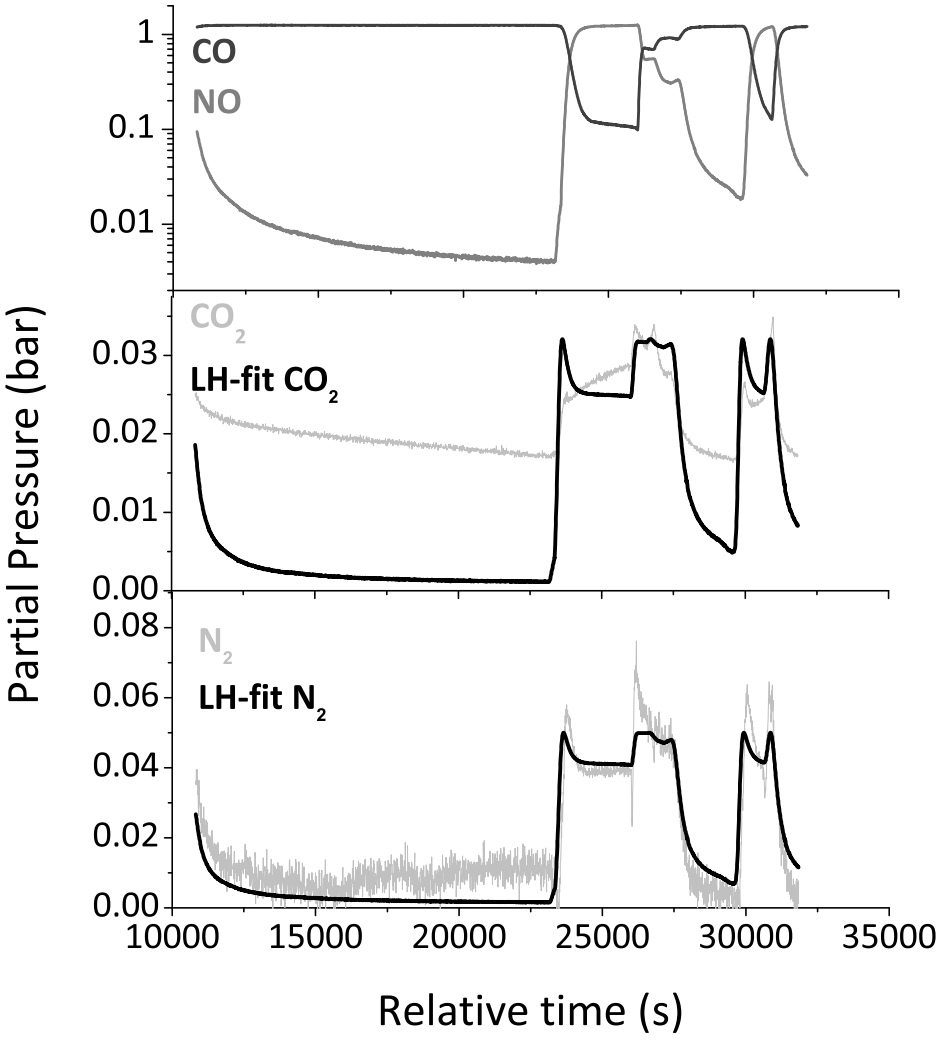

Figure 3.5: The reaction rates, (partial pressures), for N_2 and CO_2 production for the reactant gas mixtures, shown in the upper panel. The experimental partial pressures are indicated by the red curve, for CO_2, in the middle panel, and by the blue curve, for N_2, in the lower panel. The black curves in the lower two panels are the best-fit calculations, discussed in the text.

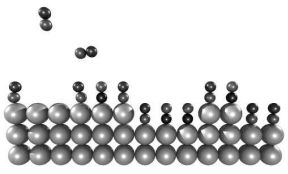

In section 3.2, it has been shown that the rate constants for the individual reaction steps combine into three fitting parameters K_i (equation 3.2.4). Table 3.1 shows two sets of optimal values, which were determined for these parameters by a least squares fitting procedure [122], either to the N_2 data or to the CO_2 data in figure 3.5.

Table 3.1: The optimal values for the parameters K_i, obtained separately by fitting equation 3.2.4 and its analog for CO_2 to the measured rates of N_2 and CO_2 formation, in figure 3.5.

	$K_1^{N_2,CO_2}\left[\frac{cm^2}{bar\cdot s}\right]$	$K_2\left[\frac{1}{bar}\right]$	$K_3\left[\frac{1}{bar}\right]$
N_2	0.40 ± 0.07	0.01 ± 0.01	1.95 ± 0.15
CO_2	0.29 ± 0.02	0.01 ± 0.01	2.3 ± 0.2

Before discussing the fits in detail, the values of the fitting parameters will be briefly addressed. It is clear that K_2 and K_3 have the same optimal values, when fitting either N_2 or CO_2. This is in full accordance with our expectations from section 3.2. The ratio between the K_1 values for the CO_2 fit and the N_2 fit is 0.7. This is much lower than the value of 2, expected when the reaction would have been dominated completely by reaction pathway I, for which $R_{CO_2} = 2R_{N_2}$. We further note that K_2 is very low, indicating that CO has a relatively strong tendency to desorb, in this reaction system. By contrast, K_3, which compares the adsorption and desorption rate constants of NO, is in the order of unity.

The LH-curves, in the middle and lower panels of figure 3.5, provide reasonable fits to the measured signals. The typical LH features, such as the reaction peaks when the mixture is changing from CO-rich to NO-rich and vice versa, and also the variations of the reaction rates during more modest changes in the composition of the reactant mixture, are all reproduced, at least qualitatively, by the fits. The fit to the CO_2 signal is not as good as that for the N_2 signal. As concluded above, from the ratio between the K_1 values, N_2 production is not fully dominated by the first pathway, implying that also N_2O has also been produced. Unfortunately, the mass of N_2O, 44 amu, is equal to that of CO_2, so that their peaks in the mass spectrum add up. It should be further noted that the extreme sharpness of the peaks, in the measured N_2 signal, is not represented by the fit. This discrepancy might be explained in two ways; firstly, the mass sweep of the QMS introduced systematic small differences between the precise readout times of the individual

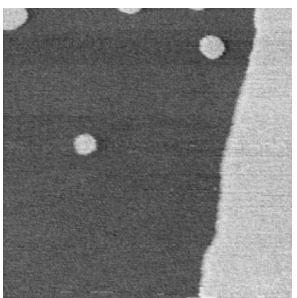

mass signals. When rapid changes occur in the partial pressures of the gasses involved in the reaction system, this may lead to a noticeable, transient error, when different signals are subtracted from each other, following equation 3.4.1. Secondly, as we will discuss now, the description of the reaction rates, in terms of a single set of kinetic parameters, may be inadequate, in view of the occurrence of two distinct surface structures.

In section 3.4.1, it was argued that the sudden introduction or sudden lifting of the quasi-hexagonal surface reconstruction of Pt(100) has been the cause of the surface roughness and the change in symmetry (hexagonal versus square), which were introduced by changing from NO-rich to CO-rich gas mixtures, and vice versa. Accompanying the difference between the two surface structures, we should also expect a difference in the kinetics of the NO reduction reaction. In the fits, in figure 3.5, this has been completely ignored. The fact that the calculations, in this figure, nevertheless qualitatively fit the observations, indicates that the reaction mechanism does not change. Thus the reaction rates should be described by Langmuir-Hinshelwood kinetics for both structures, and the values for the rate constants should be quite similar. The comparison between calculated and measured reaction rates will now be refined, by separating the measurements into two different regimes, one corresponding to the data for which the STM observations indicate the surface to be reconstructed, and the other corresponding to the unreconstructed surface. The STM images show that the two regimes correspond approximately to $p_{NO} > p_{CO}$ and $p_{NO} < p_{CO}$, respectively. For each of these two regimes, a separate set of values for the three parameters for the LH-kinetics was determined.

$$R_{N_2} = \begin{cases} K_1^{hex} \dfrac{p_{NO}}{\left(1 + K_2^{hex} p_{CO} + K_3^{hex} p_{NO}\right)^2} & p_{NO} > p_{CO} \\ K_1^{(1x1)} \dfrac{p_{NO}}{\left(1 + K_2^{(1x1)} p_{CO} + K_3^{(1x1)} p_{NO}\right)^2} & p_{NO} < p_{CO}, \end{cases} \tag{3.4.2}$$

where parameters K_i^{hex} define the fit for the reconstructed surface, and $K_i^{(1x1)}$ that for the unreconstructed surface. The result of this procedure is shown in the lower panel of figure 3.6; for comparison, the upper panel repeats the best fit to the N_2 signal for the 'single-kinetics' model, which was already shown in figure 3.5. The introduction of the three additional parameters has clearly led to a modest improvement of the fit. In particular,

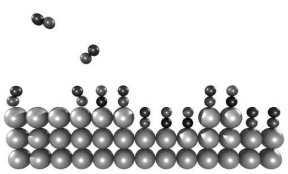

the CO-rich episodes are better described, even though the match between calculation and measurement is still not ideal.

The best-fit values for the six parameters of the 'dual-kinetics' model are listed in table 3.2, together with the three values for the 'single-kinetics' fit.

Table 3.2: The optimal values of the fitting parameters for the N_2 reaction rate for the 'single-kinetics' fit (figure 3.5), and for the 'dual-kinetics' fit (figure 3.6). The units of the parameters are the same as in table 3.1. The right column shows the goodness of fit, expressed as the normalized χ^2_ν, defined in equation 3.4.2.

Single kinetics	$K_1^{N_2}$	K_2	K_3	χ^2_ν
	0.40 ± 0.07	0.01 ± 0.01	1.95 ± 0.15	8.9
Dual kinetics	K_1^{hex}	K_2^{hex}	K_3^{hex}	χ^2_ν
hex	0.43 ± 0.05	0.01 ± 0.01	2.10 ± 0.20	
				9.1
	$K_1^{(1x1)}$	$K_2^{(1x1)}$	$K_3^{(1x1)}$	
(1x1)	0.33 ± 0.03	0.01 ± 0.01	1.60 ± 0.10	

In order to compare the quality of the fits on a more quantitative basis, the normalized χ^2_ν [123] for both fits has been determined.

$$\chi^2_\nu = \frac{1}{N-\nu-1} \sum_{i=0}^{N} \frac{(F_i - D_i)^2}{F_i}, \tag{3.4.3}$$

in which N is the number of data points, ν the number of fitting parameters (either 3 or 6), and F_i, and D_i are the theoretical and measured values of the reaction rate at point i. As the right column of table 3.2 shows, the difference between the goodness-of-fit values for the two models is statistically insignificant, mainly due to the remaining, systematic discrepancy between the measured N_2 production rates and both models. In principle, a similar, dual-kinetics fitting procedure can be carried out for the CO_2 signal, but the quality of the fit to this signal has been relatively poor. Possibly, a full fitting procedure, involving all 16 reaction rate constants, could lead to a fit with a χ^2_ν value closer to unity.

From figure 3.6 and table 3.2, the following information has been extracted. The dual-kinetics fit for the quasi-hexagonal episodes, in NO-rich

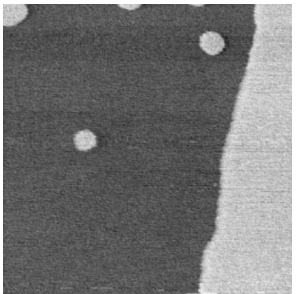

mixtures, is very close to the single-kinetics fit, which is also reflected in rather similar values of the three fitting parameters for the quasi-hexagonal structure, and for the single-kinetics model. On the other hand, as already indicated, the fit for the square (1x1) episodes, under CO-rich conditions, is clearly different from, i.e. better than, the single-kinetics fit. Indeed, two of the three parameters assume somewhat different values in this case. The biggest difference can be found in K_3, the ratio between the rate constants for adsorption and desorption of NO, which is always high, but tends more strongly towards NO adsorption in the quasi-hexagonal phase than in the square phase. K_1 is somewhat lower in the square phase than in the quasi-hexagonal phase, which means that, either the NO dissociation step is more difficult, or the N_2O production is higher, in this phase.

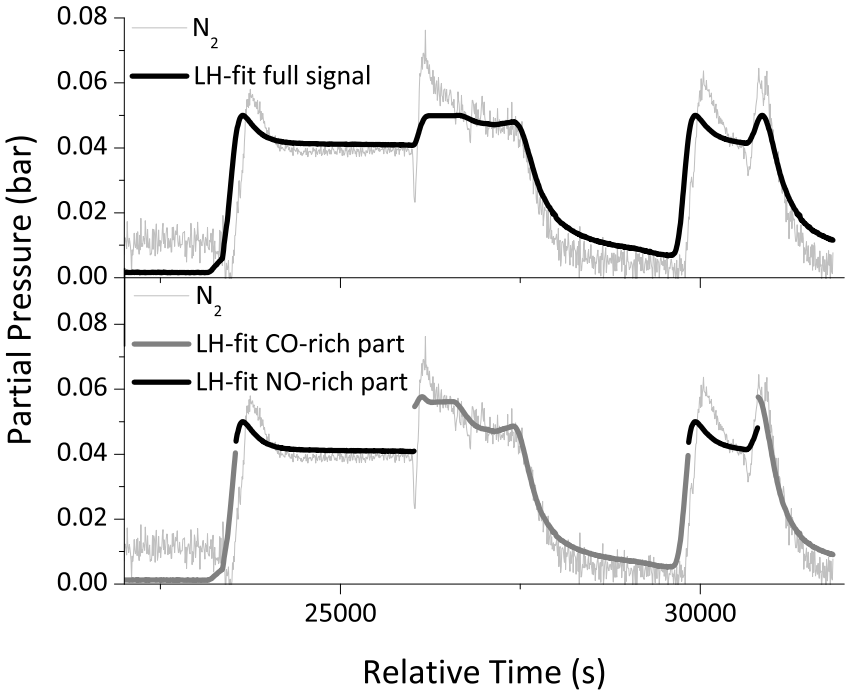

Figure 3.6: (Lower panel) The fit obtained according to the dual-kinetics Langmuir-Hinshelwood model for the production of N_2, compared with the experimental N_2 signal. (Upper panel) For reference, the upper panel repeats the single-kinetics fit of figure 3.5.

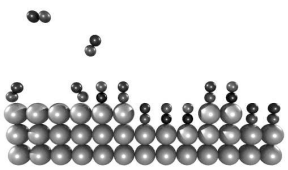

3.5 Conclusions

In this chapter, the reduction of NO by CO on the Pt(100) surface, by in-situ STM, at atmospheric pressures and elevated temperatures, combined with simultaneous mass spectrometry has been investigated. The STM images indicate that, depending on the CO:NO ratio, the surface switches between two different structures, with either a square or a hexagonal symmetry, reflecting the unreconstructed (1x1) surface and the quasi-hexagonally reconstructed Pt(100) surface, respectively. The measured rates of N_2 and CO_2 production in terms of Langmuir-Hinshelwood kinetics has been analyzed. In this procedure, the possibility of two separate LH regimes, namely one for the (1x1) surface, and the other for the quasi-hexagonal structure have been considered. Even though the latter, dual-kinetics, fit follows the measurements more closely, the systematic differences between measurements and models are too severe to quantify this improvement.

Appendix: LH calculation

In this appendix, the derivation of R_{CO_2} and R_{N_2} is shown, using the assumptions, as listed in section 3.2. Let us start with rewriting the reaction equations with corresponding reaction constants k_i:

$$
\begin{array}{lll}
CO_{(g)} + * & \rightleftharpoons_{k_{-1}}^{k_1} & CO_{(ads)} \quad (1),\\
NO_{(g)} + * & \rightleftharpoons_{k_{-2}}^{k_2} & NO_{(ads)} \quad (2),\\
NO_{(ads)} + * & \rightleftharpoons_{k_{-3}}^{k_3} & N_{(ads)} + O_{(ads)} \quad (3),\\
N_{(ads)} & \rightleftharpoons_{k_{-4}}^{k_4} & \frac{1}{2}N_{2\ (g)} + * \quad (4),\\
CO_{(ads)} + O_{(ads)} & \rightleftharpoons_{k_{-5}}^{k_5} & CO_{2\ (g)} + 2* \quad (5),\\
NO_{(ads)} + N_{(ads)} & \rightleftharpoons_{k_{-6}}^{k_6} & N_2O_{(ads)} + * \quad (6),\\
N_2O_{(ads)} & \rightleftharpoons_{k_{-7}}^{k_7} & N_{2\ (g)} + O_{(ads)} \quad (7),\\
N_2O_{(ads)} & \rightleftharpoons_{k_{-8}}^{k_8} & N_2O_{(g)} + * \quad (8).
\end{array}
$$

In the steady state approximation, we can directly define the reaction rate for the formation of CO_2 and N_2 from the equilibrium coverage ϑ_i, of the species on the surface.

$$\frac{d\vartheta_{CO_2}}{dt} \equiv R_{CO_2} = k_5\vartheta_{CO}\vartheta_O. \tag{3.5.1}$$

$$\frac{d\vartheta_{N_2}}{dt} \equiv R_{N_2} = k_4\vartheta_N^2 + k_8\vartheta_{N_2O}. \tag{3.5.2}$$

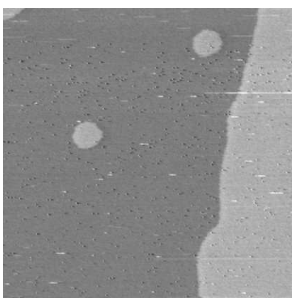

In order to be able to fit Langmuir-Hinshelwood kinetics to the data, obtained by the QMS, which comes in the form of partial pressures of reactants and reaction products, the expressions 3.5.1 and 3.5.2 need to be rewritten, as a function of the partial pressures of the reactants CO and NO. Let's start with the derivation of R_{CO_2}, which can be rewritten as a function of ϑ_{CO} and ϑ_{NO}, via the coverage of oxygen atoms on the surface, ϑ_O,

$$\frac{d\vartheta_O}{dt} = k_3\vartheta_{NO}(1-\vartheta_{NO}-\vartheta_{CO}) - k_5\vartheta_{CO}\vartheta_O = 0$$

$$\Leftrightarrow R_{CO_2} = k_3\vartheta_{NO}(1-\vartheta_{CO}-\vartheta_{NO}). \tag{3.5.3}$$

ϑ_{CO} and ϑ_{NO} now need to be written as functions of the reactant pressures p_CO and p_NO. We will start by writing down the steady state situation, from the reaction equations,

$$\frac{d\vartheta_{CO}}{dt} = k_1 p_{CO}(1-\vartheta_{CO}-\vartheta_{NO}) - k_{-1}\vartheta_{CO} = 0$$

$$\frac{d\vartheta_{NO}}{dt} = k_2 p_{NO}(1-\vartheta_{CO}-\vartheta_{NO}) - k_{-2}\vartheta_{NO} = 0.$$

These can be substituted into each other to obtain functions of the coverages, solely as a function of the reactant pressures, after which the result can then be substituted into equation 3.5.3, to obtain the reaction rate for the formation of CO_2:

$$\vartheta_{CO} = \frac{\frac{k_1}{k_{-1}}p_{CO}}{1+\frac{k_1}{k_{-1}}p_{CO}+\frac{k_2}{k_{-2}}p_{NO}} \tag{3.5.4}$$

$$\vartheta_{NO} = \frac{\frac{k_2}{k_{-2}}p_{NO}}{1+\frac{k_1}{k_{-1}}p_{CO}+\frac{k_2}{k_{-2}}p_{NO}} \tag{3.5.5}$$

$$\Rightarrow R_{CO_2} = k_3\frac{\frac{k_2}{k_{-2}}\cdot p_{NO}}{\left(1+\frac{k_1}{k_{-1}}\cdot p_{CO}+\frac{k_2}{k_{-2}}\cdot p_{NO}\right)^2}. \tag{3.5.6}$$

The derivation, to obtain the expression for the reaction rate for N_2 formation, is slightly more complicated. Again, the coverages of the various species, on the surface on which the N_2 reaction rate depends, should be rewritten, by reactant pressures. Looking at equation 3.5.1, the steady state situations for ϑ_N and ϑ_{N_2O} first need to be written down, which yields

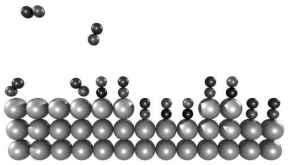

$$\frac{d\vartheta_N}{dt} = -2k_4\vartheta_N^2 - k_6\vartheta_{NO}\vartheta_N + k_3\vartheta_{NO}(1-\vartheta_{CO}-\vartheta_{NO}) = 0$$

$$\frac{d\vartheta_{N_2O}}{dt} = k_6\vartheta_{NO}\vartheta_N - k_7\vartheta_{N_2O} - k_8\vartheta_{N_2O} \qquad = 0.$$

From this, the expressions for ϑ_N and ϑ_{N_2O} can be derived, in which the quadratic formula has been used to obtain the expression for ϑ_N,

$$\vartheta_N = -\frac{1}{4k_4}\left(k_6\vartheta_{NO} \pm \sqrt{k_6^2\vartheta_{NO}^2 + 8k_4k_3\vartheta_{NO}(1-\vartheta_{CO}-\vartheta_{NO})}\right)$$

$$\vartheta_{N_2O} = \frac{k_6\vartheta_{N_2O}\vartheta_N}{k_7+k_8}.$$

Since $\vartheta_N > 0$, the square root term has to be larger than $k_6\vartheta_{NO}$, which means that only the minus solution is valid. Substituting these expressions in equation 3.5.2, and simplifying the outcome, yields

$$\begin{aligned} R_{N_2} = \quad & \frac{-k_7/(k_7+k_8) \;+\; 1/2}{4k_4}\left[k_6^2\vartheta_{NO}^2\right. \\ & -\;\; \left. k_6\vartheta_{NO}\sqrt{k_6^2\vartheta_{NO}^2 + 8k_4k_3\vartheta_{NO}(1-\vartheta_{CO}-\vartheta_{NO})}\right] \\ & +\;\; 1/2\; k_3(1-\vartheta_{CO}-\vartheta_{NO}), \end{aligned}$$

which, after substituting expressions 3.5.4 and 3.5.5, and simplifying, yields equation 3.2.2:

$$\begin{aligned} R_{N_2} = \quad & \frac{k_2 p_{NO}}{4k_{-2}k_4\left(1+\frac{k_1}{k_{-1}}p_{CO}+\frac{k_2}{k_{-2}}p_{NO}\right)^2} \\ & \times \;\; \left[\left(\frac{1}{2}-\frac{k_8}{k_7+k_8}\right)k_6^2\frac{k_2}{k_{-2}}p_{NO}\right. \\ & -\;\; \left.\left(\frac{1}{2}-\frac{k_8}{k_7+k_8}\right)k_6\sqrt{1+\frac{8k_4k_3k_{-2}}{k_6^2k_2p_{NO}}}\;\right] \\ & +\;\; \frac{k_3k_2p_{NO}}{2k_{-2}\left(1-\frac{k_1}{k_{-1}}p_{CO}+\frac{k_2}{k_{-1}}p_{NO}\right)^2}. \end{aligned}$$

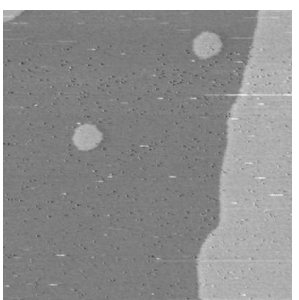

If k_4 is dominant,

$$\lim_{k_4 \to \infty} R_{N_2} = \frac{k_3}{2} \frac{k_2}{k_{-2}} \frac{p_{NO}}{\left(1 + \frac{k_1}{k_{-1}} p_{CO} + \frac{k_2}{k_{-2}} p_{NO}\right)^2},$$

is obtained, and if k_4 is negligible,

$$\lim_{k_4 \to 0} R_{N_2} = \frac{k_3 k_8}{k_7 + k_8} \frac{k_2}{k_{-2}} \frac{p_{NO}}{\left(1 + \frac{k_1}{k_{-1}} p_{CO} + \frac{k_2}{k_{-2}} p_{NO}\right)^2},$$

is obtained, in which $(\sqrt{1+\epsilon})$ is approached by $(1 + 1/2\epsilon)$. The combination of the two limits is exactly equation 3.2.3.

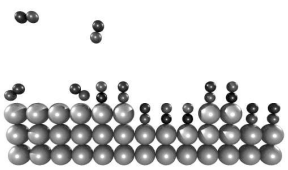

Chapter 4

High-resolution STM imaging: CO oxidation on Pt(110)

4.1 The reaction system: Expectation

The oxidation of CO on transition metal based catalysts has instigated extensive studies [76–82, 124, 125]. These include high-pressure STM studies [124] and high-pressure SXRD studies [125], on several surface orientations of palladium and platinum, one of which is Pt(110). As argued in chapter 2, CO oxidation on Pt(110) has been used primarily as a test reaction for the ReactorSTM Mark II, to determine its performance, with respect to the ReactorSTM Mark I. In addition, this experiment has yielded a few results, unveiling more of the strengths of the ReactorSTM Mark II, in addition to "just" atomic row resolution STM images, in the (1x2) missing-row reconstruction on Pt(110), at room temperature and low vacuum conditions, and atomic row resolution on Pt(110) under a flow of 1 bar of CO at 160℃.

In the aforementioned studies, the reaction system, as modelled in figure 4.1, is proposed to hold for CO oxidation on Pt(110). Figure 4.1 is divided into four phases, which are distinguished by the ratios between the partial pressures of CO and O_2. We start from a clean Pt(110) surface, exhibiting its (1x2) missing-row reconstruction (fig. 4.1 A), as has been observed in STM imaging [128]. After exposure to CO, following arrow 1 in figure 4.1, the reconstruction is lifted, and the surface restructures into its (1x1) phase. Due to the half-occupation of the outermost layer, resulting from the 1x2 to 1x1 transition, initially a pattern of (1x1) patches, which have the Pt(110) monatomic step height of 1.4 Å, with respect to the layer below, is formed on the surface. This resembles the pattern of the skin of a tiger, hence the

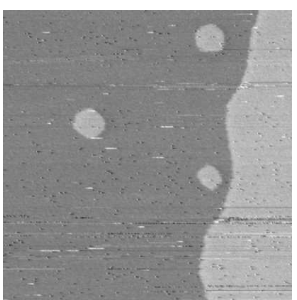

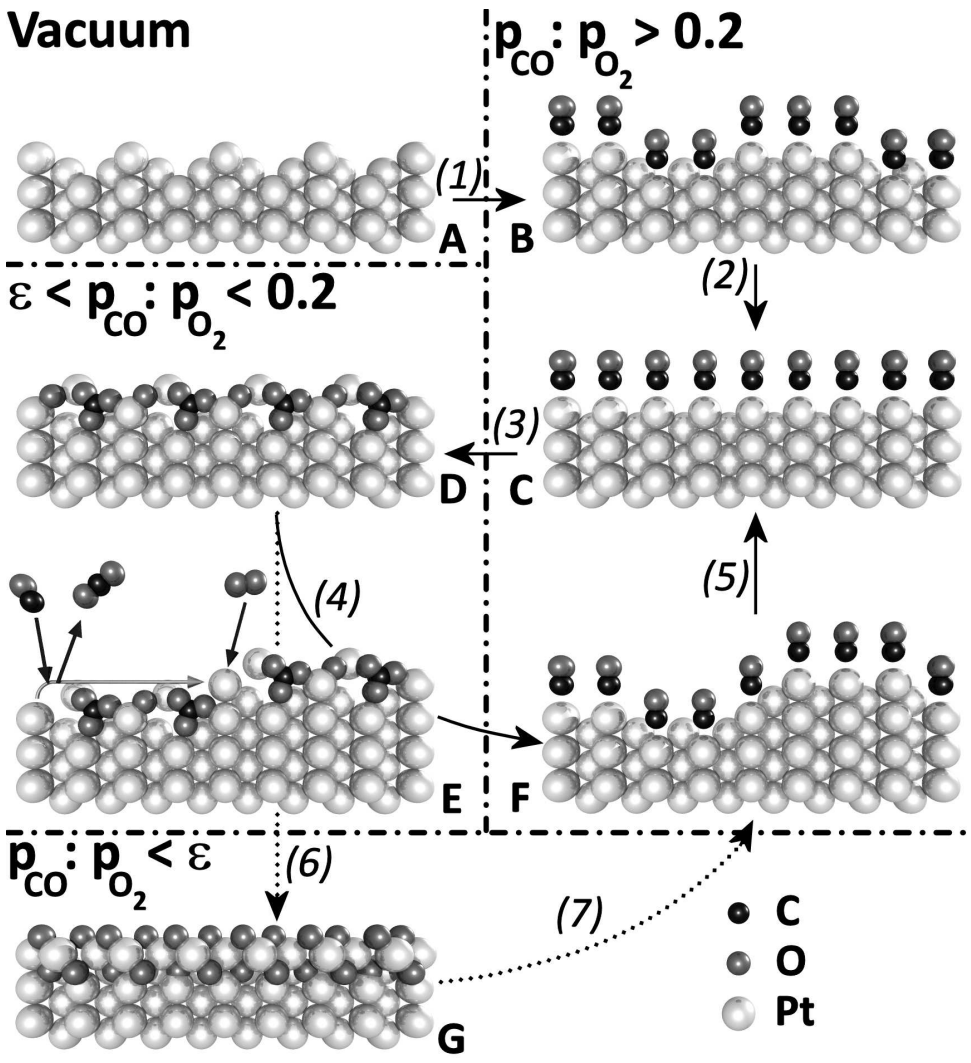

Figure 4.1: A model for the CO-oxidation reaction system on Pt(110). There are four phases distinguished by certain $p_{CO} : p_{O_2}$ values. (A) (1x2) missing-row reconstruction under vacuum. (B) The tiger skin pattern after CO-exposure of (A). (C) The flat, CO-covered metallic surface. (D) (1x2) commensurate oxide structure, including carbonate ions. (E) The Mars-Van Krevelen mechanism in action. (F) The rough CO-covered metallic surface. (G) α-PtO_2.

"tiger skin" pattern, which is observed in STM images [124, 127] (4.1 B). In time (arrow 2), surface diffusion leads to a flat, CO-covered metallic surface (4.1 C), which is the equilibrium situation in a CO-rich phase. This results in STM images showing large terraces, which have the Pt(110) monatomic step

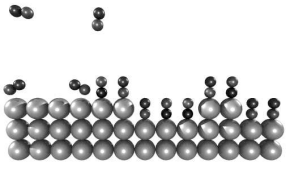

height. When $p_{CO} : p_{O_2}$ is changed to roughly < 0.2 (arrow 3), the surface undergoes a phase transition into a (1x2) commensurate oxide structure (4.1 D). Although this structure has never been atomically resolved in real space, the (1x2) period has been observed in reciprocal space by SXRD [125]. Since no known platinum oxide terminates in this (1x2) commensurate shape on the surface, and the (1x2) missing-row reconstruction is excluded by the fact that the rows of the new structure are shifted in the (001) direction, it has been suggested by DFT calculations that carbonate ions are involved in this structure. This, in turn, explains why this structure *only* occurs when there are significant traces of CO present in the gas atmosphere. The carbonate ions might act as an intermediate in the CO_2 formation. Large scale STM images have indicated that the surface, in this case, becomes progressively rougher with respect to the metallic phase; patches, with a height of 2 to 4 Å and a width of 4 to 7 nm, cover the surface [124]. Since the height of these patches did not correspond with (an integer of) the monatomic step height on Pt(110), they were ascribed to an oxide. The roughening of the surface is ascribed to the active reaction mechanism in this phase, the Mars-Van Krevelen mechanism, which is shown in 4.1 E. A CO molecule reacts with an oxygen atom on the oxide surface to form CO_2, which desorbs, creating an under-coordinated platinum atom on the surface. A certain fraction of these under-coordinated platinum atoms becomes highly mobile, diffusing on the oxide surface, until they get oxidized, and immobilized in the oxygen-rich gas atmosphere. The (1x2) structure, however, was not observed in the earlier mentioned STM images. On the one hand, from the situation in 4.1 D, the CO pressure can be increased again (arrow 4), switching the surface back to the CO-covered metallic state, which initially will be a rough metallic surface (4.1 F). The roughness, induced by the formation of the oxide layer, will anneal out by diffusion (arrow 5), returning the surface to its equilibrium situation, the flat, metallic surface, as in 4.1 C; this process has been observed by STM [124]. On the other hand, when the pressure ratio $CO:O_2$ drops below ϵ (arrow 6), the (1x2) commensurate oxide is replaced by the incommensurate hexagonal α-PtO_2 oxide (4.1 G), which has been observed in SXRD [125]. Also, due to the Mars-Van Krevelen reaction mechanism, this oxide will slowly roughen. When this (roughened) oxide is again exposed to CO (arrow 7), the surface switches back to the rough CO-covered metallic state (4.1 F), following the same steps as described above.

If there is a clear energy difference between the adsorption of CO onto steps with respect to the terraces, the surface can spontaneously switch from an oxide to a metal at a particular $CO:O_2$ ratio. At the same $CO:O_2$ ratio, a flat metallic surface will oxidize. In the model described in figure 4.1,

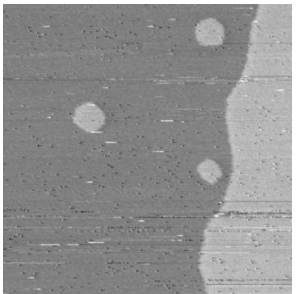

we have shown that the surface roughens in the oxidic state, by the Mars-Van Krevelen reaction mechanism, and smoothes by diffusion in the metallic state. All these ingredients can lead to spontaneous reaction oscillation at the mentioned $CO:O_2$ ratio, which is the case for many of the surface orientations of palladium and platinum. A model for this type of reaction oscillation, linking the evolution of roughness in the oxidic and metallic states, and the affinity of CO binding at steps, is discussed in depth in [28]. In the case of Pt(110), however, reaction oscillation has never been observed. A reason for this might be the existence of the intermediate (1x2) commensurate oxide structure (4.1 D), which does not exist for the other surfaces, destroying the regime in which spontaneous reaction oscillations for the other surface orientations exists.

4.2 The reaction system: Mark II experiments

4.2.1 STM images and reaction kinetics

The results obtained with the ReactorSTM Mark II are summarized in figures 4.2, 4.3, and 4.4. Figure 4.2 shows a series of STM images, with different length scales in various gas compositions, whereas figure 4.3 shows the same phase diagram as figure 4.1, in which the ball models have been replaced by STM images at a fixed length scale of 4.5 nm^2. This way of presenting the STM images has been chosen deliberately. In figure 4.2, the large scale images, representing the various reactor conditions, show important surface properties, such as atomic density and mobility. In addition, the high quality of the z-scale in these particular images allows us to determine the atom-row distance quantitatively, by the use of height profiles, which are also shown in figure 4.2. In the phase diagram, figure 4.3, the length scale of the STM images has been kept constant, which in some of the phases leads to lower quality STM images, with respect to their analogous images shown in figure 4.2. Keeping the length scale constant, however, provides a very clear picture of the atomic level changes which occur when switching from one phase to another. Figure 4.4 shows the reaction kinetics, as measured by the quadrupole mass spectrometer during this experiment.

Figure 4.2 A shows an STM image of the Pt(110) surface, at room temperature in an ill defined vacuum[1]. This image resolves the (1x2) missing-row

[1] As I explained in chapter 2, the reactor volume is separated from the ultrahigh vacuum environment during STM operation, implying that the pressure will slowly increase after the reactor is closed. This means that, prior to exposing the sample to high gas pressures,

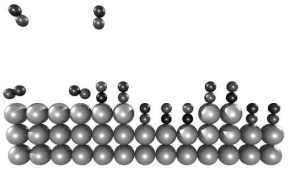

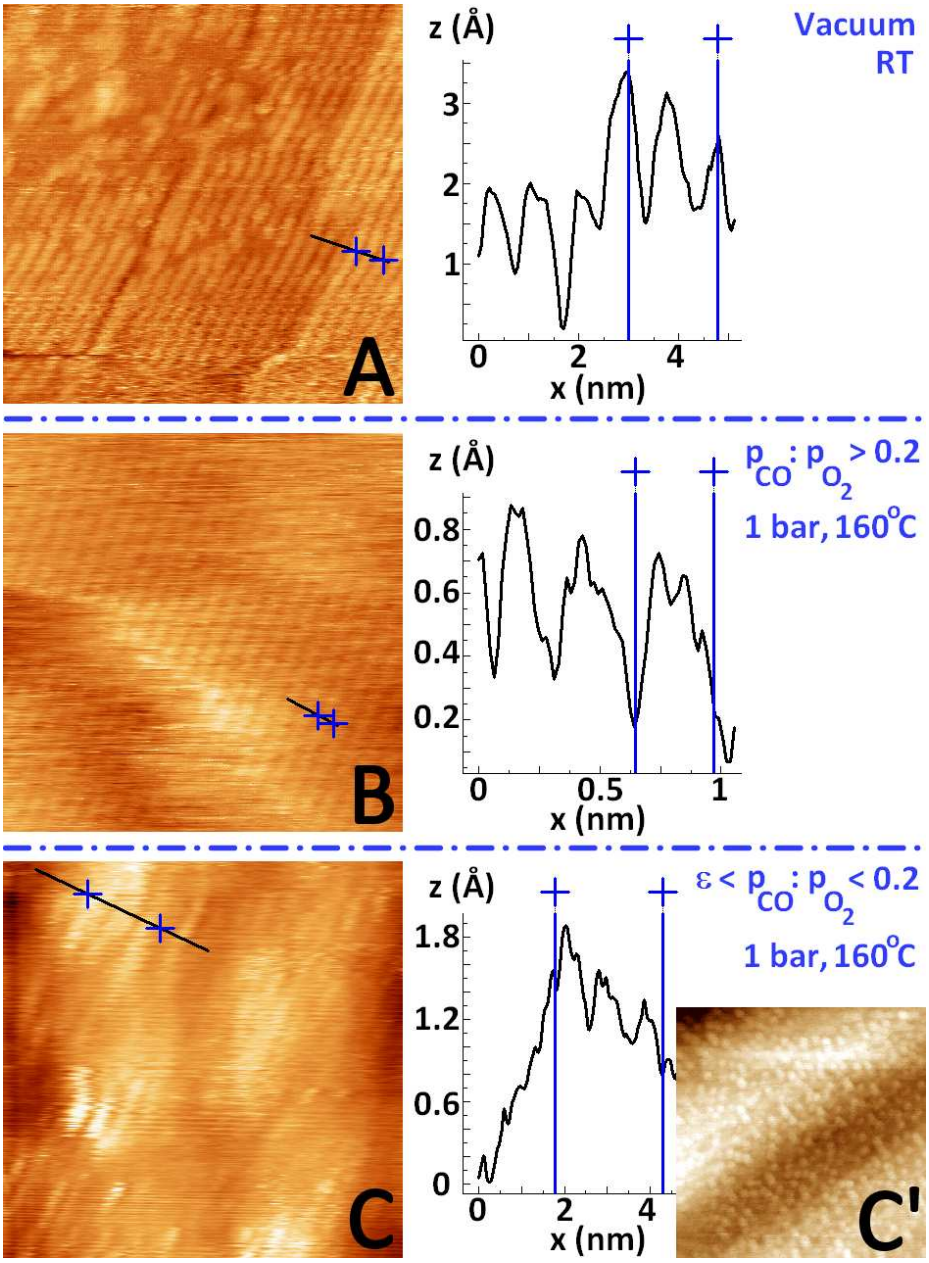

Figure 4.2: STM images and corresponding height profiles in three different phases. (A) A 25 nm x 25 nm STM image of the missing-row reconstruction, at room temperature under vacuum. (B) A 7.5 nm x 7.5 nm STM image of Pt(110), at 160℃ and 1 bar of CO. (C) A 12.5 nm x 12.5 nm STM image of Pt(110), at 160℃ and 1 bar of O_2/CO. (C') A 210 nm x 210 nm STM image of Hendriksen et al. [27], under the same conditions.

the freshly prepared sample will be exposed to the reactor's "bad breath", which will always contain remnants of the gases used in the last experiment, typically influencing the surface structure.

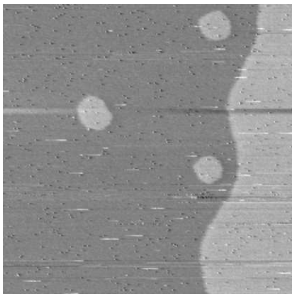

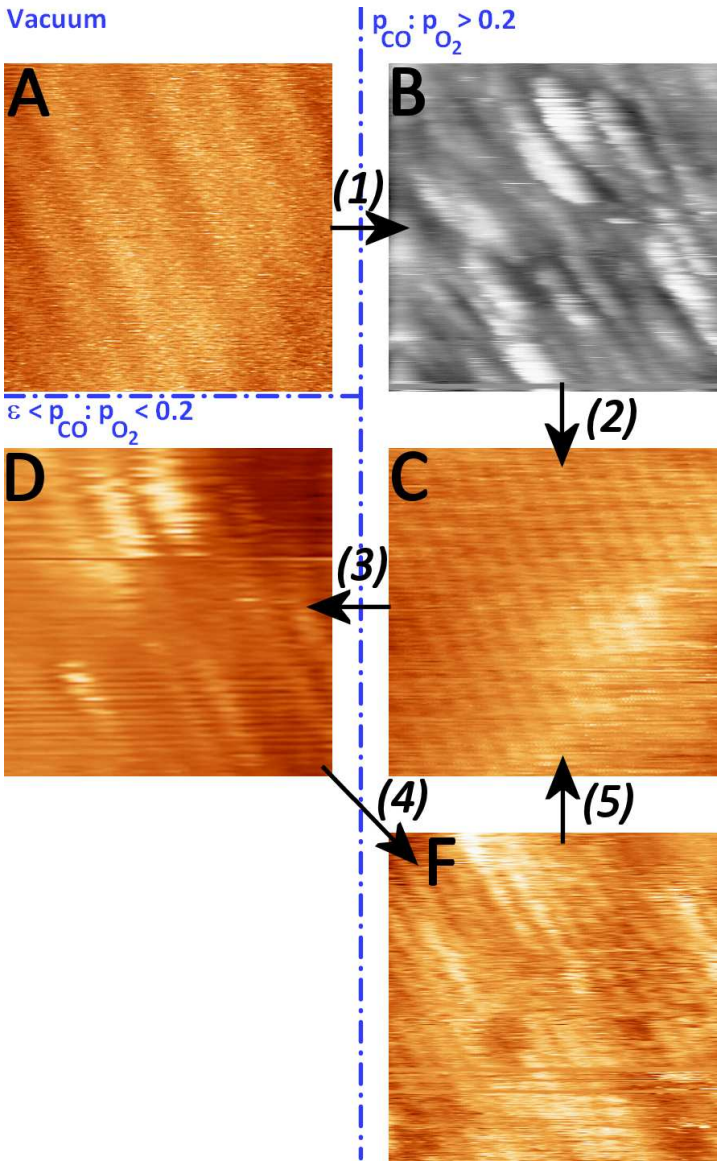

Figure 4.3: A phase diagram, as in figure 4.1, with STM images as obtained with the ReactorSTM Mark II. Unless otherwise stated, $T = 160℃$. All images are 4.5 nm x 4.5 nm, except for the grey scale image (15 nm x 15 nm). (A) The missing-row reconstruction, under vacuum at room temperature. (B) The tiger skin pattern, after exposure of (A) to 1 bar CO. (C) Flat, metallic Pt(110), in a CO-rich flow. (D) Roughened Pt(110), exhibiting the (1x2) commensurate surface oxide, at a high O_2/CO ratio. (F) Rough, metallic Pt(110) in CO-rich flow.

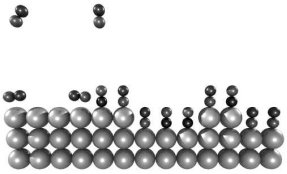

reconstruction, which Pt(110) exhibits in vacuum, after applying standard sample preparation techniques (1 keV Ar^+ ion bombardment, followed by annealing at ∼1000 K). By using height profiles, such as the one corresponding to image A, the average inter-row distance has been measured to be 0.75 ± 0.03 nm. This is consistent with the theoretical value of 0.78 nm [89]. In the upper left hand corner of image A, however, the periodicity conforming with the surface reconstruction is broken: larger clumps of material have accumulated in adatom islands. A reason for this restructuring process is the fact that the ill defined vacuum, to which the sample is exposed in this stage, contains gases, which induce lifting of the reconstruction (see footnote). Finally, from the top right hand to one-third left of the bottom right hand, runs a step with a height of 1.5 Å, corresponding to the monatomic step height on Pt(110) of 1.4 Å [129]. Image B, in figure 4.2, shows an atomic-row resolved STM image of Pt(110), exposed to 1 bar of CO at a temperature of 160℃. In this case, the average row distance is 0.37 ± 0.02 nm, corresponding to the theoretical distance between the rows of the normal (110) surface termination of metallic platinum [90]. This surface is not rigid: in the bottom half of the image, a number of horizontal stripes occur coinciding with the scan direction of the STM. These stripes are not caused by noise or tip effects, but by step dynamics – they cover a step on the surface. The mobility of single atoms at a step, namely, is much higher than the line scan speed of the STM, meaning that every time the STM tip scans over the edge of the step, a different number of atoms will be present at that step, at that particular moment. This will lead to a stripy step, which is what we observe[2]. Finally, image 4.2 C shows an STM image of Pt(110), exposed to 1 bar of a CO/O_2 mixture, with a ratio $\epsilon < p_{CO} : p_{O_2} < 0.2$ at 160 ℃. It can immediately be seen that the roughness on the surface has increased, in the form of the formation of protrusions. Hendriksen et al. [27] have already shown this structural change on the surface by high-pressure STM (image C'), but they could not resolve the atomic details of this structure. By the use of spectroscopic techniques, however, they could determine that the structure on the protrusions was the same as the structure in between the protrusions. Moreover, they ascertained that this structure is not consistent with a metallic state of platinum. As they found, the height of these protrusions, ∼0.2 nm, was not in agreement with the monatomic step height on Pt(110). They also determined the sizes of the protrusions to be between 6 and 8 nm. As I mentioned in the former section, Ackermann et al. [36] have studied this system by high-pressure SXRD, also observing this structure in reciprocal space. Their observation revealed a commensurate structure with a (1x2) period, which they, in combination

[2]Similar work has been done on Au(111) [130, 131]

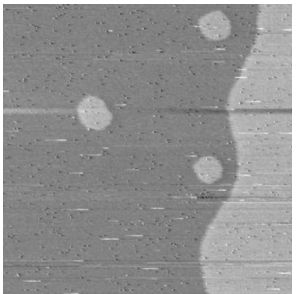

with density functional theory calculations, determined to be a surface oxide, incorporating carbonate ions. Physical proof for these indirect observations, using the ReactorSTM Mark II, has been provided. A commensurate super structure, with an average periodicity of 0.72 ± 0.06 nm has been observed, which indeed agrees with a (1x2) period. Furthermore, this period has been observed both on the protrusions (of which four are visible in image C), and in between the protrusions, supporting both Hendriksen's and Ackermann's results.

The phase diagram, shown in figure 4.3, shows the full cycle of the Pt(110) surface during an experiment. It has been built up in the same way as figure 4.1, labelling the STM images and arrows between the phases, in figure 4.3, with the same letters and numbers as the ball models and arrows in figure 4.1. The length scales of the STM images are now all 4.5 nm^2, except for the grey scale image, which shows the tiger skin structure at a larger scale. Starting from the vacuum situation in image A, showing the (1x2) missing-row reconstruction, we expose the surface to a high pressure of CO and 160℃(arrow 1). Via image B, showing the tiger skin pattern at larger scale (15 nm^2), we obtain image C (arrow 2): a flat metallic surface, clearly exhibiting double the density of rows, with respect to image A – the reconstruction is lifted. The reaction mechanism, on this type of surface, follows Langmuir-Hinshelwood kinetics [27, 79]. Following arrow 3 into the oxygen rich phase (image D), with $p_{CO} > \epsilon$, the surface roughens, due to the different reaction mechanism in this regime, the Mars-Van Krevelen mechanism [27, 124], as explained in the former section. As can be seen, image D exhibits the (1x2) period, consistent with the existence of the (1x2) commensurate oxide structure. When switching back to a large CO:O_2 ratio, the surface switches back to its metallic phase (arrow 4), as can be seen in image F, in which the number of rows on the surface has doubled with respect to image D. The reaction mechanism now also changes back to the Langmuir-Hinshelwood mechanism, and due to the high mobility of platinum atoms at this temperature, the surface anneals out, ending up in the same situation as image C: a flat metallic surface (arrow 5). The cycle following arrows 3-4-5 can be repeatedly reproduced. During these measurements, the transition to the incommensurate hexagonal α-PtO_2 oxide structure was not observed, nor the roughening process following this transition, because the CO pressure never dropped below ϵ.

Finally, figure 4.4 shows the CO-oxidation reaction kinetics obtained by the mass spectrometer. Graph A includes several switches from an O_2-rich to CO-rich environment. The signals, measured by the QMS for oxygen and CO, are slightly different in magnitude; the acquired oxygen signal is lower

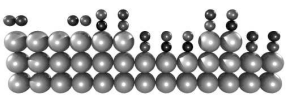

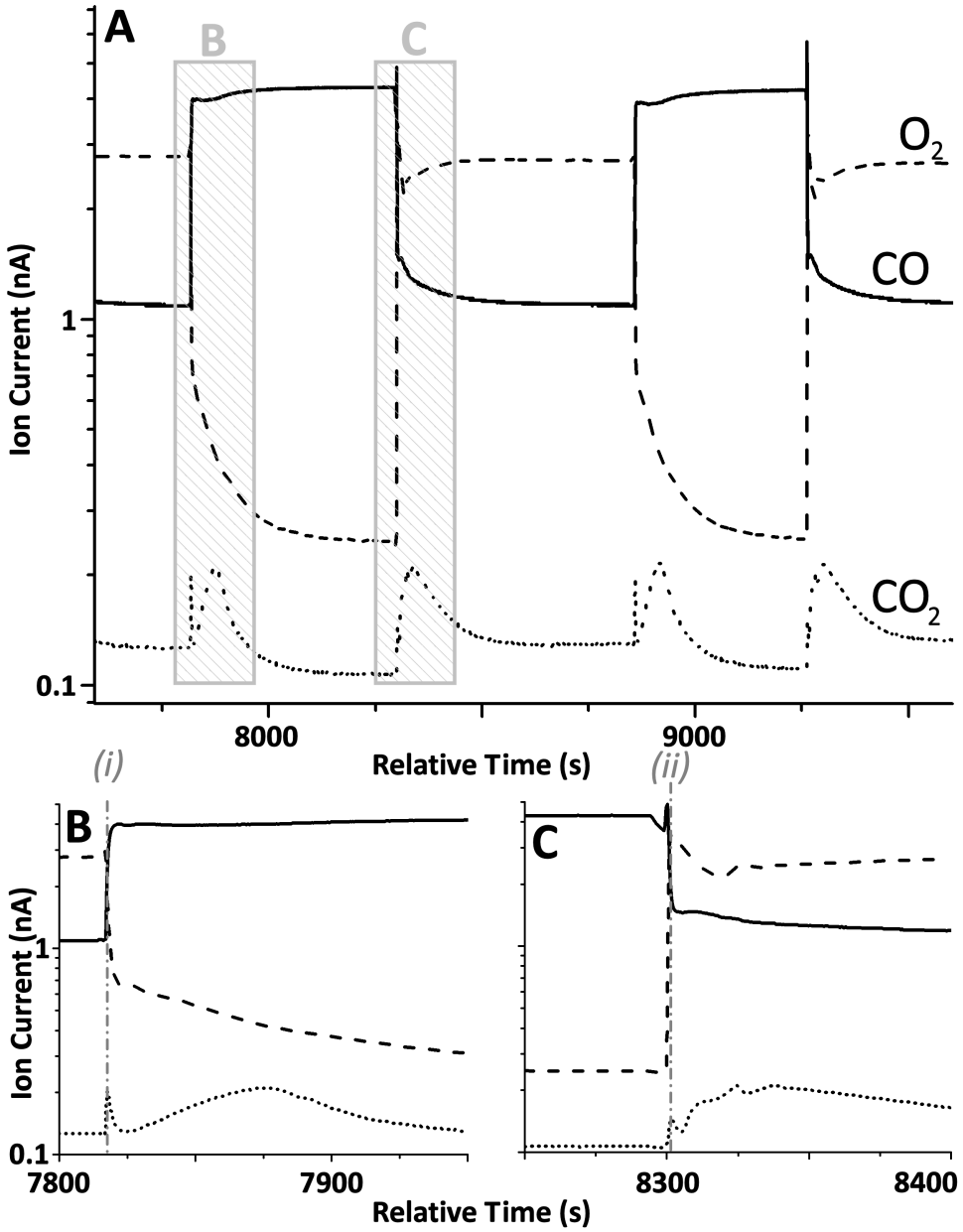

Figure 4.4: The reaction kinetics. Graph (B) and (C) are two zoom-ins of graph A, labelled by the grey rectangles.

than CO signal, for the same pressure/flow settings. This is to be expected, since the turbo pump evacuates oxygen more effectively than CO. The CO_2 signal shows some interesting features. Firstly, the steady state reaction rate, in the CO-rich environment, is lower than in the oxygen-rich environment.

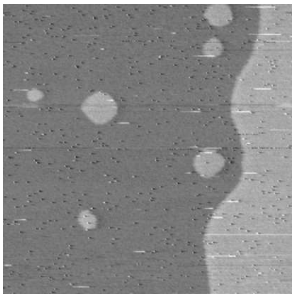

This indicates that the CO-covered metallic Pt(110) surface is less reactive than the oxidic surface, under these circumstances. Switching from oxygen-rich to CO rich, a sharp peak in the CO_2 production can be seen, as at t = 7820 s, and t = 8810 s; a zoom-in on this feature can be seen in graph B. The sharp increase might correspond to the increasing reactivity of the oxide, when offering more CO to the surface, after which the surface switches back to the metal, which, since it has a lower reactivity, causes a step down in reaction rate. The broader peaks, following these sharp peaks, are the Langmuir-Hinshelwood peaks, peaking at the optimal CO/O_2 ratio for that particular environment. On the other hand, when switching from CO to O_2, the oxidation of the surface happens on the decreasing slope of the Langmuir-Hinshelwood peak at t = 8310 s(graph C), after which the surface maintains a higher reactivity, directly proportional to the CO partial pressure. In the STM images, obtained under oxygen-rich flow conditions, the (1x2) period was always visible, indicating that the partial CO pressure, as can be seen in spectrum A of figure 4.4, under these conditions, was always sufficiently high to maintain this structure. Changing the flow reactor to a batch reactor might lead to consumption of all the available CO, during which the surface might change to its bulk α-PtO_2 phase. Deteriorating tip quality, however, prevented us from observing this transition. The next section will briefly focus on the tip quality, showing an example of the surface switching from the commensurate oxide to a metal.

4.2.2 Transition

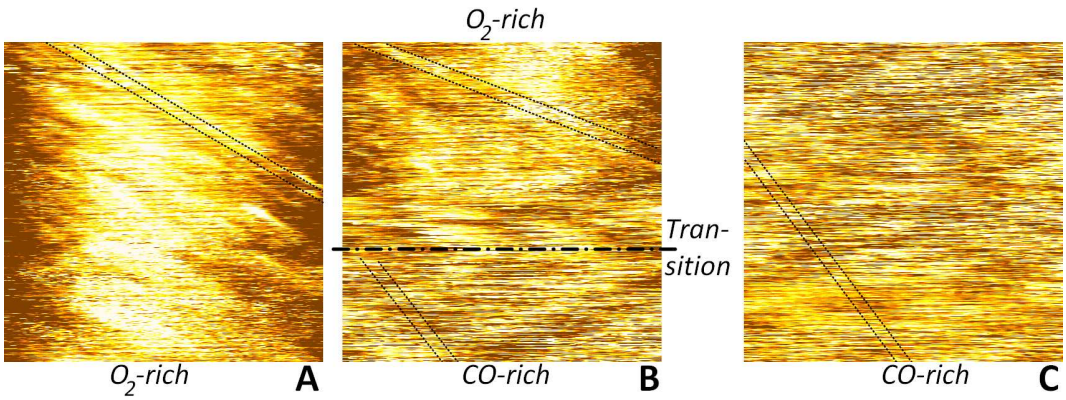

Figure 4.5: 25 nm x 25 nm STM images, showing a transition from the oxidic to the metallic terminated surface. (A) shows the oxide, (B) the transition, and (C) the metal.

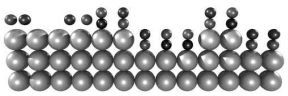

As mentioned in the last paragraph, the quality of the tip can deteriorate quickly under extreme conditions. As an example, a series of consecutive STM images is shown in figure 4.5, in which a transition from the (1x2) commensurate surface oxide to the metallic phase has been recorded. Image A shows the oxide, in which the black lines indicate the direction of the atomic rows. Image C shows the metal, in which the black lines also assist in distinguishing the barely visible atomic rows. In image B, the transition takes place at roughly two-third from the top of the image. The transition occurs at the same time that we observe a step down in reaction rate, for instance at $t = 7820$ s in figure 4.4. The reactivity of the surface oxide, under the offered high oxygen pressure conditions, is higher than the metal under similar, but high CO pressure, conditions. This step down in reaction rate also causes a small change in the thermal drift; since fewer (exothermic) reactions occur at the surface, the temperature will decrease slightly.

As can already be seen in image A, the image quality on the oxide is visibly worse than the images shown in figures 4.2 and 4.3. During the transition, visibility was completely lost, and the first images in the CO-rich environment are hardly any better. There are several reasons for this behavior. Firstly, the tip used is a mechanically sheared PtIr (80% Pt, 20% Ir) tip. In an oxidizing environment, this tip will also oxidize, which negatively influences the image quality. Moreover, the tip will also act as a catalyst for the reaction. As can be seen in image B in figure 4.2, the platinum surface exhibits a huge mobility, which will not be different on the tip. Atoms can migrate through the tip apex, leading to the horizontal stripiness in the images, due to the slow z-feedback response of the electronics, with respect to the speed at which atoms migrate through the tip apex. These horizontal stripes were observed in all our STM images, at least up to a certain level. During the switching of the gas environments, the more stoichiometric CO/O_2 ratio will lead to a changing catalytic activity of the tip, which leads to surface dynamics, making it incapable of imaging. This can clearly be seen in image B of figure 4.5, where all the details on the surface were completely lost. The tip surface possibly could also be roughened by the Mars-van Krevelen mechanism, leading to an initially rough tip surface, after switching back to a CO-rich environment; the smoothing of this surface will also lead to noise, caused by atoms passing the apex, which we observe in image C.

So in order to observe more extreme situations, such as, in this particular experiment, a change from an oxidic phase to a metallic phase, or even from one oxidic phase to another, the quality of the tip needs to be improved. One can think of using etched PtIr (or W) tips, rather than mechanically sheared

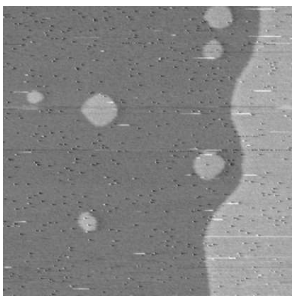

ones, and gold plating these sharp tips, to make them inert. One could even think of using tips made of pure gold, but gold is a very soft material to work with.

4.3 Conclusion and outlook

Observations on the reaction system of CO oxidation on Pt(110), making use of the ReactorSTM Mark II, support the work previously done by Hendriksen et al. and Ackermann et al. [27, 36]. The atomic row structure on the surface could be resolved in a series of gas environments, which have been divided into phases, as in figure 4.1 and 4.3, shedding light on the different surface terminations in these different phases. More directly, the (1x2) commensurate surface oxide structure, proposed by density functional theory calculations, has been imaged, and shows that this structure completely covers the surface. CO_2 reaction rates seem to be higher for the oxidized surface than for the metallic surface. All in all, as already pointed out in chapter 2, the ReactorSTM Mark II operates as intended; this experiment shows that it is capable of providing new insights into atomic-scale high-pressure, high-temperature catalysis, bringing many unexplored areas within striking distance.

For future STM experiments, it is necessary to improve the quality of the tip. The possibilities of gold plating tip and reactor compatible materials, to improve stability, are currently being explored. This step is also necessary to improve imaging in future experiments, including other strongly oxidizing or aggressive agents, such as NO and H_2S.

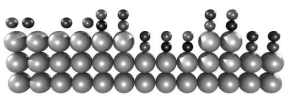

Chapter 5

Hydrodesulphurization of thiophene

5.1 Hydrotreating: industry and research

The refinement of crude oil is one of the cornerstones of modern society. In this chemical process, the crude oil is converted into transportation fuels, such as gasoline and diesel oil. An important step in oil refining is the catalytic hydrotreating of liquid petroleum fractions, which are obtained after distillation of the crude oil. During catalytic hydrotreating, the hetero-atoms N, S, and O are removed from the petroleum fractions. During the combustion of the carbohydrates containing these elements, SO_2 and NO_x are formed, which are the main contributors to the formation of acid rain. Furthermore, these types of carbohydrates have a detrimental effect on the transition-metal based catalysts used in the further refining processes and in car exhausts. In addition, hydrotreating converts olefins and aromatics into saturated carbohydrates, which burn more cleanly (i.e. fully to CO_2 and H_2O). The annual sale of hydrotreating catalysts is 10% of the total global catalyst market, which emphasizes the importance of hydrotreating. In short, the hydrotreating catalyst consists of CoMo, NiMo, and NiW sulfides, dispersed on a highly porous γ-alumina support. CoMoS is the catalyst for desulphurization and NiMoS for denitrogenation and hydrogenation, and in one of the processes, NiWS assists in hydrocracking [140, 141].

Throughout the years, the hydrotreating catalysts have drastically improved, which is undoubtedly partly thanks to a contribution of scientific research. The main drive for this drastic improvement was legislation in the European Union and the United States. Up to now, European legislation

decreed six emission standards, starting from the end of the eighties to setting maxima to the emission of CO, NO_x, unburnt hydrocarbons, and soot, to improve the air quality [132][1]. Additionally, to decrease the SO_2 emission, the maximum sulphur content for fuel was decreed to be at maximum 350 ppm (diesel)/ 150 ppm (gasoline) from the year 2000, to 50 ppm from 2005, and to <10 ppm ("sulphur free") from 2009 onward. Although these standards have already been met, hydrodesulphurization, the hydrotreating process in which sulphur is removed from hydrocarbons, is still gaining a lot of attention, for various reasons. Firstly, to meet this ultra low sulphur standard, *deep desulphurization* of liquid petroleum fractions is necessary. Crude oil contains a large variety of organosulphur compounds, including thiols (R-S), sulfides (R-S-R), and aromatic heterocycles called thiophenes [133]. Within the group of thiophenes, the larger molecules, such as, for instance, 4,6-dimethyldibenzothiophene ($C_{12}H_8S$), are the real challenge to desulphurize, because they exhibit steric hindrance with respect to the active sites of the catalyst [134, 135], decreasing their reactivity towards desulphurization, as is illustrated in figure 5.1. Deep desulphurization means to desulphurize these types of molecules. With an increasing demand for light fuels such as diesel, refineries have increased their production of these fuels by cracking increasingly heavy feedstocks, which contain more of these large thiophenes. In addition, oil fields at different geological locations differ in sulphur content, which can be up to 5% in weight[2]; new oil fields, to be exploited in the future, are foreseen to contain, on average, more sulphur. Secondly, the reaction mechanisms for all hydrotreating catalysts are believed to be quite similar, since their structure is more or less the same. Legal standards for NO_x emission are still being intensified, meaning that the hydrodenitrogenation catalyst is still under pressure for improvement. Understanding the hydrodesulphurization reaction also assists improvement of the hydrodenitrogenation catalyst. And the economics of the hydrodesulphurization

[1]Euro 6, which should be met in 2014, sets the following emission standards for diesel and gasoline passenger cars (in g/km). Light commercial vehicles have similar standards [132].

	CO	HC	HC+NO_x	NO_x	PM
Diesel	0.5	-	0.17	0.08	0.005
Gasoline	1.0	0.10	-	0.06	0.005

[2]Five examples of crude oil from different geological orientations, in combination with their sulphur content (low sulphur content is "sweet" oil; high sulphur content is "sour" oil) are [136–138]:

Oil type	S content
West Texas Intermediate	0.24%
Brent Blend	0.37%
Dubai Crude (Fateh)	2%
Tia Juana heavy	2.82%
Boscan	5.4%

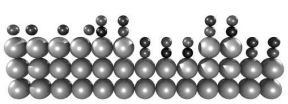

play a role in catalysis development. Currently, a typical plant heats a feedstock, mixed with a high amount of hydrogen (50-100 bar), to a temperature between 300℃ and 400℃, after which it is exposed to a fixed-bed reactor, containing highly dispersed catalytic nano-particles supported on γ-alumina. The exact combination of temperature and pressure depends on the sulphur content of the crude oil. Generally, the high temperature is needed to break the strong S-bonds, whereas the high hydrogen pressure is needed to prevent the catalyst from sulphur saturation. Hydrogen is expensive, and elevated temperatures cause the catalyst to age more quickly by coking and sintering – fundamental insights into the action of the catalyst might lead to lower operational temperatures and pressures [139–144].

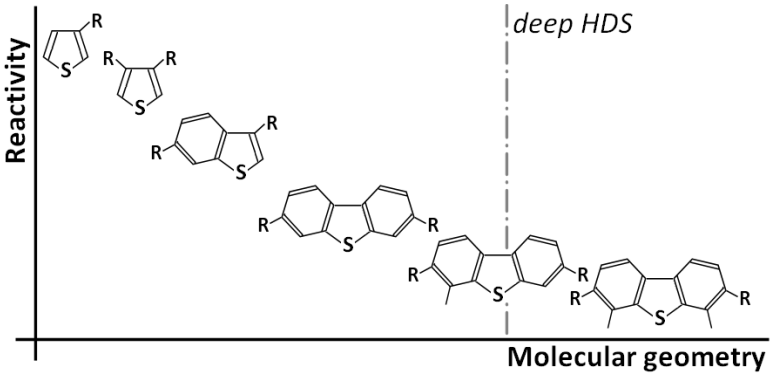

Figure 5.1: Various thiophene components which can be found in crude oil. The larger molecules are more difficult to desulphurize, because of steric hindrance [134, 135].

5.1.1 Catalyst structure and reactivity: Literature

The development of the high-quality catalyst used in today's desulphurization plants, molybdenum disulphide nano-crystallites, with cobalt as a promoter, was supported by extensive scientific research on this catalytic system. Direct and indirect insights into the structure and activity were gained by experimental studies, including gas chromatography [147], low energy electron diffraction (LEED) [148], Auger electron spectroscopy (AES) [148], STM [149–154], X-Ray crystallography [155], elastic scattering quantum chemistry, extended X-ray adsorption fine-structure spectroscopy (EXAFS) [156], and scanning electron microscopy; theoretical studies include electronic structure calculations [157–159, 164–166]. In these research efforts, both the non-promoted and the cobalt-promoted MoS_2 crystallites have been investigated.

Amongst the most important findings were the active sites of the catalyst: the edges, rims, and corners of the crystallites. In contrast, the basal planes exhibit no reactivity. Steps in the activated reaction cycle include the binding of reactants and reaction intermediates to the rims and sulphur vacancies in the edges; the formation of sulphur vacancies at the edges is favored, since the sulphur atoms are less strongly bound there, with respect to the ones in the basal plane. In addition, edge and rim positions provide a better accessibility to the large organosulphur compounds than the plane. Additional evidence for the activity of the edges and rims is an experimental study, which has shown a direct proportional relation between the amount of edge and rim sites on a sample containing MoS_2 nano-crystallites and its reactivity. The number of edge and rim sites can be decreased by sintering the crystallites into bigger particles. The promoters of the catalyst, cobalt, and nickel, are believed to replace molybdenum atoms at the edges of the crystallites, lowering the activation energy of, for example, the creation of a sulphur vacancy [173]. They also lower the activation energy for binding organosulphur molecules to the basal planes of the nano-particles, after which the additives assist diffusion of these molecules to the active sites [151]. The morphology of the MoS_2 crystallites, which determines the number of active sites, is an important issue, which depends on the reaction conditions. There have been many efforts to determine the composition, electronic structure, and morphology of MoS_2 nano-crystallites, in order to gain insight into the mechanisms behind the activity and selectivity of the catalyst. Extensive reviews on this subject exist in the literature [134, 140, 155, 171–174, 177]. This will be discussed in more detail below. The reaction mechanism has been investigated by studying hydrogen and thiophene interaction; thiophene desulphurises rather easily. Langmuir-Hinshelwood kinetics are accepted to be the mechanism for this reaction [155]. Apart from desulphurization, several hydrogenation steps take place on the surface of the catalyst; the various reaction pathways, in combination with the state of the edges under various conditions, have been studied extensively by DFT, and are supported by ex situ STM studies [145, 153, 175–177]. These will also be described in more detail in the paragraphs below.

Usually, unpromoted MoS_2 is used as a starting point for models of the hydrodesulphurization catalyst, since in situ EXAFS has shown that the catalysts used ordinarily consist of MoS_2 crystallites, with a size of 10 to 20 Å, after sulphidation at 300 to 400℃ [182]. Several STM studies have resolved these nano-particles atomically, providing valuable information about their morphology and edge terminations [142, 145, 153]. Figure 5.2 shows the basic structure of MoS_2. The crystallites consist of layered S-Mo-S slabs,

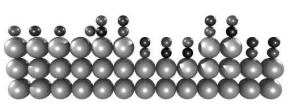

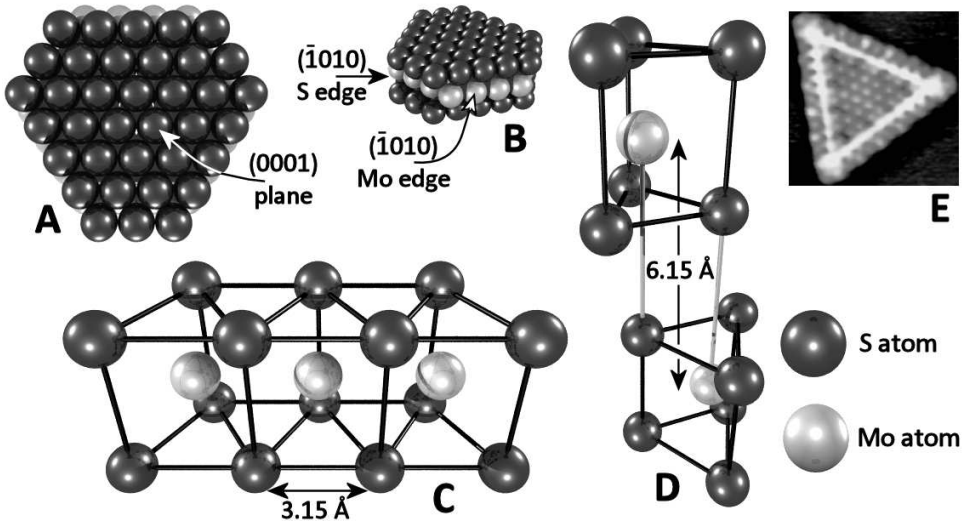

Figure 5.2: (A) A top view of a MoS_2 crystallite under reaction conditions; in this case the shape is a deformed hexagon [164, 178], rather than a triangle, as is the case under UHV or H_2S rich conditions [145]. The (0001) plane is indicated. (B) A 3D rendition of a MoS_2 crystallite, showing two possible edge terminations: a ($\bar{1}010$) S edge and a ($\bar{1}010$) Mo edge. (C) A side view of a single layer S-Mo-S slab; the atoms are hexagonally arranged. The interatomic distance is 3.15 Å[183]. (D) A unit cell of 2H-MoS_2. The Mo-Mo distance between the two layers is 6.15 Å[183]. (E) An STM image obtained by Helveg et al. [145] resolving a triangular MoS_2 crystallite on Au(111). A bright rim following the perimeter of the crystallite can be distinguished.

in which the atoms are arranged hexagonally in (0001) planes. In both the sulphur layers and the molybdenum layer, the interatomic distance is 3.15 Å. The molybdenum layer is trigonal-prismatically oriented with respect to the sulphur layers above and below, which span 3.16 Å, the thickness of a single MoS_2 slab. Multiple slabs are stacked in the same way as graphite, and are held together by Van der Waals interactions. Since this interaction is weak, one of the uses of MoS_2 is that of a lubricant. In molybdenite, the natural form of MoS_2, the second row is shifted by half, with respect to the first layer, creating a unit cell as depicted in figure 5.2 D. Here the distance between the two metal layers is 6.15 Å. STM images from earlier work have revealed a bright rim of high electron density, which follows the perimeter of the crystallites. This is attributed to the existence of localized electronic states on the edges. An example from the work of Helveg et al. [145] is shown in figure 5.2 E, illustrating this bright rim. Their studies concluded that the edge states are one-dimensional, localized perpendicular to the edges, but

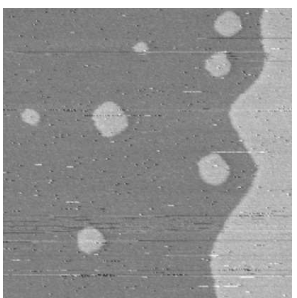

delocalized parallel to the edges [140, 143, 145, 171, 184, 185].

As can be seen in figure 5.2 B, there are two natural edge terminations: an $(\bar{1}010)$ S edge and an $(\bar{1}010)$ Mo edge. Initially, after preparing the MoS_2 crystallites under high sulphiding conditions ($p_{H_2S} \gg p_{H_2}$), previous STM studies in ultrahigh vacuum have shown that the crystallites exhibit a triangular structure, with the bright rim along the edges, as shown in figure 5.2 E. The triangular structure indicates that, under these conditions, one of the edges is favored above the other. By combining DFT studies with the STM results obtained, it was determined to be the $(\bar{1}010)$ Mo edge, in which the uncoordinated molybdenum atoms at the edges are decorated with sulphur dimers (fig. 5.3 C). Figure 5.3 B shows a different possible Mo edge termination, occurring under different environmental conditions: the 50% S covered Mo edge. Figure 5.3 A shows the bare Mo edge as reference. The bright rim is believed to correspond to metallic states occurring at the Mo edges of the crystallites, which in itself is a semiconductor [145, 153, 158–160]. The bright rim is believed to play a key role in the reaction mechanism, to be discussed below. The Mo edge is not, however, always the most stable configuration: there is a size effect [175]. An S:Mo ratio in the crystallites larger than approximately 3:1 seems to be energetically disfavored, leading to morphological transitions of the crystallites to lower the S:Mo ratio. This happens for small clusters, where the number of atoms along the edge $n \leq 6$, in which the sulphur excess relative to the bulk is relatively large with respect to Mo edges, which are decorated with sulphur dimers. The change in configuration for the smaller particles translates into triangular crystallites, exhibiting the $(\bar{1}010)$ S edges instead of the Mo edges. For even smaller clusters, the S edges undergo a transition from fully sulphided to 75% S coverage [175]. Since the Mo edge differs from the S edge, this size effect is predicted to have an influence on the reactivity of the catalyst. In the STM studies mentioned, two types of crystallites were distinguished, defined as type I and type II crystallites. Type I crystallites consist of single slabs of MoS_2, whereas type II crystallites comprise multiple MoS_2 slabs. At annealing temperatures T_a (see section 5.2), during preparation below 673 K, only type I crystallites are formed, whereas at higher T_a, also type II crystallites have been observed [145]. Another effect, observed at higher temperatures, is the sintering of smaller crystallites into larger ones, which accumulate at the steps on the Au(111) substrate [142].

When the crystallites are prepared under more reducing conditions, i.e. a larger $p_{H_2} : p_{H_2S}$ ratio, deformed hexagonal crystallites are obtained, along with rhombic, trapezoid, and pentagonal structures [145]. In our case, the

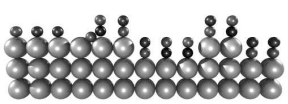

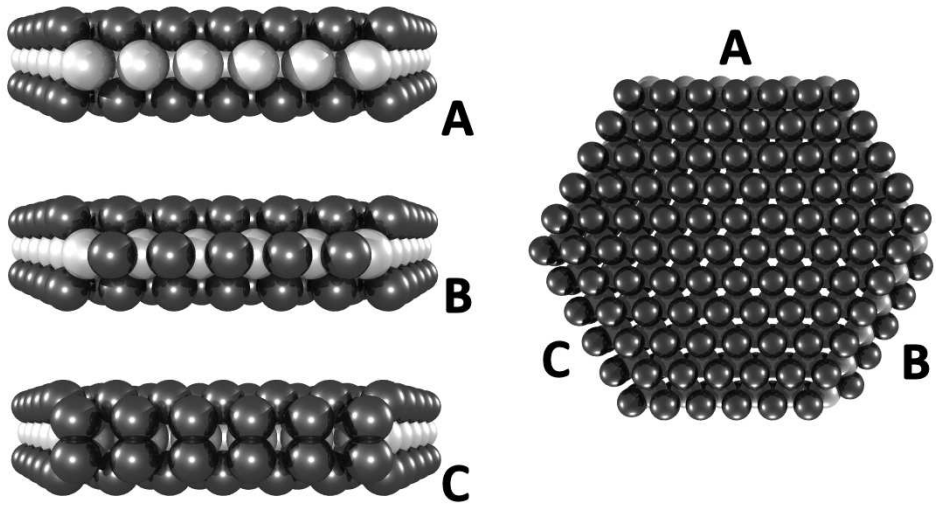

Figure 5.3: (A) A bare molybdenum edge, (B) sulphur monomers bonded to the molybdenum edge, (C) Sulphur dimers bonded to the molybdenum edge.

crystallites were deposited under sulphiding conditions, after which they were exposed to hydrogen, a reducing environment, in the reactor. Both the presence of the Mo edge, and the S edge were observed, as will be shown in section 5.4, probably in combination with adsorbed hydrogen. This indicates that, under more practical conditions, both edge terminations are present. The molybdenum edge is accompanied by the bright rim, which, to rule out support effects, is also observed when MoS_2 is deposited on carbon supports [177]. On the S edge, sulphur vacancies are created, when exposed to hydrogen; vacancy creation is also observed at the Mo edges, but only with pre-dissociated hydrogen at high temperatures [175]. The conversion of thiophenes, in particular the sterically hindered group of dibenzothiophenes, in the HDS process, mainly takes place via a pre-hydrogenation (HYD) route, rather than a direct desulphurization (DDS) route [179]. The edge terminations of the hexagonal crystallites, under HDS conditions, is predicted by DFT to consist of both Mo and S edges, with dissociated adsorbed hydrogen forming S-H groups. More specifically: (1) Mo edges with 50% S coverage, and 50% H adsorption, and (2) S edges, with 100% S coverage[3] and 100% H adsorption [160, 177, 180, 181], which is schematically depicted in figure 5.4.

Due to the various possible active edge sites, which act as adsorption sites, H donors, and activate C-S scission, there are numerous reaction pathways for thiophene to react to butene or butane. The process includes various

[3]which, under the influence of hydrogen, will also contain sulphur vacancies

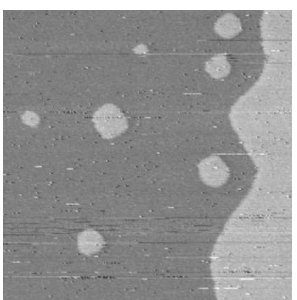

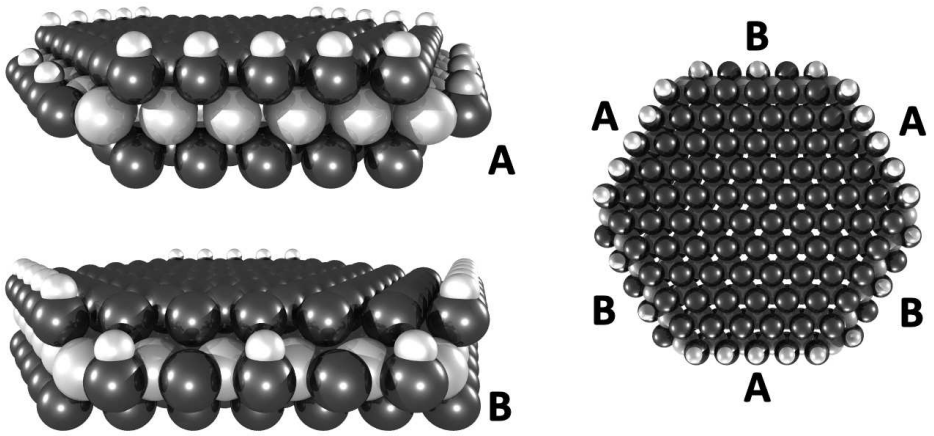

Figure 5.4: The edge termination of a MoS_2 crystallite under HDS conditions. Left: (A) An S edge, with 100% S coverage and 100% H adsorption; (B) An Mo edge, with 50% S coverage (S monomers) and 50% H adsorption. Right: Top view of the crystallite

hydrogenation steps, and a pre-hydrogenation step. The most recent reaction scheme is depicted in figure 5.5, adapted from reference [176]. The grey arrows represent very slow reactions. The top part shows the reaction intermediates on the sulphur edge, whereas the bottom part shows the reaction intermediates on the brim ("bright rim") sites of the molybdenum edge. The reaction scheme, in combination with the energy barrier calculations, give a few interesting predictions. Firstly, thiophene is found to prefer adsorption on the brim sites, whereas some of the reaction intermediates (e.g. 2,5-dihydrothiophene and cis-2-butenethiol) prefer to adsorb at a vacancy site on the S edge. Hydrogenation and H-transfer are favored on the brim sites, whereas C-S scission can occur on both the brim sites at the molybdenum edge, and the sulphur vacancy sites at the sulphur edge. The preferential site depends on the reaction conditions; under reducing conditions, C-S scission at the, in that case easily formed, S vacancies is favorable. Since desorption and diffusion of the reaction intermediates is fairly easy, the reaction mechanism under HDS conditions could be adsorption and pre-hydrogenation of thiophene at the brim sites, followed by diffusion to a vacancy site, where C-S scission takes place. A final important consideration is the regeneration of the active sites, which has a higher barrier at the S edge [143, 160, 176].

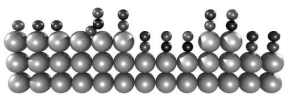

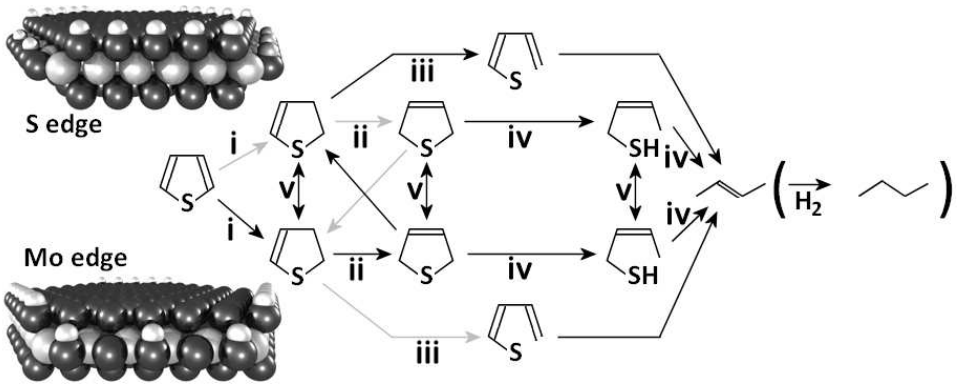

Figure 5.5: A schematic reaction scheme for the desulphurization of thiophene on either of the two edges, as defined in figure 5.4 under HDS conditions. The top part represents the S edge (vacancy model), whereas the bottom part represents the Mo edge (brim site model). (i) adsorption and pre-hydrogenation, (ii) hydrogenation, (iii) C-S scission (direct desulphurization), (iv) C-S scission in combination with hydrogenation, (v) diffusion. Grey arrows represent slow reactions [146, 176].

5.1.2 Enabling MoS_2 STM studies

When studying catalysis with STM, generally a well-prepared flat single crystal surface of the catalytic active material is used, which then is exposed to the particular reactants. In this case, however, one of the areas of interest is the morphological dynamics of MoS_2 nano-crystals under various conditions. Using a single MoS_2 crystal would be futile. A recipe for dispersing MoS_2 nano-crystallites on a conducting and chemically inert surface has been developed for STM studies on this reaction system – in short, molybdenum is evaporated onto the (111) surface of gold, in the presence of an excess of H_2S gas [145, 153]. Next to the inertness of bulk gold[4], the herringbone reconstruction onto its (111) surface provides good nucleation sites for highly dispersed metal islands [145]. In performing STM on the nano-crystallites, the bias voltage applied between tip and sample influence the apparent height of the crystallites. At increasing bias voltages, the apparent height asymptotically approaches the expected height for a single MoS_2 slab, 3.15 Å, whereas for small bias voltages, the apparent height goes to zero [153]. On the other hand, the distance between sample and tip also determines whether the current tunnels via the top sulphur layer (large distance), or directly to the molybdenum layer below (small distance). STM images in these two cases,

[4]Gold *nano*-particles are actually found to be catalytically very active for reactions such as CO oxidation [31–33]

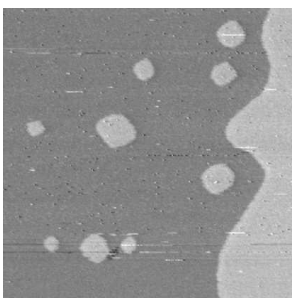

however, are reported to be quite similar, which makes it difficult, for example, to identify an S site on the surface [150].

5.1.3 MoS_2 catalysis in the ReactorSTM

The aim of this work was to study thiophene desulphurization in situ, under reaction conditions, with the ReactorSTM^{TM}, in order to investigate the influence of the conditions on the morphology of the crystallites. This included witnessing various steps in the reaction mechanism in situ, such as the binding of a thiophene molecule to a rim site, its conversion to reaction intermediates like thiolates, the creation of sulphur vacancies on the edges, and reaction of the intermediate species at these vacancies. To achieve this, the aforementioned recipe of depositing MoS_2 on Au(111) was used, and the surface was exposed at elevated temperatures to various mixtures of thiophene, hydrogen, and argon, at ambient pressures. The overall reaction studied is $C_4H_4S + 4H_2 \rightleftharpoons C_4H_{10} + H_2S$. Since both in preparing the catalyst, and performing the experiment, substances had to be used which are not commonly used with ultrahigh vacuum equipment (H_2S and thiophene), this was first performed as a pilot experiment on the ReactorSTM^{TM} Mark I, after some system adjustments. Then, the experiment was moved to the ReactorSTM^{TM} Mark II, described in detail in chapter 2[5].

5.2 Preparation

5.2.1 Setup adjustments

In order to make the ReactorSTM^{TM} compatible with the desulphurization experiment, adjustments had to be made at two fronts. Firstly, additions to the preparation chamber of the UHV system were necessary, and secondly, adjustments to the gas cabinet and the STM itself had to be made, to be able to run the experiment. Both will be discussed in this section.

To form the MoS_2 nano-particles, molybdenum is deposited on the surface, by electron beam deposition, in an H_2S background. For the molybdenum deposition, an E-beam evaporator [68] was installed on the UHV chamber, in combination with a quartz microbalance [167], for monitoring the deposition rate. H_2S was supplied to the chamber via a standard leak

[5]This work has been done in the framework of NIMIC [57], in cooperation with the company Albemarle Catalysts BV.

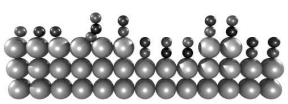

valve. The tubing, valves, and rotary pump [168] for the H_2S gas supply system, are all corrosion resistant.

Because one of the reactants, thiophene, is a liquid at room temperature (T_b = 84℃), the existing gas cabinet and parts of the ReactorSTM^{TM} had to be adapted, in order to offer gaseous thiophene to the MoS_2 catalyst, and to prevent thiophene from condensing in the gas lines and reactor[6]. Furthermore, clogging of the mass flow controllers, pressure regulators, and pumps had to be prevented. Figure 5.6 shows a schematic drawing of the modifications applied to the system.

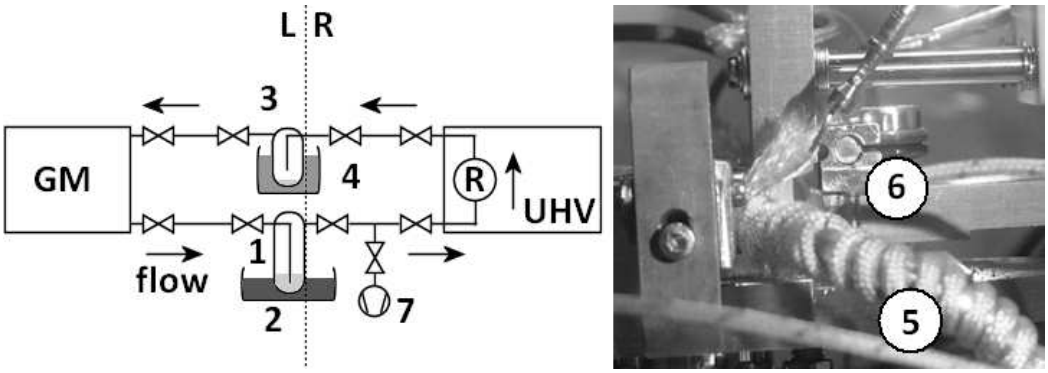

Figure 5.6: (Left) A schematic drawing of the modifications applied to the gas lines and ReactorSTM^{TM}. Left (L) of the dashed line, the equipment is at room temperature, while right (R) from the dashed line, all equipment is heated. (GM) The gas manifold, (1) thiophene flask, (2) heat bath, (3) cold trap, (4) ice bath, (R) reactor, (7) rotary pump. (Right) A detail photograph of the ReactorSTM^{TM}, showing the heated gas lines (5) and the cartridge heater heating the reactor (6).

Figure 5.6 schematically shows the flow path from the gas manifold (GM), via the reactor (R), back to the gas cabinet. The gas manifold supplies a mixture of argon and hydrogen, which bubbles through a flask containing thiophene (1), after which it enters a teflon tube. It is possible to heat up the thiophene, via a heat bath (2), in order to control the vapor pressure of thiophene. This opens the possibility of changing the amount of thiophene

[6]The modifications were only prepared for the gas cabinet and parts of the ReactorSTM^{TM} Mark I, which is discussed in this section. For the experiments performed in the ReactorSTM^{TM} Mark II, a separate gas cabinet was constructed, and during experiments, the whole STM chamber was heated to 120℃, in order to prevent C_4H_4S from condensing in the chamber or reactor.

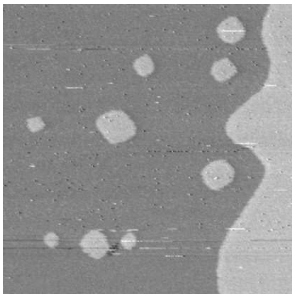

offered to the catalyst. To the right of the dashed line in the schematic, all components are heated. The gas lines outside the UHV are heated by heating tapes [65], while the gas lines inside the vacuum system are heated by a high resistance Cu alloy wire ($R = 6.8\ \Omega/\mathrm{m}$) (5). The reactor is heated by a cartridge heater (6) [169], clamped in a copper block, in order to create good thermal contact between the heater and the reactor. Both systems are equipped with separate thermocouples, for accurate temperature monitoring. A rotary pump (7) was added to the inlet, to be able to pump down the reactor, in case of a severe leak of the reactor. At the end of the heated gas line, a cold trap (3), cooled by an ice bath (4), was installed, to liquify the thiophene in the exhaust line, before the exhaust continues to the gas cabinet.

5.2.2 Sample preparation

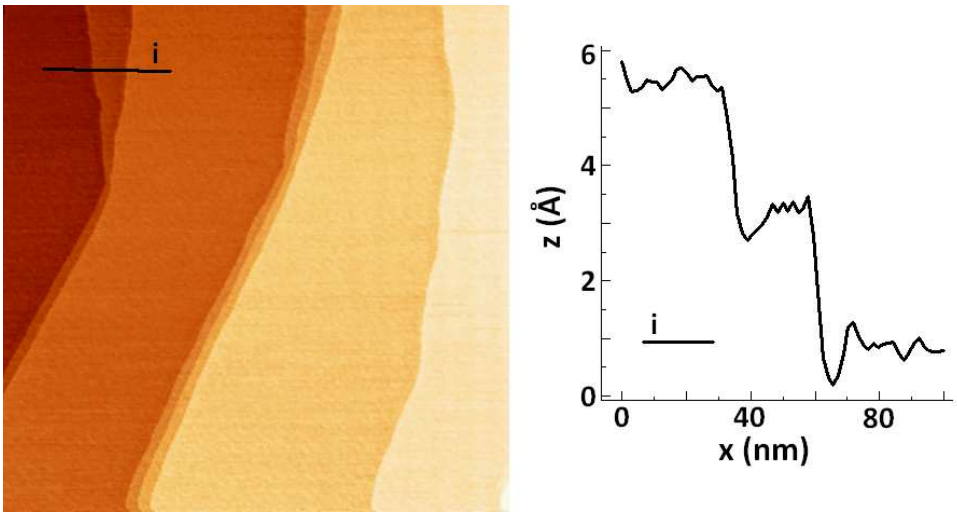

Figure 5.7: (Left) 400x400 nm^2 STM image (V_b = 80 mV; I_t = 0.2 nA), showing the clean Au(111) surface exhibiting large terraces. (Right) A height profile (i), showing the monatomic step height on Au(111) to be 2.3 Å.

As described in section 5.1, a gold surface, cut in the (111) direction, was chosen as a good support for MoS_2 nano-particles. First, the gold surface was cleaned by repeated cycles of 0.6 kV Ar^+ ion bombardment and annealing under UHV at 850 K. Figure 5.7 shows the surface of the prepared gold sample, which we used as a support for growing the MoS_2 crystallites. STM images obtained in the hours following this image show little variation, indicating that the surface is very stable; the height profile, in figure 5.7,

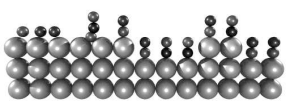

shows the monatomic step height of Au(111) to be 2.3 Å, which is well in accordance with the theoretical value of 2.36 Å [170].

Before creating the nano-particles, the cleanliness of the gold crystal was checked by LEED/Auger and STM. The procedure of creating the nano-particles, following the cleaning of the gold sample, is schematically depicted in figure 5.8.

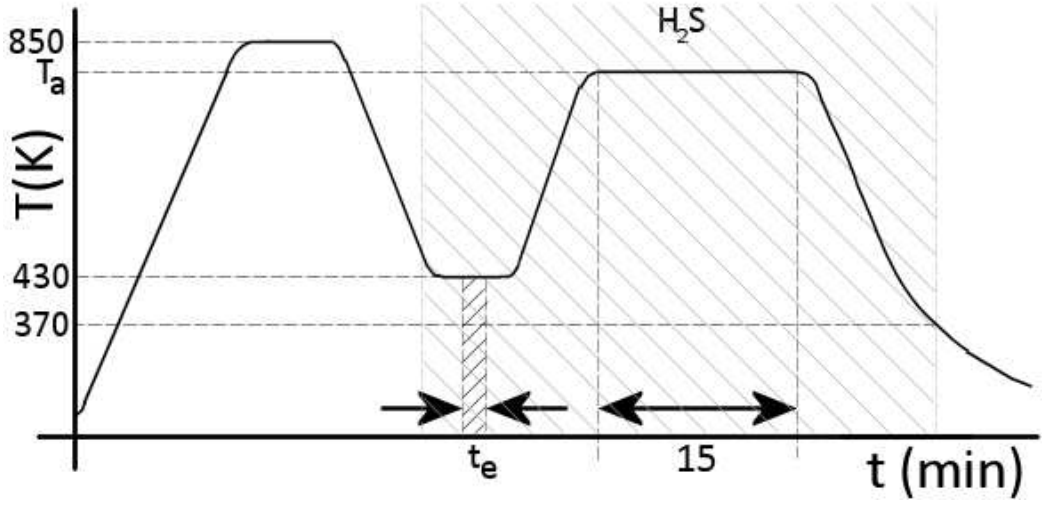

Figure 5.8: The graph shows the temperature evolution of the sample during the MoS_2 nano-particles preparation on Au(111) [142]. T_a represents the temperature at which the sample is annealed during H_2S exposure, after the evaporation of molybdenum. t_e is the duration of molybdenum evaporation. It is tuned such, that a coverage of 15 – 20% molybdenum is obtained.

Figure 5.8 starts with the final annealing step of the Au(111) surface at 850 K, after which the sample is cooled down to 430 K, which temperature is maintained. At this point, the UHV chamber is backfilled with H_2S, at a pressure of $1 \cdot 10^{-6}$ mbar. This is done because an excess amount of sulfur should be offered to the surface, in order to form MoS_2; backfilling the UHV chamber with $1 \cdot 10^{-6}$ mbar of H_2S corresponds to one monolayer of H_2S exposure to the surface per second. The evaporation time t_e is chosen such, that a coverage of 15 to 20 % MoS_2 nano-particles is obtained in the end; at a molybdenum flux of 70 nA, $t_e \approx 20$ seconds. After deposition, the sample is annealed for 15 minutes at temperature T_a, which for different preparations is between 600 K and 800 K, maintaining the H_2S background. When the sample is cooled down to room temperature, the H_2S valve is shut.

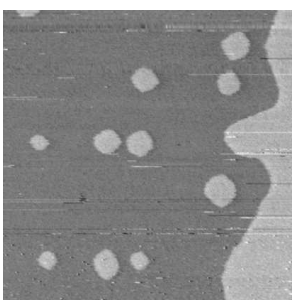

5.3 In situ HDS of C_4H_4S on MoS_2 crystallites

The first aim was to learn whether this catalytic system would be a suitable subject for investigation with the ReactorSTM. As mentioned in the introduction to this chapter, it was decided to first perform this experiment on the ReactorSTM Mark I, to discover the effects of H_2S and thiophene on the ultrahigh vacuum system. In addition, a study of the behavior of the STM itself, under reaction conditions for this catalyst, could be done. Also the capability of the STM to image the MoS_2 nano-crystallites, as well as the fact whether we could obtain a measurable reaction rate with the mass spectrometer, could be studied. Since the results of the pilot study on the ReactorSTM Mark I proved to be positive, the step to the ReactorSTM Mark II was taken. The results obtained by both STM's are mixed throughout the following sections. The first section describes the findings on the chemical composition of the crystal, using Auger electron spectroscopy. The section covering the reaction kinetics is followed by the section which finishes with an in-depth discussion about the structure of the catalyst.

5.3.1 Auger electron spectroscopy

Auger electron spectroscopy (AES) provides information about the amount of certain chemical elements present on a surface. By performing AES on our crystal, the chemical composition of the sample, before and after preparation of the MoS_2 crystallites on the Au(111) surface, and before and after exposure to reaction conditions, could be determined. Figure 5.9 shows four Auger spectra obtained in four different situations. Graph 5.9 A shows the spectrum for clean Au(111). 5.9 B shows Au(111), with MoS_2 evaporated onto it, which has not been exposed to C_4H_4S/H_2. 5.9 C shows Au(111)/MoS_2 after exposure to reaction conditions. 5.9 D shows Au(111) without MoS_2, after exposure to the reactants. And finally, 5.9 E shows the gold surface onto which an excess of molybdenum has been evaporated.

The gold peak at 69 eV was observed in all spectra, which has been used to verify whether the sample has been placed in the electron beam. Apart from this, there are various differences between the spectra in figure 5.9. The clean surface, shown in spectrum A, does not have any other peaks but the gold peak. Spectra B, C, and D all exhibit sulphur peaks at 152 eV. In spectrum B, the sulphur signal is very weak, whereas the peaks in spectra C and D are strongly pronounced. The sulphur peak in spectrum B comes only

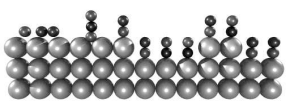

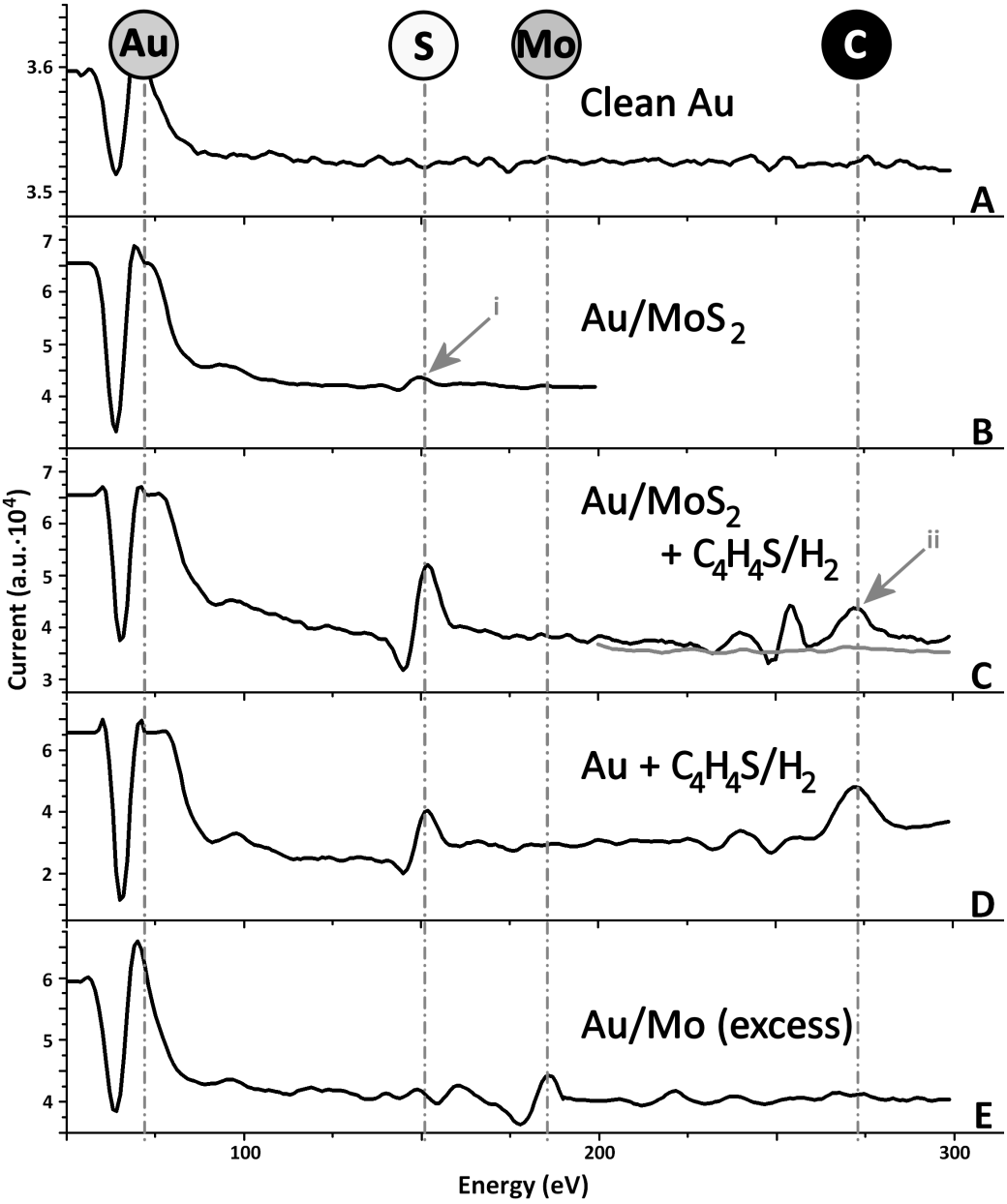

Figure 5.9: Auger spectra of Au/MoS_2 in the following situations: (A) Clean Au(111), (B) MoS_2 evaporated onto Au(111), (C) Au/MoS_2 after C_4H_4S/H_2 exposure, (D) Au(111) after C_4H_4S/H_2 exposure, (E) Excess molybdenum deposition ($\approx$ 1 ML). The peaks used for identification are 69 eV (Au), 152 eV (S), 186 eV (Mo), and 272 eV (C)

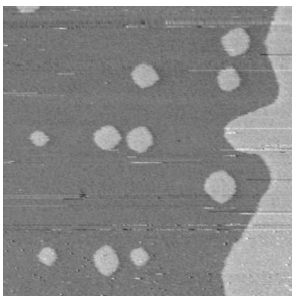

from the MoS_2 crystallites, since the crystal has not been exposed to reaction conditions. In spectra C and D, the surface has been exposed to 1.2 bar of thiophene and hydrogen/argon at 120℃. After exposure, thiophene remains on the gold surface, which can be either adsorbed or condensed – the crystal is cooled down to room temperature, prior to a transfer to the AES. In addition, spectra C and D also exhibit carbon peaks at 272 eV, indicating the presence of a carbon containing species, which could be thiophene. The carbon peak in spectrum C, however, shows a different kind of behavior than the one in spectrum D. When the bare gold surface is exposed to thiophene (D), the carbon peak is stable, whereas the carbon peak seems to disappear after the initial Auger scan of the surface, which had been catalytically active (C). The reason for the disappearance of the carbon peak in spectrum C is not exactly known. It could possibly be ascribed to a process of diffusion and reaction, under the influence of the electron beam, but this hypothesis needs verification. The only spectrum in which a clear molybdenum peak can be seen is spectrum E, in which the sample was exposed to an excess of molybdenum, with respect to the amount aimed for in the desulphurization experiments. With the quartz crystal monitor calibrated for molybdenum, it was determined that, for a full monolayer of molybdenum, an evaporation time t_e (see fig. 5.8) of 3 minutes would be needed. In the case of spectrum E, the evaporation lasted for 1 minute, leading to 1/3 Mo coverage. For these experiments, however, the coverage aimed at was between 5 and 10 %, which translated into an evaporation time between 10 and 20 seconds. In this case, the molybdenum peak at 186 eV was sufficiently low to disappear into the background noise.

5.3.2 Reaction kinetics

The adjustments applied to the ReactorSTM^{TM}, as described in section 5.2, allowed a mixture of argon, hydrogen, and thiophene to be offered to the catalytic surface in the reactor. During an experiment, the direct leak from the Kalrez seal to the UHV for residual gas analysis, with the QMS (chapter 1), was used. The amount of hydrogen offered to the surface is easy to control, by altering the ratio between the mass flow controller settings for argon and hydrogen. The amount of thiophene is difficult to adjust during an experiment. To carry this out, the vapor pressure should be increased, which is only possible by changing the temperature of the heat bath, which is a slow process. In practice, thiophene is the limiting factor for the reaction rate in the reactor; even bubbling the smallest possible amount of hydrogen, set by the gas manifold, through the thiophene initiated no decrease of reaction product yield. Because of this, and the low reaction rate, it was difficult

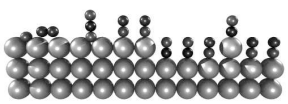

to conclude, from a flow experiment, whether the surface was catalytically active or not. Therefore, a batch experiment was performed, by closing the inlet and exhaust valve to the reactor at a set ratio of $Ar/H_2/C_4H_4S$, at a temperature of 120℃, and a pressure of 1.2 bar. In a batch experiment, it was expected that the leak of the reaction products would have a different time evolution than those of the reactants, because the reactants were being consumed, whereas the products were being produced. In addition to this experiment, a batch control experiment was performed, using the same settings, but exposing the reactant mixture to a clean Au(111) surface, without MoS_2 crystallites evaporated onto it. The outcome of both experiments are shown in figure 5.10.

Panel A, in figure 5.10, shows the evolution in time of reactants and reaction products, for the batch experiment with MoS_2 crystallites on the surface, whereas the panel B represents the control experiment. The bluish lines correspond to the reactants, hydrogen (amu 2), and thiophene (consisting of amu 45, 58, and 84). The reddish lines reflect the reaction products: H_2S (amu 34), butane (amu 29, 43, and 58), and butene (amu 41 and amu 56 (not checked)). Mass 58 corresponds both to a reactant and a product, and is green; mass 20, corresponding to doubly ionized argon, is inert and grey. The first difference between these two graphs is the level of the reaction products, which, in the upper panel, are order(s) of magnitude higher than in the control experiment, whereas the thiophene signals are more or less in the same range. There is, however, a large difference in the level of hydrogen between the two experiments. But in the control experiment, there was still an excess of hydrogen with respect to thiophene, and as mentioned earlier, hydrogen is not the limiting factor in these experiments. Secondly, as can be seen in the upper panel, the slopes of the masses corresponding to butane seem to be different from the slopes of the masses corresponding to thiophene. In the control experiment, in the lower panel, this effect cannot be seen – here the differences in slopes seem only marginal, and could be ascribed to the fact that each type of molecule has a different leak rate into the vacuum system. Moreover, the graphs with the lowest levels approach the detection limit of the mass spectrometer, which can be translated into the large variations in the measured signals. An effort to approach the difference in slopes more qualitatively, in both the real and the control experiment, is discussed in the next paragraph.

To determine the reactivity of the catalyst, it is necessary to know whether the ratios between the QMS signals are changing in time. During the batch experiment, in addition to a reaction taking place, the reactor was also being

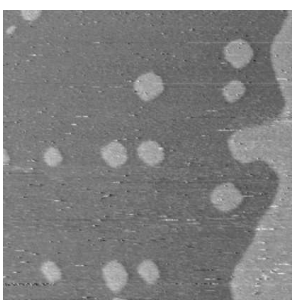

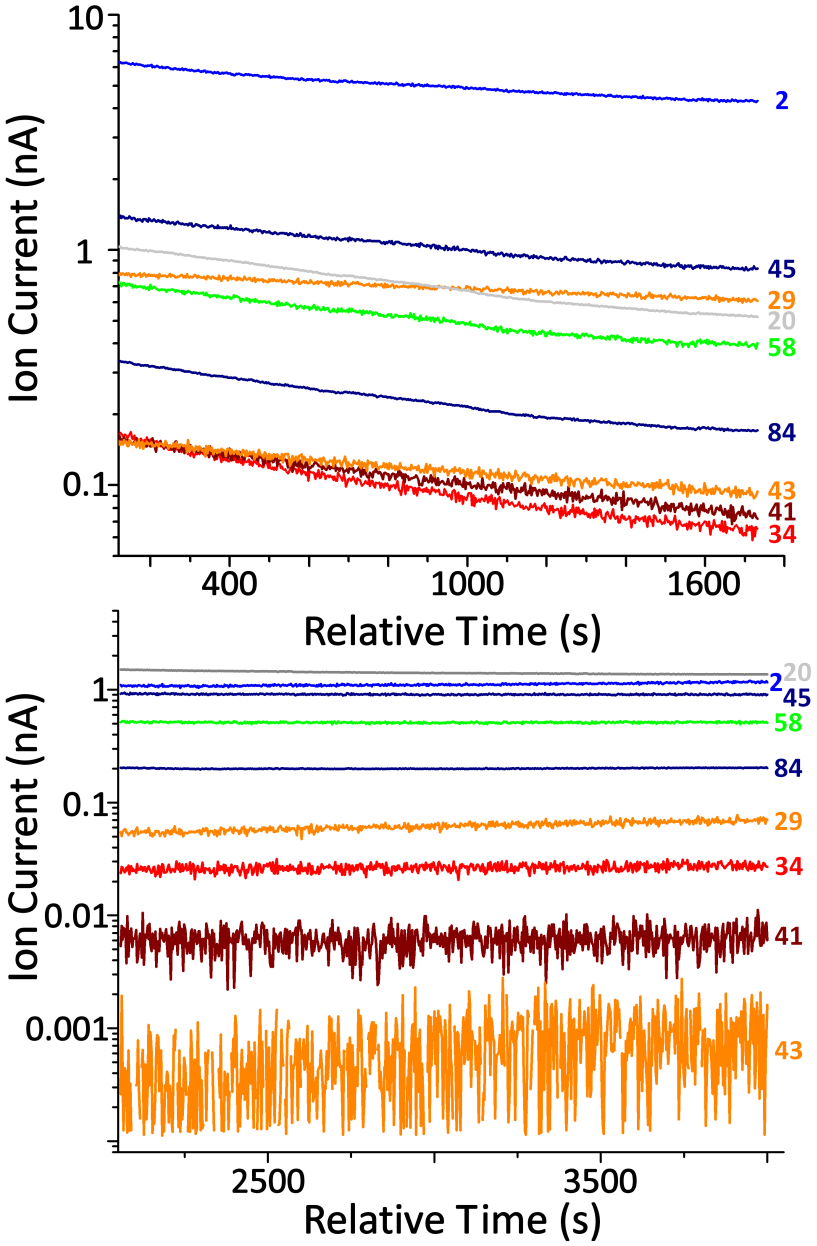

Figure 5.10: (Upper panel) The batch experiment, in which the MoS_2 islands on a Au(111) support were exposed to a mixture of argon, hydrogen, and thiophene. (Lower panel) The batch experiment, in which a clean Au(111) surface was exposed to the same reactant composition. Both experiments were performed at $T = 120℃$ and $p = 1.2$ bar.

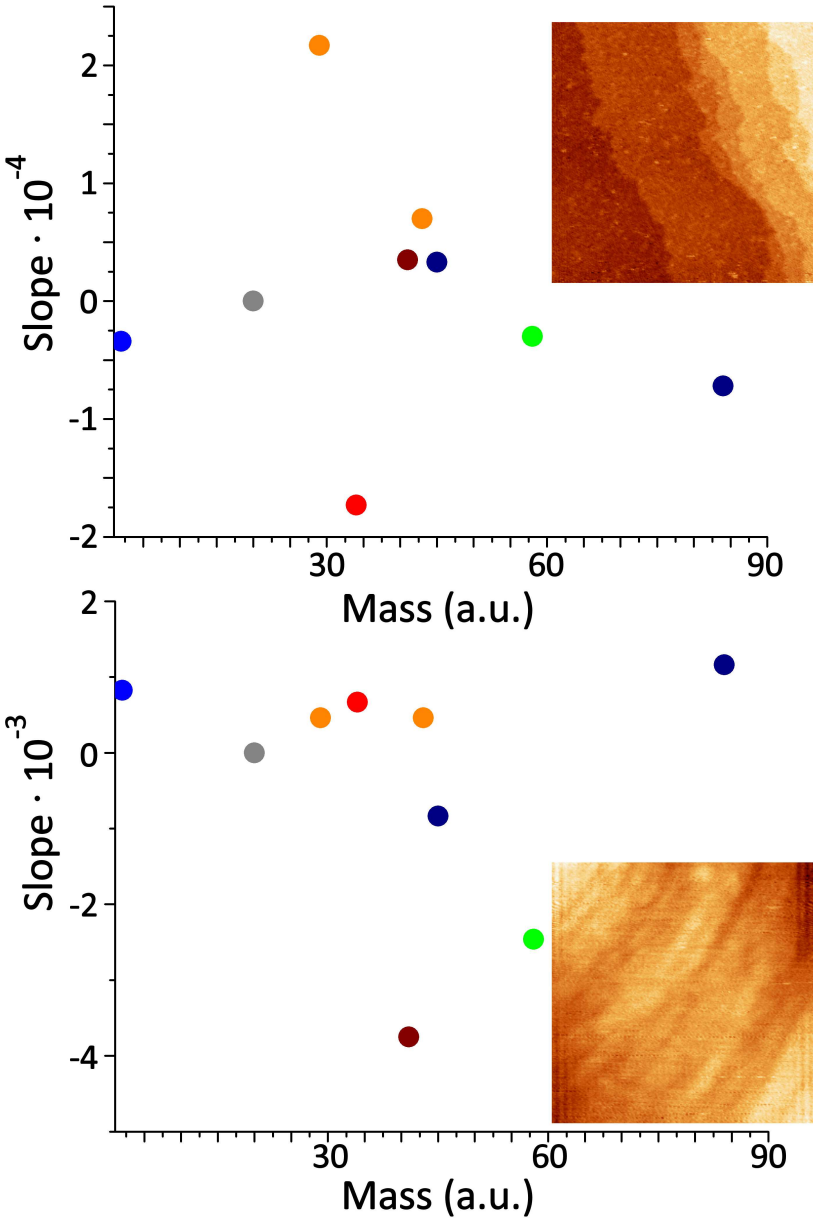

Figure 5.11: (Upper panel) The slopes of the QMS signals in the real experiment, corrected to the argon slope. The STM image is 100x100 nm^2, with $V_b = -80$ mV, and $I_t = 0.15$ nA. (Lower panel) The slopes of the QMS signals in the control experiment, corrected to argon slope. The STM image is 100x100 nm^2, with $V_b = 80$ mV, and $I_t = 0.2$ nA.

slowly emptied, via the small leak into the UHV system, for which a correction must be made. Starting from a small example: suppose there are

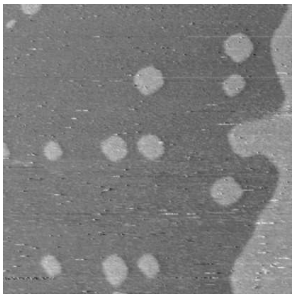

two gases, A and B, in a volume with a ratio of A:B = 1:10. If no reaction between A and B is taking place, for each molecule of A leaving the volume, 10 molecules of B will leave the volume. The time evolution of gas A and B, on a linear scale, will therefore be different. On a logarithmic scale, however, the slopes of A and B will be the same. So the first step in determining the differences between the slopes in this experiment, was to fit an exponential function to the QMS signals, to plot these functions on a logarithmic scale, and to determine the slopes of the lines resulting from this operation. Next, in this experiment, there is a carrier gas, argon, which is not participating in the reaction. The slope of argon, therefore, should be 0 if there was no leak. To correct for the leak, the values of the slopes of all the mass spectrometer signals were subtracted from the value of the slope of the argon signal. If the outcome of this simple calculation for a certain signal is negative, it means that more of this specific material is disappearing than is leaking out, meaning that this material is being consumed. On the other hand, when the outcome is positive, more material is leaking out than should happen, meaning that this material is being created in the reactor. This operation has been done, on both the real and the control experiment, of which the results are shown in figure 5.11. The color codes correspond with those used in figure 5.10. Panel A again reflects the experiment in which the catalyst is used; panel B matches the control experiment. A general look at these graphs indicates that, in the upper panel, the reaction products corresponding to butane indeed have larger slopes, when compared to the signals corresponding to thiophene, whereas the slopes are more or less the same in the control experiment. This supports the findings discussed in the last paragraph. However, there are several question marks here. During the experiment, H_2S seems to have been consumed, rather than produced – perhaps the fact that H_2S was used to create the MoS_2 crystallites compromises this signal, since H_2S is probably spread throughout the system. The marginal addition of the H_2S, created during the reaction, cannot nearly compensate for the H_2S, degassing from the walls and being evacuated by the pumps. Also, despite the fact that thiophene had a negative slope, its ionized mass 45 had a positive slope; this was reversed in the control experiment. In addition, the signal of mass 45 was higher than the signal of mass 84 (see fig. 5.10); of all the substances used, the only combination of atoms adding up to 45 was S=C-H^+, which could only have originated from thiophene. An explanation for this is not yet available.

In the upper right hand corner of both graphs, in figure 5.11, an STM image obtained by the ReactorSTM Mark I, corresponding to the situation of that particular experiment, is shown. Although the image quality is poor,

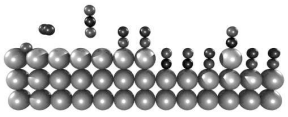

it can clearly be seen that, in the case of the catalytically active surface, there are small MoS_2 crystallites dispersed over the surface. In the case of the control experiment, the surface is not covered with these nano-particles.

5.4 Catalyst structure and reactivity: Experimental

In the initial study, performed on the ReactorSTM Mark I, several of the aspects described in section 5.1.1 were observed. As argued in section 5.1.2, Au(111) was chosen as a support for the MoS_2 nano-crystallites; figures 5.12 and 5.14 show the STM images we obtained under vacuum conditions[7]. Figure 5.12 shows the effect of the bias voltage on the apparent height of the MoS_2 crystallites. For type I crystallites, the apparent height asymptotically approached a value of 3.0 Å at large bias voltages, starting from very small heights at small bias voltages. This effect has been ascribed to the interaction of the crystallites with the Au(111) substrate. The semiconducting properties of the crystallites, in this situation, were slightly influenced, leading to a change in the band gap to -1 V. Tunneling within this band gap gave mixed Au/MoS_2 states, which at low bias voltages were dominated by the gold substrate. When the bias voltage was gradually increased, more states of the crystallites became available for tunneling, due to the integration of the state density, increasing the apparent height of the crystallites in the STM images. Outside the band gap, the electronic structure was dominated by the MoS_2 crystallites, translating into an apparent height of 3.0 Å, approaching the real height of a S-Mo-S slab of 3.16 Å. Image 5.12 A was obtained with a bias voltage of -80 mV. From the STM image and the corresponding height profile a, it can be seen that the MoS_2 crystallite, indicated by the hatched area, barely stands out, with respect to the gold layer below. In comparison, image 5.12 B was recorded with a bias voltage of -1.9 V. The matching height profile b shows that the apparent height of the MoS_2, in the profile again corresponding to the hatched areas, is now 2 Å, approaching the value of a single S-Mo-S slab [143].

A second effect, which has been observed and used to characterize the

[7]Actually the "vacuum conditions" comprised a $p <\sim 10^{-4}$ mbar of mainly H_2 exposure, since the volume of the reactor, during STM measurements, was not evacuated, and the main residual gas was H_2. This already translates into a slight morphological change of the MoS_2 crystals, from triangular into deformed hexagonal, as can be seen in figure 5.14 D and F; this will be discussed at a later stage in this section

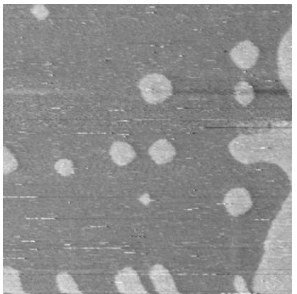

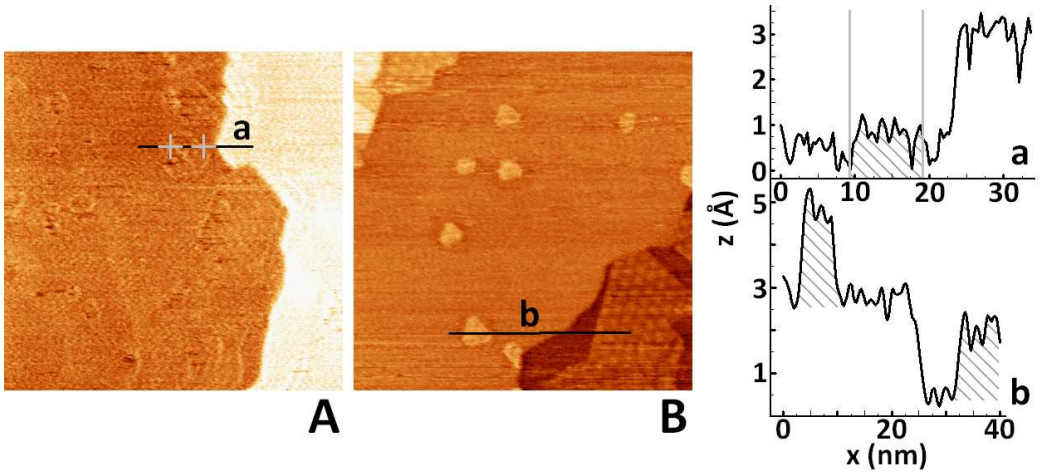

Figure 5.12: Two 100 x 100 nm^2 STM images of MoS_2 on Au(111). For image A, $V_{bias} = -80$ mV, $I_t = 0.2$ nA; for image B, $V_{bias} = -1.9$ V, $I_t = 0.15$ nA.

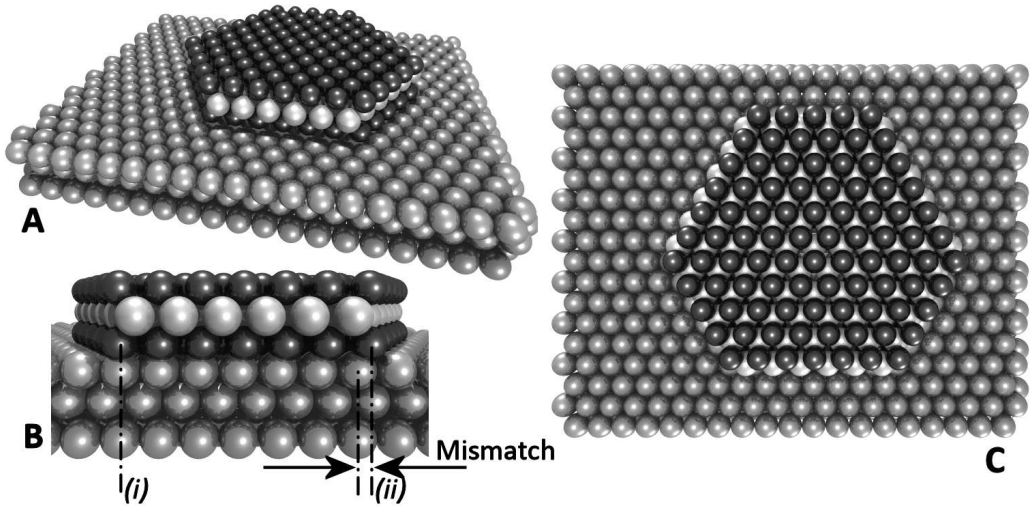

Figure 5.13: (A) A 3D impression of a MoS_2 crystallite on a gold (111) substrate. (B) A side view of image (A), showing the difference in lattice spacing between the crystallites and the substrate from which the Moiré pattern originates, indicated as "mismatch". (C) A top view of image (A).

MoS_2 crystallites with the ReactorSTM Mark I, was the sintering and accumulation of MoS_2 at the Au(111) steps, occurring at higher annealing temperatures T_a, as shown in figure 5.14. Since the resolution of the ReactorSTM Mark I was insufficient to atomically resolve 10 to 20 Å wide MoS_2 crystallites, a $T_a \approx 800$ K was used, in order to create these larger crystallites. Since the interatomic distances of unreconstructed Au(111) (2.88 Å),

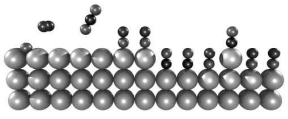

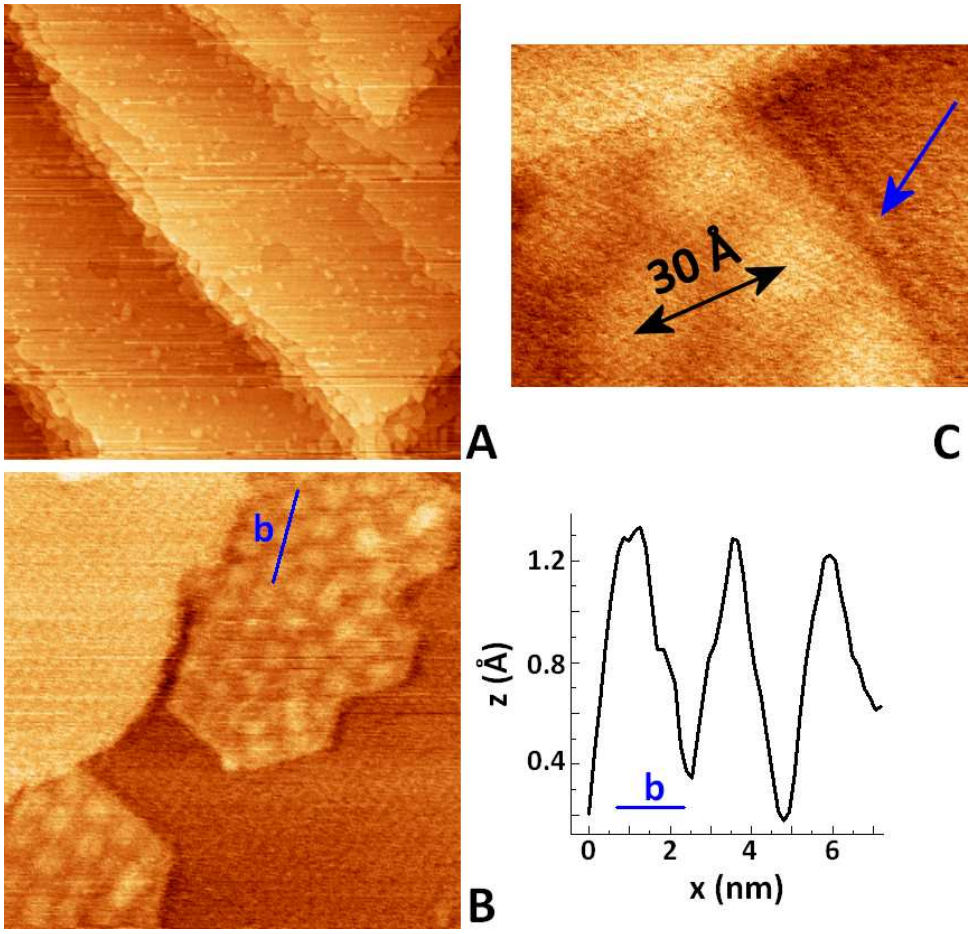

Figure 5.14: (A) A 400 x 400 nm^2 STM image of Au(111), with MoS_2 crystallites on it. (B) A 35 x 35 nm^2 STM image. Corresponding height profile (b) shows the corrugation of the Moiré pattern. (C) A 10 x 10 nm^2 STM image, in which the edge states of the crystallites can be seen. The periodicity of the Moiré pattern is 30Å. All STM images in this figure were obtained at $V_b = -1.9$ V and $I_t = 0.15$ nA.

which was believed to support the crystallites [145], and MoS_2 (3.15 Å) differ, a Moiré pattern should appear, due to the lattice mismatch. The lattice mismatch is shown schematically in the ball models in figure 5.13. (A) shows an on scale 3D impression of a MoS_2 crystallite on Au(111), for which a side view and top view are shown in 5.13 B and C. In the side view, the lattice mismatch, leading to the Moiré pattern between Au and MoS_2 is indicated by the arrows. Three STM images are shown in figure 5.14, which were obtained at room temperature and under exposure to the residual gases in the reactor,

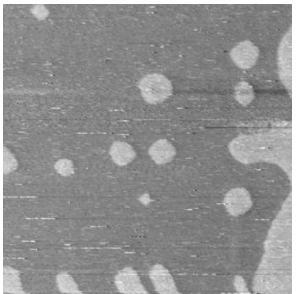

which was not being evacuated during the STM operation. Image 5.14 A is a large scale scan, showing both sintered MoS_2 crystallites, collected at the Au(111) steps, and 10 to 20 Å MoS_2 nano-particles, scattered on the gold terraces. The small scale images 5.14 B and C, and also figure 5.12 B, reveal more detailed information about the MoS_2 structure. The nano-crystallites on the terraces, as visible in image 5.12 B, exhibited a deformed hexagonal structure, ascribable to the reducing conditions in the reactor volume (see footnote 7); the residual gas consisted mainly of hydrogen. The height of the crystallites, indicated in the corresponding height profile in figure 5.12 b, was 2 Å, corresponding to a single S-Mo-S slab. Furthermore, the bright rim along the edges of the nano-crystallites was slightly visible, although it was difficult to distinguish in individual height profiles. In image 5.14 C, the bright rim along the edge is more clearly distinguishable, and is pointed out by the blue arrow. The larger MoS_2 patches, shown in images 5.14 B and C, clearly exhibit an overlayer structure, with a periodicity of 30 Å. The z-corrugation of this corrugation is about 1 Å, which can be seen in the height profile b, corresponding to figure 5.14 B. For a non-rotated hexagonal overlayer – the MoS_2 overlayer is not rotated with respect to the gold substrate – with lattice constant a_o on a hexagonal substrate with lattice constant a_s, a buckling would be expected, due to the atoms of the overlayer structure alternatingly being positioned at on-top sites and high-coordination sites. This buckling would have a periodicity of $a_s \cdot a_o/(a_o - a_s)$ [186]. For $a_o = 3.15$ Å and $a_s = 2.88$ Å, this leads to a periodicity of 33.6 Å, which corresponds well with the distance measured between the maxima of the Moiré pattern, indicating that the structures observed in the STM images are MoS_2 crystallites.

However, as can be clearly seen in the STM images in figure 5.12 B and 5.14 B, and as mentioned in footnote 7, the shape of the crystallites on the Au(111) terraces is not triangular, but deformed hexagonal. The question of what happens under reaction conditions needs to be addressed, since the gas composition in the reactor of the STM, during a "vacuum" experiment, consisted mainly of hydrogen, one of the reactants in the hydrodesulphurization process. Despite the fact that the research reported in the literature ([145, 160, 175, 177, 179–181]) has not been performed under reaction conditions, the experimental studies include investigations of the interaction of MoS_2 crystallites with hydrogen and thiophene separately, and the theoretical DFT studies elaborate on the morphology and edge terminations, under practical HDS (reducing) conditions. These studies, as described in section 5.1.1, reveal a complex interplay between the different aspects of the reaction mechanism, and the crystallites' morphology, under different environmen-

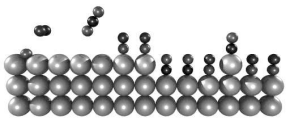

tal conditions. The effect on the reactivity and reaction mechanism of the changing edge termination, under the influence of the size of the crystallites, is unknown. Also, the experimental studies have not been performed in situ under reaction conditions. In addition, a change in the chemical potential is predicted, by density functional theory, to change the active sites and the structure of MoS_2 [160]. In summary, this theoretical study investigated the effect of the sulphur chemical potential μ_S on the sulphur saturation of the Mo and S edges of MoS_2 crystallites. For the Mo terminated edge, in the physically realistic range, the S coverage is expected to be 50 %; only at a very high μ_S will there be 100 % coverage. Sulphur coverage of < 50 % is only stable outside the physically realistic range of μ_S. For the S terminated edge, 100 % coverage is expected, in the realistic range for μ_S; formation of S vacancies will only occur at low values of μ_S. Sulphur exchange between the edges might occur in this situation. The absence of experimental studies, under realistic conditions, in combination with theoretical studies predicting differences in catalytically active sites, between vacuum and high-pressure conditions, confirms the importance of studying this reaction system in situ, under reaction conditions, which was the target with the ReactorSTM. During the first runs of this experiment on the ReactorSTM Mark I, knowledge of whether the reaction system was suitable for study with this type of machine was required. The STM images, obtained by the ReactorSTM Mark I, resolved the MoS_2 crystallites on the Au(111) surface, as shown in figure 5.14. The batch experiment, as described in section 5.3.2, indicated a measurable catalytic activity of the surface. Together, they have proven the suitability of the ReactorSTM for this catalytic system. In addition, the H_2S and thiophene, necessary for sample preparation and desulphurization experiments, did not prove to become a serious handicap for the ultrahigh vacuum system. There remained, however, a major issue with respect to the experiment: under reaction conditions, the tip approach was very unreliable. On many occasions, the tip did not detect a tunneling current, i.e. it either got stuck or the apex was covered by some insulating layer. And in most of the few cases when the tip did find the surface, a tip crash occurred. One of the possible explanations is the presence of a cold spot in the reactor; as described in section 5.2, an external heating cartridge was used for heating up the reactor, which, due to its position and the low thermal conductivity of stainless steel, might not be able to heat up all parts of the reactor equally. Thiophene might condense onto a cold spot (in which "cold" means below 84℃) on the tip holder or the tracks along which the tip holder slides, affecting the properties of the approach motor. Perhaps the acceleration required to make the tip holder perform its stick-slip motions exceeded the maximum acceleration provided by the piezo element. Another possibility is

the presence of sulphur-containing molecules covering the tip apex, making it electrically insulating. Additionally, the resolution of the ReactorSTM Mark I, under reaction conditions, was too poor to atomically resolve the crystallites, edge vacancies, and the large organic molecules adsorbed onto the Mo and/or S edges; the edges would also be hard to distinguish.

All in all, the pilot experiment performed on the ReactorSTM Mark I was successful in imaging and detecting reactivity, however, with poor resolution and unreliable tip approach. Both the success, as well as the drawbacks, lead to repeating the experiment with the ReactorSTM Mark II, in which it was hoped to observe the dynamics of the morphology of the crystallites, under reaction conditions, as well as the various reaction steps. An attempt to solve the approach issue by heating up the whole SPM chamber to 110℃ during STM operation was made. The initial findings are summarized in figure 5.15. Image A and B show the clean gold surface, A on a large scale, showing the herringbone reconstruction, and B on the atomic level. The reconstruction on the Au(111) surface originates from the reduced coordination number of the surface atoms, which are compressed by about 5 % along the $1\bar{1}0$ direction. This leads to two different domains, an fcc domain, and an hcp domain along the $11\bar{2}$ direction. These domains are separated by the gold atoms near the bridge positions of the bulk layer below, which appear as bright lines in the STM image. The reconstruction has a $22\text{x}\sqrt{3}$ unit cell. On a larger scale, these domains exhibit a zigzag pattern, with angles of 120°, due to elastic interactions. This zigzag pattern resembles a fish scale, hence the name "herringbone" reconstruction [145, 161, 162]. Image C, in figure 5.15, shows the gold surface when more then a monolayer of molybdenum is deposited. The surface is characterized by blobs, which seem to have a preference for buckling at the steps. From the height profile *c* can be seen that the difference in height between two terraces is 6 Å, which does not correspond to any integer, multiplied by the monatomic step height of Au(111)[8], but does correspond to a multiple step of some kind, rather then a single step. Along the steps, "speed bumps" of accumulated material exist, also with a height of 6 Å, as can be seen in the height profile. Finally, image D shows an STM image from a successful MoS_2 deposition experiment in the ReactorSTM Mark II. The quality of the image is not very high, but the characteristic Moiré pattern can be distinguished. The step height of the crystallites is 3 Å, as can be seen in height profile *d*. Although MoS_2 crystallites have been successfully created in this experiment, the recipe has not yet been optimized. The small

[8]This might arise under the influence of Au-Mo alloying, which is discussed in the appendix at the end of this chapter

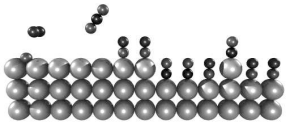

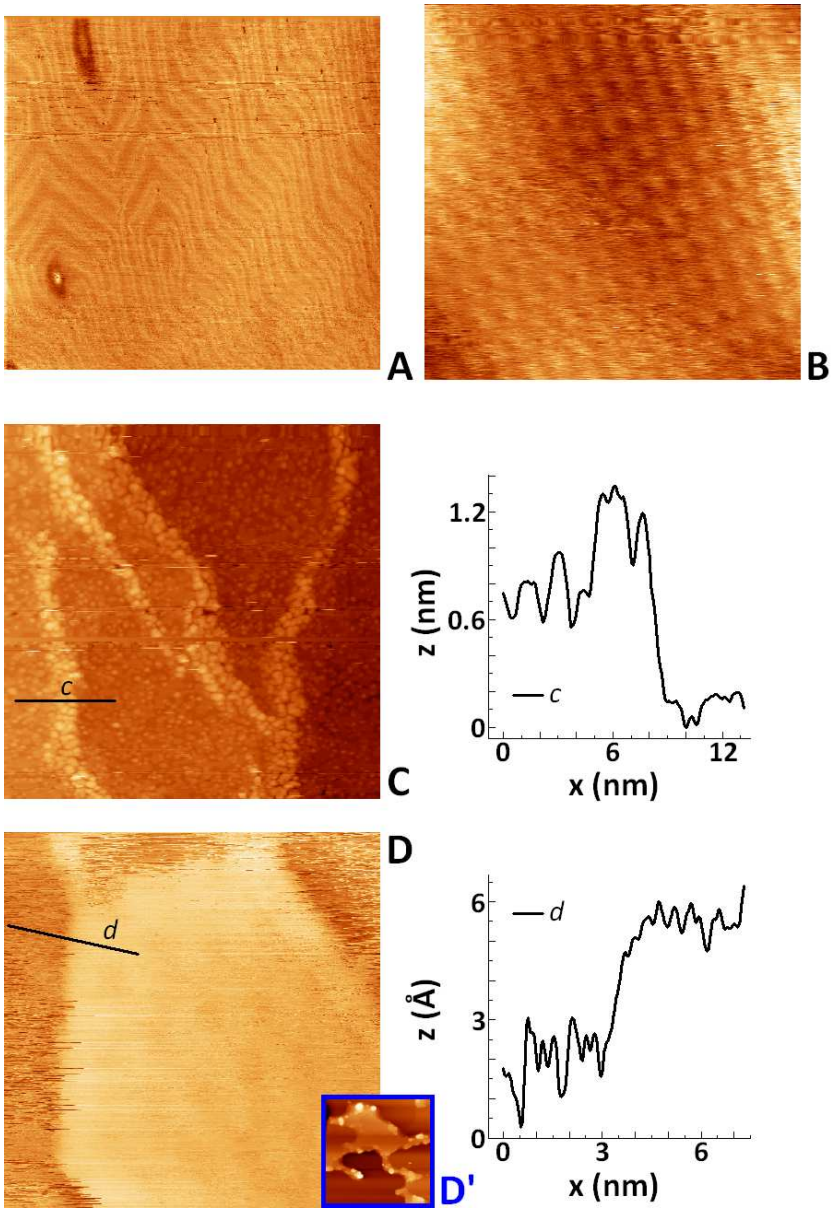

Figure 5.15: STM images obtained by ReactorSTM Mark II. (A) A 100 nm^2 STM image, showing a large terrace on Au(111), exhibiting the herringbone reconstruction. (B) A 2.5 nm^2 STM image of atomically resolved Au(111). (C) A 25 nm^2 STM image of Au(111) with > 1 monolayer of Mo deposited; c is the corresponding height profile. (D) A 10 nm^2 STM image of a MoS_2 crystallite on Au(111), with height profile d. Image D' is a 110 nm^2 subsection from a large scan, showing the accumulation of MoS_2 islands at the steps.

image, shown in figure 5.15 D', is a cut-out from a large scale image, showing that, all the MoS_2 crystallites are on the edges of the Au(111) terraces, and on the terraces themselves no nano-particles can be seen. Unfortunately, it has not been possible to continue with this experiment up to the moment of writing, after obtaining the series of STM images, including figure 5.15. This means that the aim of atomically resolving the MoS_2 crystallites, and of performing high-pressure experiments lie in the near future [163].

Although the focus of this study has only been on the unpromoted MoS_2 nano-crystallites, a few words should be included about the addition of the main promoters for MoS_2, cobalt and nickel. Adding cobalt or nickel to the catalyst, on its industrial support γ-alumina, the promoter can appear in three forms. Firstly, the promoter atoms can dissolve into the γ-alumina, and secondly, cobalt can form a stable sulphide, Co_8S_9, on top of the support. Neither of these forms are believed to influence the desulphurization reaction rate. The third form, in which cobalt or nickel atoms replace some of the molybdenum atoms in MoS_2, forming CoMoS or NiMoS, increases reactivity by an order of magnitude. It is believed that the promoter atoms, in this structure, do not affect the molybdenum edges; they do, however, replace the molybdenum atoms at the sulphur edges. The activation energy for the creation of a sulphur vacancy, in the case of a sulphur edge, in which the metal atoms are replaced by cobalt or nickel, is significantly lower than for the sulphur edge with molybdenum [140, 187, 188]. In future experiments, adding these promoters to the MoS_2 crystallites has been planned, to study their influence on the activity of the catalyst under realistic conditions.

5.5 Concluding remarks

In conclusion, two milestones have been achieved in this experiment, up to the moment of writing. Firstly, it has been possible to successfully deposit MoS_2 nano-crystallites onto a Au(111) support, both with the ReactorSTM Mark I and Mark II. Up to now, in both cases it has only been possible to characterize the crystallites by the Moiré pattern, generated due to the lattice mismatch between Au(111) and MoS_2. However, the ReactorSTM Mark II is capable of atomically resolving the Au(111) surface, which opens the possibility of also atomically resolving the crystallites. This would be impossible with the ReactorSTM Mark I. Secondly, the activity of the catalyst under high-pressure and high-temperature conditions has been shown, with the combination of a batch experiment and a control experiment, using the

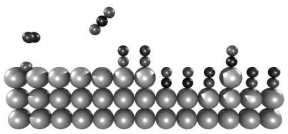

ReactorSTM Mark I. The microscope was also able to image the catalyst under these conditions, however with poor quality.

Further research is necessary, to investigate the behavior of the catalyst under high-pressure conditions, e.g. to determine which of the two edge terminations will be dominant, and what the role of each of the edges is, during various reaction steps. In a later stage, also the effect of the promoters cobalt and nickel should also be studied in the same fashion.

Appendix: Mo-Au alloying

At the first attempts at preparing molybdenum disulfide adatom islands on the (111) surface of gold, an unexpected, but easy to explain behavior was observed. Figure 5.16 shows a series of STM images, under different conditions. Image A and B are an example of what the STM images looked like, after the first MoS_2 deposition attempts. As can be seen, adatom island structures are present at the surface, which at first suggested the presence of MoS_2 on the surface. However, these surfaces were not stable, but began to behave like the series of STM images shown in figure 5.17. This figure shows four consecutive STM images A to D, each with a recording time of about 80 s. The markers I and II follow two evolving steps on the gold surface, throughout the imaging. As can be seen, these steps change drastically within the recording time of these four images, in total about five minutes, indicating a huge mobility of the steps on the gold surface. The density of adatom islands has significantly decreased, with respect to image A and B in figure 5.16; in the lower left hand corner of the images, some adatom island features still can be seen, which exhibit a larger stability than the steps on the gold surface. Apparently these are not MoS_2 crystallites (or at least stable ones) in image A and B of figure 5.16. There are a few indications supporting this hypothesis. Firstly, as the height profile a_2 on image A suggests, the apparent height of the adatom structures is 2 Å, which means these structures in this case actually *cannot* be MoS_2. This is because the bias voltage used to obtain this image, 80 mV, is well below the band gap of the semiconducting crystallites, in which case it should yield a very low apparent height for the crystallites, as in figure 5.12 A. The step height of the terraces, as indicated in the height profile a_1, is about 2.5 Å, which does seem to be different from the adatom structure's height. Next to the very irregular shapes of the adatom structures in image B, which according to the height profile b seem to exhibit the same step height as the terraces, vacancy islands can also be distinguished. As a reference, image C in figure

5.16 shows an STM image of one of the successful deposition experiments, exhibiting large MoS_2 crystallites, which are recognizable from their characteristic Moiré pattern. The step height of the Au(111) terrace here is 2.3 Å; the apparent height of the crystallites in this experiment were measured to be 2 Å, as shown in figures 5.12 and 5.14. Furthermore, in this case, no mobility of the Au(111) steps was observed. Image D in figure 5.16 shows the freshly prepared Au(111) surface, before Mo/H_2S exposure, in which the step height of the terraces again is 2.5 Å. In all these images, the step heights of the terraces correspond to a single step on Au(111). This is also the case for the steps in image A of figure 5.17, as shown in its corresponding height profile *a*. Finally, it should be mentioned that, in the situation of image A and B of figure 5.16, molybdenum, in combination with sulphur, (probably) was not deposited on the Au(111) surface. Whenever we observed the high step mobility, only a large series of sputtering and annealing cycles[9] would completely remove this mobile step behavior, returning to the initial situation of a clean Au(111) surface.

So since there has been material deposited on the gold surface, leading to a high step mobility, the question arises as to what mechanism is behind it. The literature reports the possibility of molybdenum alloying with gold. When molybdenum is deposited on gold, it forms clusters in the elbows of the herringbone reconstruction. This structure is stable up to a temperature of 600 K, above which gold encapsulates the molybdenum, forming Au-Mo-Au sandwiches on the surface. The same happens when molybdenum is deposited at a temperature above 525 K (one paper reports already having observed alloying at a deposition temperature of 300 K). When the alloying takes place, a large mobility of the steps on the gold surface has been observed. Once alloyed, exposure to atomic oxygen or sulfur can separate the metals, ending with molybdenum oxides or sulfides on top of the surface [189–191].

What has apparently been seen, in the early experiments here, is this alloying between the two metals, because the initially observed adatom islands (which could be just molybdenum, or molybdenum in combination with some sulphur), disappear; thereafter, huge step mobility on the gold surface was observed. There are two possible reasons for this alloying to occur in this case. In the initial deposition experiments, various parameters were being tuned, including H_2S pressure, molybdenum, and H_2S exposure time,

[9] On the order of ten cycles were needed to get rid of the step mobility. Molybdenum is hard to get rid of.

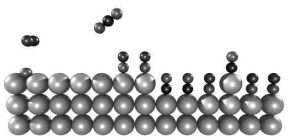

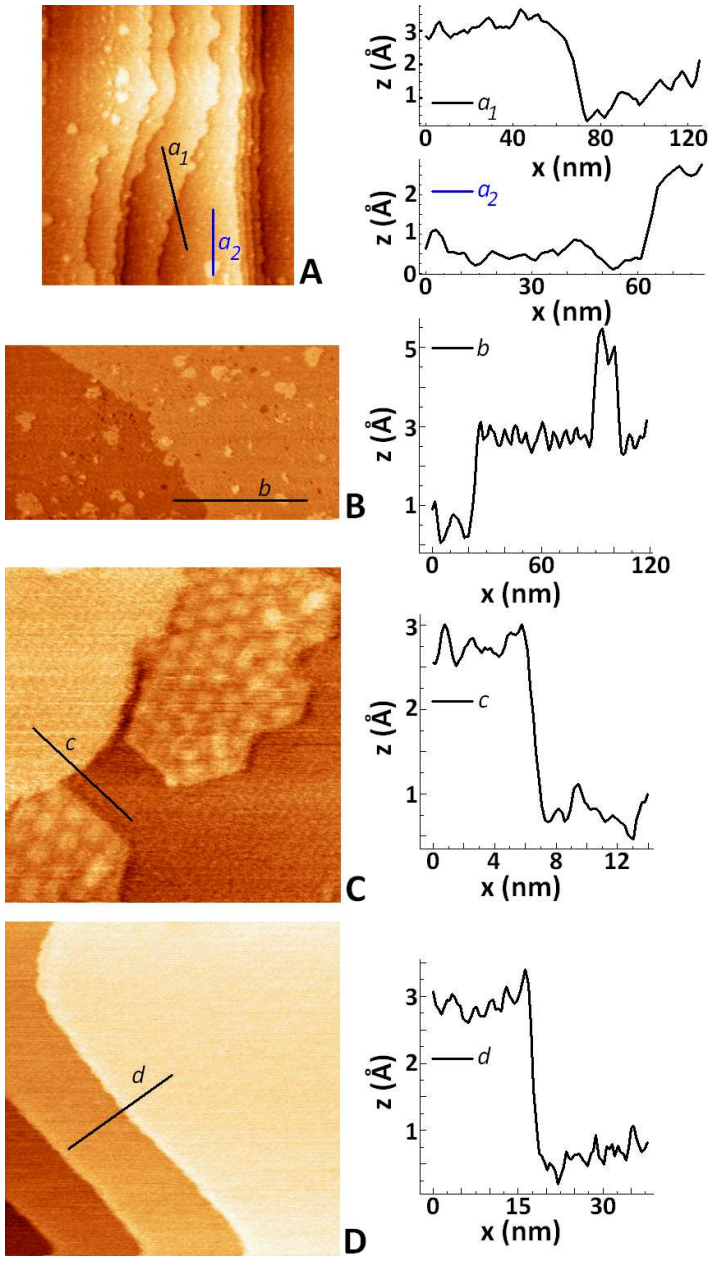

Figure 5.16: (A) A 300 x 335 nm^2 STM image, with height profiles a_1 and a_2, showing adatom island structures on Au(111); V_b = 80 mV; I_t = 0.2 nA. (B) A 300 x 155 nm^2 STM image, with height profile b; V_b = -2 V, I_t = 0.2 nA. (C) A 35 nm^2 STM image, with height profile c, showing MoS_2 on Au(111); V_b = -1.9 B, I_t = 0.15 nA. (D) A 100 nm^2 STM image of terraces on Au(111); V_b = 80 mV, I_t = 0.2 nA. T = 293 K.

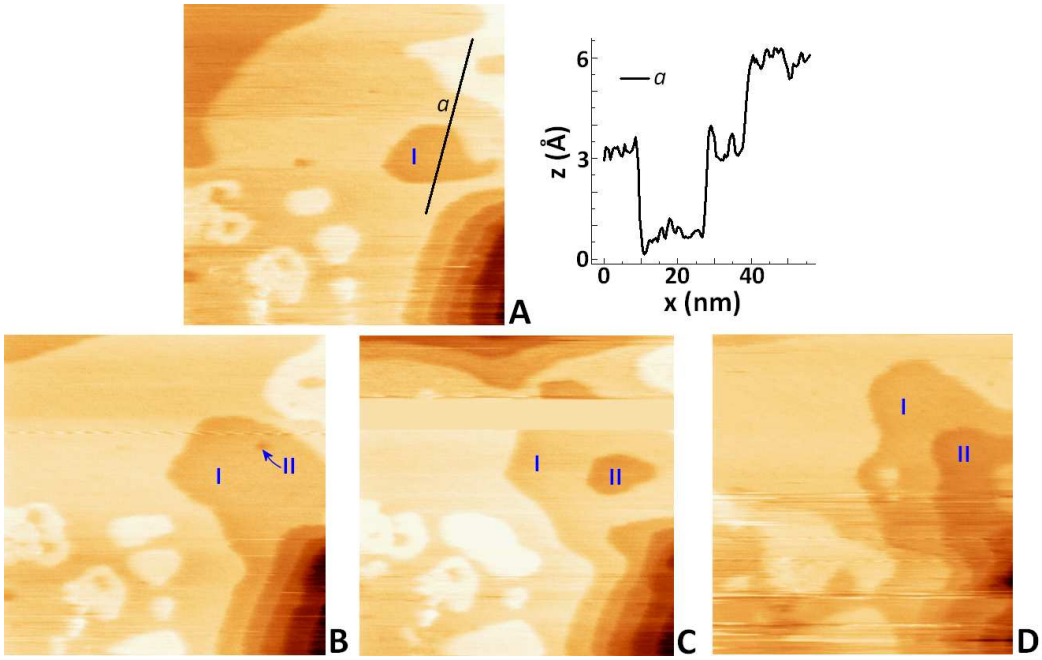

Figure 5.17: Four consecutive 100 x 100 nm^2 STM images (the recording time was ~80 s/image), showing large step mobility. The indicated terrace steps I and II have been followed. For image A, a corresponding height profile a is included. T = 393 K; V_b = -0.8 V; I_t = 0.2 nA.

and temperature. Under the "wrong" conditions this might lead to instable Mo/MoS_2 structures on the Au(111) surface, eventually leading to alloying of the two metals. However, there is one more factor present. When starting with the experiments involving thiophene, and still tweaking the parameters in the initial preparation steps, the alloying was no longer observed. This leaves a second option for destabilizing MoS_2 structures: the residual gases in the reactor, prior to thiophene exposure. The main residual gases in the reactor volume, before it was exposed to thiophene, were CO and H_2. CO does interact with MoS_2, but is not expected to destroy the islands [192]. H_2, on the other hand, reacts with the step edges, forming H_2S, which is part of the desulphurization reaction to be studied. With no organosulphur compounds present to fill these vacancies, hydrogen will proceed to react away all the sulfur, leaving bare molybdenum on gold, opening the possibility of alloying of the two metals.

Presumabely the interaction of the residual hydrogen in the reactor with the MoS_2 nano-particles is one of the key players in these experiments, in

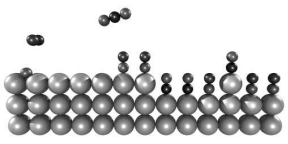

which the metals alloy. Initially, adatom islands are seen (of which, it should be said, their composition is not completely certain, due to the low bias voltage used to be able to image them, as in figure 5.16 A; it could be MoS_x, just Mo, or even Au already covering Mo). Later the fingerprint of alloying (the mobile steps) was observed. That the alloying did not take place directly, but only after an exposure of several hours in the reactor, could be explained by the fact that it takes hydrogen some time to react away all the sulfur – remember that the sample was at room temperature. Since molybdenum sulphides are stable on the gold surface, and sulphur is capable of de-alloying gold and molybdenum, a large fraction of the sulphur would have to be removed before alloying could begin. In addition, when thiophene was used, alloying was no longer observed. This could mean that when there is a steady supply of a sulphur containing carbohydrate, it fills up the vacancies created by the residual hydrogen, and the islands on the surface are stabilized. Once thiophene is in the reactor surroundings, it is very difficult to remove, and it continues to outgas. This means that, even when there is no external supply of thiophene, the remnants of the previous experiments are enough to counteract the destabilizing effect of hydrogen.

Chapter 6

Summaries and epilogue

6.1 Summary for the layman

The process of catalysis is a very important element in our modern society. From medicine to plastic bags: nowadays, almost everything encounters a catalyst at some point in its production process. A catalyst is a substance accelerating or selective to one specific chemical reaction, without being consumed itself. Most catalytic processes are heterogeneous: the catalyst is in a different phase, usually solid, than the reactants, which mostly are gaseous or liquid. In this case, the surface of the catalyst plays a decisive role in its activity, since the atoms of the bulk cannot be accessed by the reactants. Although the use of catalysts is widely spread, the most fundamental question about catalysts has not yet been answered in full extent: How does it work at the most elementary level, the level of atoms and molecules? If we can answer this question for a specific reaction on a specific catalyst, we will understand why it works better or worse under certain circumstances. Even more important is that this will possibly enable us to improve that catalyst. The research field, targeting the answer to this fundamental question, started blossoming over the last decennia. We are becoming more conscious of our impact on the environment, and one of the means to create a more sustainable and clean environment is the use of better catalysts.

The transport sector is one of the most important areas in which we try to control our impact on the environment. Sixteen percent of the global emission of CO_2 passes through the exhaust of a vehicle [193]. To minimize CO_2 emission, industry has been developing more economical combustion engines, while cars with hybrid engines and electro-motors are also being developed. Next to CO_2, however, the exhaust-gas composition consists of

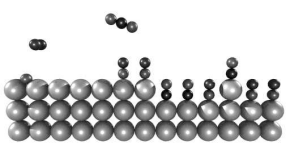

more hazardous gases, like carbon monoxide (CO), nitrogen oxides (NO_x), sulfur oxides (SO_x), and various unburned carbohydrates. The origin of these side products can be found in crude oil. Crude oil consists of organic remains, which naturally contain nitrogen and sulfur compounds. Next to the concentration of these compounds in the fuel that is combusted in the engine, other circumstances are important – the temperature of an engine is an important parameter in, for example, the amount of CO produced. The concentrations of hazardous gases in the exhaust gas are minimized in two ways. On the one side, the three-way catalyst in the exhaust of a vehicle processes CO, NO_x, and unburnt hydrocarbons to CO_2, N_2, and H_2O. On the other side, organic compounds containing nitrogen and sulphur can be industrially converted to clean hydrocarbons by catalytically activated denitrogenation and desulphurization, before fuel is distributed.

In this thesis I have studied three specific reactions from the petrochemical industry, and the three-way catalyst, at the atomic level: desulphurization of thiophene[1] on gold-supported molybdenum disulfide nano-particles, CO oxidation[2] and NO reduction[3] on platinum. To engage research at the atomic level, we have constructed a special microscope that is able to image the surface of a catalyst, under high pressure and temperature ("real reaction conditions"). By mimicking these conditions in the microscope, we can study the activity of a catalyst in its natural environment, as in the petrochemical industry and the vehicle exhaust. This is not the standard modus operandi in this field: many experimental techniques do not allow high pressures, but only operate in vacuum ($p < 10^{-8}$ bar), a discrepancy going by the name "pressure gap". But at very low pressures, a catalyst behaves quite differently!

The microscope we have built is a so-called scanning tunneling microscope, which is described in chapter 2. The concept of such a machine is to scan a surface (the sample), with an atomically sharp needle (the tip), in such a way that the tip "feels" the atoms on the surface; a macroscopic analogue is the blind man who feels with his cane (the tip) the bumpiness of the pavement (the sample). The microscope has been designed in such a way that we, on the one hand, can expose the sample to a flow of gas at pressures up to 10 bar (in a high-pressure cell, which we have called the "reactor"), and on the other hand, make use of an ultrahigh vacuum system, in order to

[1] An aromatic substance, in which one of the carbon atoms is replaced by a sulfur atom; it is frequently present in crude oil.

[2] $2CO+O_2 \rightarrow CO_2$, one of the reactions taking place in the three-way catalyst.

[3] $2NO+2CO \rightarrow N_2+2CO_2$, one of the reactions taking place in the three-way catalyst.

perform standard preparation and analysis techniques on the sample. The sample itself separates the reactor from the rest of the vacuum system, during an experiment, by being pressed onto a rubber seal. By means of a transfer system, we can move the sample from the reactor to any of the pieces of ultrahigh-vacuum instrumentation mounted on the chamber. A dedicated gas manifold allows us to expose the sample to a wide range of mixtures of up to four different gases, at separately controlled flows and pressures. To be able to correlate surface structure with reactivity, simultaneously with the microscope we operate a quadrupole mass spectrometer, which measures the gas composition in the reactor.

In our research on NO reduction, presented in chapter 3, we have shown that the surface reconstruction of Pt(100)[4] plays a significant role in the reactivity. This is based on our observation of a clear phase transition on the surface, in our STM images, when changing the gas composition, indicating the rearrangement of the platinum atoms in the outermost surface layer. The sites at the surface change from a square symmetry to a hexagonal symmetry, changing the properties of these sites. We believe that the reaction mechanism (Langmuir-Hinshelwood kinetics) on both of these phases is the same, since the surface remains metallic, but with different reaction constants. We have constructed a mathematical model, with which we have been able to fit the experimental data of the mass spectrometer. This model indicates that separating the reactivity data according to the surface phase transition, introducing two sets of fitting parameters, improves the quality of the fit with respect to a description where all data were fit with a single set of parameter values.

The oxidation of CO on Pt(110)[5], described in chapter 4, is the first system we have resolved atomically, under reaction conditions. Firstly, we were able to resolve the (1x2) missing-row reconstruction, atomically under vacuum. More importantly, we observed various surface structures, on the atomic level, under realistic conditions. Secondly, the formation of an oxide layer was observed, in combination with roughening of the surface, when we increased the oxygen pressure. Replacing the oxygen by CO, the surface switches back to a metallic phase, during which it smoothens. On the ox-

[4]Pt(abc) refers to a certain crystallographic orientation of the surface. The (100) surface undergoes a reconstruction, which means that the surface looks different from the rest of the crystal. The "(100) crystal" has a square lattice, whereas the atoms at the surface rearrange themselves into a hexagonal lattice.

[5]See last footnote. The (110) orientation also exhibits a reconstruction, in which every second row on the surface is absent: the (1x2) missing-row reconstruction.

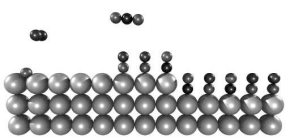

ide, the surface exhibits a different reaction mechanism (Mars-Van Krevelen kinetics) than on the metal (Langmuir-Hinshelwood kinetics). The activity of the catalyst is higher, when the surface of the catalyst is in the oxide phase. This is a result, which cannot be obtained under vacuum conditions, therefore emphasizing the importance of studying catalysts under realistic conditions.

Chapter 5, finally, describes the desulphurization of thiophene on molybdenum disulfide crystallites, supported on a gold (111)[6] crystal. At the time of writing of this thesis, we achieved two experimental milestones in this experiment. Firstly, we have been able to create and image MoS_2 crystallites on Au(111), both in the ReactorSTM Mark I[7] and the Mark II[8]. The imaging quality on the crystallites in the ReactorSTM Mark II still needs improvement, but since we were able to atomically resolve Au(111) with this machine, this should be a feasible goal. Secondly, we have observed reactivity of the crystallites in the ReactorSTM Mark I, by exposing the sample to a 1 bar mixture of thiophene (carried by argon) and hydrogen, which means we can activate the crystallites under realistic conditions. We were also able to image the crystallites under these conditions; however, the imaging quality of the ReactorSTM Mark I is too poor to do a proper morphology analysis on the crystallites, or to distinguish vacancy creation, or thiophene adsorption, on the crystallites. But the fact that we have been able to image the crystallites, under a high thiophene/hydrogen pressure in the Mark I, means we will be able to do the same in the Mark II, in which we should also be able to resolve the crystallites atomically.

6.2 Samenvatting voor de leek

Katalyse is niet meer weg te denken uit onze moderne maatschappij. Van medicijnen tot plastic zakjes: bijna alles heeft tegenwoordig wel ergens tijdens het productieproces met een katalysator te maken gehad. Een katalysator is een stof die selectief is voor één bepaalde chemische reactie of deze versnelt zonder daarbij zelf verbruikt te worden. De meeste katalytische processen zijn heterogeen: de katalysator bevindt zich in een andere fase, meestal vast,

[6]The (111) surface of gold reconstructs into a hexagonally close-packed "herringbone"-reconstruction.

[7]An already existing prototype of the ReactorSTM [53], which formed our basis for defining our requirements, in developing its successor. The Mark I has been briefly described at the end of Chapter 1.

[8]Successor of the Mark I; has been described in full detail in Chapter 2.

dan de reagerende stoffen, die meestal gasvormig of vloeibaar zijn. In dit geval speelt het *oppervlak* van de katalysator een doorslaggevende rol in de werking, aangezien de atomen van de katalysator *onder* het oppervlak niet toegankelijk zijn voor de gasvormige of vloeibare moleculen van de reagerende stoffen. Hoewel het gebruik van katalysatoren wijd verspreid is, is de meest fundamentele vraag over katalysatoren nog niet geheel beantwoord: Hoe werkt een katalysator op het meest elementaire niveau: het niveau van atomen en moleculen? Als we deze vraag voor een bepaalde reactie op een bepaalde katalysator kunnen beantwoorden, zijn we niet alleen in staat te begrijpen waarom de katalysator beter of slechter werkt onder verschillende omstandigheden, maar vooral ook om de katalysator mogelijk te verbeteren. Het wetenschappelijk vakgebied met als doel deze fundamentele vraag te beantwoorden, heeft de laatste decennia een grote vlucht genomen. Eén van de redenen hiervoor is dat we ons er steeds bewuster van worden dat wij als mens een grote invloed hebben op het klimaat van deze planeet; betere katalysatoren stellen ons in staat een duurzamere en schonere samenleving te creëren, hetgeen in de volgende paragraaf geïllustreerd wordt aan de hand van de transportwereld.

De transportwereld is één van de belangrijke gebieden waarin we proberen onze impact op het milieu te verminderen. Zestien procent van de wereldwijde uitstoot van CO_2 gaat via de uitlaat van een voertuig [193]. Om de uitstoot van CO_2 te minimaliseren, worden er steeds zuiniger verbrandingsmotoren gemaakt, waarnaast ook hybride en elektrische auto's ontwikkeld worden. In de uitlaatgassen van benzine- en dieselmotoren zitten naast CO_2 echter ook veel schadelijker stoffen, zoals koolstofmonoxide (CO), stikstofoxides (NO_x), zwaveloxides (SO_x) en verschillende koolwaterstoffen. De oorsprong van deze bijproducten ligt niet alleen in de verbranding zelf – de temperatuur van een verbrandingsmotor draagt sterk bij aan bijvoorbeeld de concentratie CO in de uitlaatgassen, maar ook in de aardolie. Aardolie is namelijk opgebouwd uit organische resten, waar van nature stikstof- en zwavelverbindingen inzitten. Om de concentratie van alle schadelijke stoffen in de uitlaatgassen te minimaliseren, wordt aan twee kanten actie ondernomen. Aan de ene kant zorgt een driewegkatalysator in de uitlaat van de verbrandingsmotor ervoor dat stoffen als CO, NO_x en onverbrande koolwaterstoffen omgezet worden in CO_2, N_2 en H_2O. Aan de andere kant worden organische stikstof- en zwavelverbindingen industrieel omgezet naar schone koolwaterstoffen door katalytische denitrogenering en ontzwaveling.

In dit proefschrift heb ik drie specifieke reacties uit de petrochemische industrie en de driewegkatalysator op atomair niveau bestudeerd: ontzwaveling

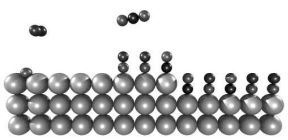

van thiofeen[9] op nanodeeltjes bestaande uit molybdeensulfide, CO oxidatie[10] en NO reductie[11] op platina. Om onderzoek hiervan op atomair niveau mogelijk te maken, hebben we een microscoop ontwikkeld die ons in staat stelt om onder hoge druk en hoge temperatuur ("reële reactieomstandigheden") het oppervlak van de katalysator te zien. Door deze omstandigheden na te bootsen in de microscoop, kunnen we de daadwerkelijke werking van de katalysator zien zoals die in de industrie en de uitlaat van een voertuig plaatsvindt. Dit is niet standaard in dit vakgebied: vele experimentele technieken laten geen reële reactieomstandigheden toe, maar werken slechts bij zeer lage druk ($p < 10^{-8}$ bar), een discrepantie die als het "pressure gap" door het leven gaat – bij zeer lage druk werkt een katalysator namelijk vaak heel anders dan onder realistische omstandigheden.

De microscoop die we gebouwd hebben is een zogenaamde rastertunnelmicroscoop, die beschreven wordt in hoofdstuk 2. Het concept hiervan is om met een atomair scherpe naald (de tip) over een oppervlak (het preparaat) heen te bewegen, zodat de tip de atomen op het oppervlak "voelt". Denk hierbij aan de manier waarop een blinde met zijn stok (de tip) de hobbels op de stoep (het preparaat) probeert te zien. Het ontwerp van de microscoop is zo, dat we aan de ene kant het preparaat aan een stroom gas van 1 – 10 bar kunnen blootstellen (in een hogedrukcel), en aan de andere kant gebruik maken van ultrahoog vacuüm (10^{-13} bar) om het preparaat zo goed mogelijk te kunnen prepareren. Het preparaat zelf scheidt via een rubberen afdichting de hogedrukcel van de rest van het systeem tijdens een experiment; met een transfersysteem kunnen we het preparaat verplaatsen van de hogedrukcel naar de verscheidene preparatie-apparaten die aan het vacuümsysteem hangen. Een speciaal ontworpen gassysteem stelt ons in staat om tijdens een experiment het preparaat bloot te stellen aan maximaal vier verschillende gassen op een onafhankelijk van elkaar ingestelde flow en druk. Om de structuur van het oppervlak te kunnen correleren met de reactiviteit, maken we gebruik van een massaspectrometer die de samenstelling van de gassen in de hogedrukcel meet. Massaspectrometer en microscoop meten gelijktijdig.

In ons onderzoek over de reductie van NO, gepresenteerd in hoofdstuk 3, hebben we laten zien dat de oppervlaktereconstructie van Pt(100)[12] een

[9]Een aromatische verbinding waarbij één van de koolstofatomen is vervangen door een zwavelatoom die veel voorkomt in ruwe aardolie.

[10]$2CO+O_2 \rightarrow CO_2$, één van de reacties in de driewegkatalysator.

[11]$2NO+2CO \rightarrow N_2+2CO_2$, één van de reacties in de driewegkatalysator.

[12]Pt(abc) refereert aan een bepaalde kristaloriëntatie van platina. Het (100) oppervlak heeft een zogenaamde oppervlaktereconstructie, hetgeen betekent dat het oppervlak er

rol speelt in de reactiviteit. Dit baseren we op onze waarneming van een duidelijke faseovergang bij het wisselen van de gassamenstelling, waarbij er alleen sprake is van herstructurering van platina-atomen op het oppervlak. De atomen aan het oppervlak, waaraan de gasmoleculen kunnen binden, schakelen tussen een vierkante en een zeshoekige symmetrie, hetgeen hun eigenschappen verandert. Wij denken dat het reactiemechanisme (Langmuir-Hinshelwood kinetiek) in beide gevallen hetzelfde is, aangezien het oppervlak metallisch blijft, echter wel met verschillende reactieconstanten. Hiervoor hebben we een wiskundig model opgesteld dat we hebben gefit aan de experimentele data van de massaspectrometer. Dit model suggereert dat het splitsen van de kinetiek van de reactie in twee sets fitparameters, één voor de vierkante symmetrie van het oppervlak, en één voor de hexagonale symmetrie, de kwaliteit van de fit verbetert ten opzichte van het gebruik van slechts één set parameters waarbij de veranderende oppervlaktesymmetrie buiten beschouwing wordt gelaten.

De oxidatie van CO op Pt(110)[13], zoals beschreven in hoofdstuk 4, is het eerste systeem dat we onder reële reactieomstandigheden atomair hebben opgelost. In eerste instantie hebben wij in vacuüm de zogenaamde missende-rij-reconstructie atomair op kunnen lossen. Belangrijker is, dat we onder realistische omstandigheden verschillende oppervlaktestructuren atomair hebben kunnen waarnemen. We hebben de vorming van een oxide waargenomen, wanneer we de zuurstofdruk boven een bepaald niveau brachten, hetgeen ook verruwing van het oppervlak tot gevolg had. Het oppervlak werd weer metallisch wanneer we het zuurstof vervingen door CO, en dit metallische oppervlak werd gaandeweg vlakker. Op het oxide is een ander reactiemechanisme actief dan op het metaal; de activiteit op het oxide is hoger. Dit effect is niet te zien wanneer de katalysator in vacuüm bestudeerd wordt, hetgeen benadrukt hoe belangrijk het is om katalysatoren te bestuderen onder realistische omstandigheden.

Hoofdstuk 5, ten slotte, beschrijft de ontzwaveling van thiofeen op molybdeendisulfidekristallen die op een goud (111)[14] oppervlak aangebracht zijn.

---

anders uitziet dan de rest van het kristal. Het "(100) kristal" van platina heeft een vierkant rooster, echter aan het oppervlak hergroeperen de atomen zich in een hexagonaal rooster.

[13]Zie vorige voetnoot. De (110) oriëntatie heeft ook een reconstructie, waarbij elke tweede rij atomen op het oppervlak ontbreekt: de missende-rij-reconstructie.

[14]Het goud (111) oppervlak reconstrueert in een dichtgepakt hexagonaal rooster genaamd "haringgraat reconstructie", omdat het patroon doet denken aan de graat van een haring.

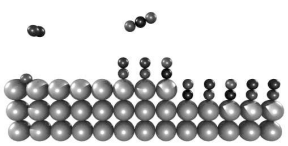

Op het moment van schrijven hebben we twee belangrijke mijlpalen behaald. In eerste instantie hebben we zowel in de ReactorSTM Mark I[15] als in de ReactorSTM Mark II[16] de MoS_2 kristallen kunnen creëren en zichtbaar kunnen maken. Met betrekking tot de kwaliteit van de STM plaatjes met de Mark II valt nog veel te winnen, maar aangezien we het goud (111) oppervlak atomair hebben kunnen oplossen, is het atomair oplossen van de nanokristallen een haalbaar doel. In tweede instantie hebben we in de Mark I de activiteit van de kristallen kunnen meten door ze bloot te stellen aan 1 bar thiofeen (met argon als draaggas) en waterstof. Onder deze omstandigheden waren we ook in staat om de kristallen te zien met de STM, echter is de kwaliteit van de STM plaatjes van de Mark I te laag om iets zinnigs te kunnen zeggen over de dynamica van de kristalvorm of het binden of verdwijnen van moleculen aan de randen van de kristallen. Echter het feit dat we onder de juiste omstandigheden met de Mark I hebben kunnen meten, heeft de weg geplaveid voor hetzelfde type metingen in de Mark II, waarmee we de kristallen onder realistische omstandigheden atomair zullen kunnen oplossen.

6.3 Epilogue

The process of obtaining a PhD is, in many ways, comparable to making a long journey. You start by taking a step into the unknown, knowing that all encounters, both positive and negative, will make you a richer person. The goal of the journey is the journey itself; there is not really a fixed plan, apart from the day at, and the place from, where your plane leaves to bring you home. On a journey, you meet lots of interesting people, from many cultures, who give you new insights, give directions, or make arrangements for you. Sometimes you experience unexpected delays, which can be annoyingly long, and sometimes you are surprised by the ease at which you do something, which you foresaw to be a hurdle. Not every road is flat and straight, but after every mountain pass and corner, there will be a new view or experience. When you take a wrong turn, you may have to go back, to get back on track, but sometimes a wrong turn can lead to an unexpected surprise. In the end, when you return home, you write a travel report, to help you to remember all the special moments and experiences. In your hands lies my travel report.

This work would never have taken its current shape without the technical,

[15] Een reeds bestaand prototype van de ReactorSTM [53], die de basis heeft gevormd voor onze voorwaarden voor de ontwikkeling van zijn opvolger. De Mark I is kort beschreven aan het einde van hoofdstuk 1.

[16] Opvolger van de Mark I, uitgebreid beschreven in hoofdstuk 2.

scientific, and social support of many people, who I gratefully acknowledge for their various contributions, and to whom I wish to dedicate this paragraph (all names in alphabetical order). From the ReactorSTM team, with whom I have been working closely: Johan Bakker, Marta Cañas-Ventura, Qian Liu, and Violeta Navarro-Paredes. From the Fine Mechanical Department: Mirthe Bergman, Arjen Geluk, Ewie de Kuyper, Peter van der Tuijn, Gregory Verdoes, and the others who have done an occasional job for the setup. From Leiden Probe Microscopy: Gertjan Van Baarle, and Alexei Ofitserov. From the Electronics Department: Bert Crama, Raymond Koehler, and René Overgauw. The (rest of the) interface physics group: Marcelo Ackermann, Dirk van Baarle, Jan-Willem Beenakker, Anne France Beker, Hans Borsboom, Guocai Dong, Vincent Fokkema, Elodie Fourré, Erwin Heeres, Allard Katan, Willem Onderwaater, Tjerk Oosterkamp, Richard van Rijn, Ellie van Rijsewijk, Sander Roobol, Marcel Rost, Johannes Simon, Merlijn van Spengen, Femke Tabak, Ivar Taminiau, Gerard Verbiest, Jan Verhoeven, Alexander Weisz, Geert Wijts, and Yuri Yanson. From the general staff: Wilfred van der Geest. From the past: Ştefania Bobaru, and Bas Hendriksen. From Albemarle Catalysts BV: Sonja Eijsbouts, Jelle Kampen, and Bart Nelissen. From Haldor Topsøe: Stig Helveg. The people within NIMIC. Ben Nieuwenhuys, with whom we had fruitful discussions about our results on NO reduction reactions. Roger Thiel, who corrected the English of this work. Family and friends, especially Ernst Dave Herbschleb, who helped me out with many of the programs I had to write. And last, but not least, my supervisor: Joost Frenken.

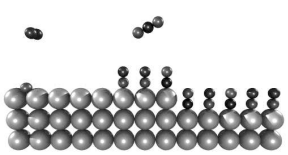

List of publications

1. *Catalytic activity of the Rh surface oxide: CO oxidation over Rh(111) under realistic conditions*; J. Gustafson, R. Westerström, O. Balmes, A. Resta, R. van Rijn, X. Torrelles, **C. T. Herbschleb**, J. W. M. Frenken, and E. Lundgren; J. Phys. Chem. C. **114**, 4580 (2010).

2. *Reply to "comment on 'Catalytic activity of the Rh Surface Oxide: CO Oxidation over Rh(111) under realistic conditions' "*; J. Gustafson, R. Westerström, O. Balmes, A. Resta, R. van Rijn, X. Torrelles, **C. T. Herbschleb**, J. W. M. Frenken, and E. Lundgren; J. Phys. Chem. C **114**, 22372 (2010).

3. *High-pressure STM study of NO reduction by CO on Pt(100)*; **C.T. Herbschleb**, S.C. Bobaru, and J.W.M. Frenken; Catalysis Today **154**, 61 (2010).

4. *High-Pressure STM for studying catalysis under industrial conditions*; **C.T. Herbschleb**, P.C. van der Tuijn, Q. Liu, G. Verdoes, M.E. Cañas-Ventura, L. Crama, D. Stoltz, J.W. Bakker, V. Navarro-Paredes, I. Taminiau, G.J.C. van Baarle, A. Ofitserov, M. Bergman, and J.W.M. Frenken; in preparation for submission to Rev. Sci. Instr.

5. *ReactorAFM; Ultrahigh vacuum/high-pressure flow reactor for atomic force microscopy studies close to conditions for industrial catalysis*; M. E. Cañas-Ventura, S. Roobol, W. Onderwaater, P.C. van der Tuijn, **C.T. Herbschleb**, Q. Liu, G. Verdoes, R. Koehler, D. Stoltz, J.W. Bakker, G.J.C. van Baarle, A. Ofitserov, V. Navarro-Paredes, I. Taminiau, M. Bergman, and J. W. M. Frenken; in preparation for submission to Rev. Sci. Instr.

6. *High-pressure STM study of hydro-desulphurization of thiophene on MoS_2/ Au(111)*; **C.T. Herbschleb**, Q. Liu, J.W. Bakker, B.J. Nelissen, S. Helveg, and J.W.M. Frenken; in preparation.

7. *Oxide versus Metal – Direct STM imaging of the surface oxide on Pt(110) during CO oxidation at atmospheric pressures*; **C.T. Herbschleb**, Q. Liu, V. Navarro-Paredes, J.W. Bakker, M.E. Cañas-Ventura, D. Stoltz, and J.W.M. Frenken; in preparation.

Curriculum Vitae

Cornelis Thaddeus Herbschleb is geboren op 1 november 1983 te Leeuwarden. Na het behalen van zijn gymnasium-diploma in juni 2001 begon hij zijn studie natuurkunde aan de Universiteit van Leiden, waar hij in juni 2006 zijn doctoraal diploma behaalde. Zijn eerste onderzoeksstage bestond aan de ene kant uit het construeren, plaatsen en beheren van kosmische stralingsdetecoren in Leiden en omgeving (alsmede in Khartoum) onder begeleiding van prof. dr. Pierre van Baal. Dit werk vond plaats in nauw contact met het Nederlands Instituut voor Kern en Hoge Energie Fysica. Aan de andere kant heeft hij tijdens deze onderzoeksstage een dergelijke stralingsdetector geïntegreerd met MiniGRAIL (Mini-Gravitational Radiation Antenna In Leiden) in de groep van prof. dr. Giorgio Frossati. De tweede onderzoeksstage vond plaats in de Interface Physics groep onder begeleiding van prof. dr. Joost Frenken en had betrekking op het onderzoek van de werking van katalysatoren met behulp van een hoge-druk STM. Hij vervolgde het werk aan deze opstelling tijdens zijn promotie, in dienst van de Interface Physics groep, verbonden aan de Universiteit Leiden. Hij heeft tijdens zijn promotie ook gewerkt aan de ontwikkeling van een nieuwe, sterk verbeterde versie van de ReactorSTM, waarin resolutie, robuustheid, drukbereik en gebruikersgemak een grote rol hebben gespeeld. Alsmede heeft hij de eerste succesvolle metingen met deze apparatuur verricht. Tijdens zijn promotie heeft hij deel uitgemaakt van NanoNed (www.nanoned.nl) en het SmartMix programma NIMIC (www.realnano.nl). Daarnaast is hij project coördinator geweest van EuroPhysicsFun, een Europees platform voor natuurkundeshows in Europa dat ondermeer jaarlijks het congres “Show Physics” organiseert.

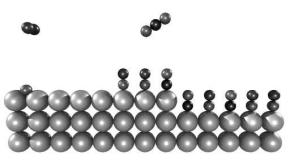

Bibliography

[1] J.J. Berzelius; Edinburgh New Philosophical Journal **21**, 223 (1836)

[2] Heterogeneous catalysis in industrial practice, 2nd ed.; C.N. Satterfield; McGraw-Hill, New York (1991)

[3] Encyclopedia of chemical technology volume 1, 3rd ed.; H.F. Mark et al.; John Wiley & Sons (1978)

[4] http://nobelprize.org/nobel_prizes/chemistry/laureates /2007/

[5] The Basis and Applications of heterogeneous catalysis; M. Bowker; Oxford Chemistry Primers (1998)

[6] Introduction to Surface Chemistry and Catalysis; G.A. Somorjai; Wiley, New York (1993)

[7] Otto Roelen, pioneer in industrial homogeneous catalysis; B. Cornils et al.; Angewandte Chemie International Edition **33**, 2144 (1994)

[8] http://www.chemguide.co.uk/physical/catalysis/ introduction.html

[9] Automobiles and pollution; P. Degobert; Éditions Technip. (1992)

[10] Surface studies by scanning tunneling microscopy; G. Binnig et al.; Phys. Rev. Lett. **49**, 57 (1982)

[11] Introduction to scanning tunneling microscopy; C. Chen; Oxford series in optical and imaging sciences (1993)

[12] Atomic-scale study of a hydrodesulfurization model catalyst; J.V. Lauritsen; PhD thesis, University of Århus (2002)

[13] Scanning tunneling microscopy; J.A. Stroscio and W. Kaiser; Academic Press, San Diego (1993)

[14] Growth mechanisms of epitaxial metallic oxide $SrRuO_3$ thin films studied by scanning tunneling microscopy; R.A. Rao et al.; Appl. Phys. Lett **71**, 1171 (1997)

[15] Epitaxial growth of thin magnetic cobalt films on Au(111) studied by scanning tunneling microscopy; B. Voigtländer et al.; Phys. Rev. B **44**, 10354 (1991)

[16] Grains, growth, and grooving; M.J. Rost et al.; Phys. Rev. Lett. **91**, 026101 (2003)

[17] Current-Voltage characteristics of self-assembled monolayers by scanning tunneling microscopy; S. Datta et al.; Phys. Rev. Lett. **79**, 2530 (1997)

[18] Boron nitride nanomesh; M. Corso et al.; Science **303**, 217 (2004)

[19] High-resolution scanning tunneling microscopy imaging of mesoscopic graphene sheets on an insulating surface; E. Stolyarova et al.; Proceedings of the Nat. Acad. of Sci. of the USA **104**, 9209 (2007)

[20] Electrochemical STM observation of $[Fe(CN)_6]^{3-}$ ions adsorbed on a hydrotalcite crystal surface; K. Yao et al.; Journ. Electroanalytical Chem. **458**, 249 (1998)

[21] Electrochemical STM investigation of 1,8-octanedithiol monolayers on Au(111): Experimental and theoretical study; M.J. Esplandiu et al.; Surf. Sci. **600**, 155 (2006)

[22] High temperature electrochemical scanning tunneling microscope instrument; A. Shkurankov et al.; Rev. Sci. Instr. **73**, 102 (2002)

[23] New model catalysts (platinum nanoparticles) and new techniques (SFG and STM) for studies of reaction intermediates and surface restructuring at high pressures during catalytic reactions; G.A. Somorjai; Appl. Surf. Sci. **121 - 122**, 1 (1997)

[24] Surface Science, an introduction; J.B. Hudson; John Wiley & Sons, Inc. (1998)

[25] Eley-Rideal type mechanism for Formate Synthesis on a Cu(III) surface; J. Ogawa et al.; Nippon Kagakkai Koen Yokoshu **81**, 270 (2002)

[26] Oxidations carried out by means of vanadium oxide catalysts; P. Mars, and D.W. Van Krevelen, Spec. Suppl. te Chem. Eng. Sci. **3**, 41 (1954)

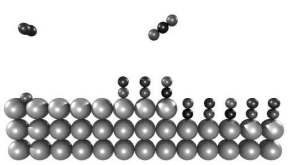

[27] CO Oxidation on Pt(110): Scanning Tunneling Microscopy Inside a High-Pressure Flow Reactor; B.L.M. Hendriksen, and J.W.M Frenken, Phys. Rev. Lett. **89**, 046101 (2002)

[28] The role of steps in surface catalysis and reaction oscillations; B.L.M. Hendriksen et al.; Nature Chemistry **2**, 730 (2010)

[29] CO oxidation at Pd(100): a first-principles constrained thermodynamics study; J. Rogal et al.; Phys. Rev. B **75**, 205433 (2007)

[30] CO oxidation on Pd(100) at technologically relevant pressure conditions: First-principles kinetic Monte Carlo study; J. Rogal et al.; Phys. Rev. B **77**, 155410 (2008)

[31] Catalysis of gold nanoparticles deposited on metal oxides; M. Haruta; Cattech **6**, 102 (2002)

[32] On the origin of the catalytic activity of gold nanoparticles for low-temperature CO oxidation; N. Lopez et al.; J. of Cat. **223**, 232 (2004)

[33] Steuern Größenquantisierungseffekte die CO adsorption auf Au-Nanopartikeln?; C. Lemire et al.; Angew. Chem., 118 (2003)

[34] CO Oxidation on Pt-Group Metals from Ultrahigh Vacuum to Near Atmospheric Pressures. 1. Rhodium; F. Gao et al.; Journ. Phys. Chem. C **2009**, 182 (2009)

[35] Highly active surfaces for CO oxidation on Rh, Pd, and Pt; M.S. Chen et al.; Surf. Sci. **601**, 5326 (2007)

[36] Structure and Reactivity of Surface Oxides on Pt(110) during Catalytic CO Oxidation; M.D. Ackermann et al.; Phys. Rev. Lett **95**, 255505 (2005)

[37] Solid state physics; J.R. Hook and H.E. Hall; J. Wiley and sons (2003)

[38] Chemistry of the elements (2nd ed.); N.N. Greenwood and A. Earnshaw; Butterworth-Heinemann (1997)

[39] Surface science – an introduction; K. Oura et al.; Springer-Verlag Berlin (2003)

[40] Common origin for surface reconstruction and the formation of chains of metal atoms; R.H.M. Smit et al.; Phys. Rev. Lett 87, 266102 (2001)

[41] Relativistic effects in structural chemistry; P. Pyykkö; Chem. Rev. **88**, 563 (1988)

[42] First-principles calculations of equilibrium ground-state properties of Au and Ag; N. Takeuchi et al.; Phys. Rev. B **40**, 1565 (1989)

[43] Reconstruction mechanism of fcc transition-metal (001) surfaces; V. Fiorentini et al.; arXiv-cond.mat, May 24 (1993)

[44] Energy minimization methods in computer vision and pattern recognition; A.K. Jain et al. (editors); (Springer, 2001)

[45] High-Pressure XPS of Pd model hydrogenation catalysts; D. Teschner et al.; J. Cat. **230**, 186 (2005)

[46] A differentially pumped electrostatic lens system for photoemission studies in the millibar range; D. Ogletree et al.; Rev. Sci. Instr, **73**, 3872 (2002)

[47] Xingcai Su, P. S. Cremer, Y. Ron Shen, and G.A. Somorjai, J. Am. Chem. Soc. **1997**, 119, 3994 (1997)

[48] Oxidation of Pd(553): From ultrahigh vacuum to atmospheric pressure; R. Westerström et al.; Phys. Rev. B **76**, 155410 (2007)

[49] Catalytic CO oxidation over ruthenium bridging the pressure gap; H. Over et al.; Progress in Surf. Sci. **72**, 3 (2003)

[50] A high pressure, high temperature, scanning tunneling microscope for in situ studies of catalysts; B.L. Weeks et al.; Rev. Sci. Instr. **71**, 10, 3777 (2000)

[51] Atomic-scale electron microscopy at ambient pressure; J.F. Creemer et al.; Ultramicroscopy **108**, 9, 993 (2008)

[52] Ultrahigh vacuum/high-pressure flow reactor for surface X-ray diffraction and grazing incidence small angle X-ray scattering studies close to conditions for industrial catalysis; R. van Rijn et al.; Rev. Sci. Instr **81**, 014101 (2010)

[53] The "Reactor STM": A scanning tunneling microscope for investigation of catalytic surfaces at semi-industrial reaction conditions; P.B. Rasmussen et al.; Rev. Sci. Instr. **69**, 3879 (1998)

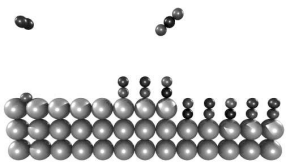

[54] A new scanning tunneling microscope reactor used for high-pressure and high-temperature catalysis studies; F. Tao et al.; Rev. Sci Instr **79**, 084101 (2008)

[55] ReactorAFM: Ultrahigh vacuum/high-pressure flow reactor for atomic force microscopy studies close to conditions for industrial catalysis; M.E. Cañas-Ventura et al.; in preparation for submission to Rev. Sci. Instr.

[56] Introduction to Scanning Tunneling Microscopy; C. J. Chen Oxford University Press (1993)

[57] www.realnano.nl

[58] High-pressure STM study of NO reduction by CO on Pt(100); C.T. Herbschleb et al.; Cat. Today **154**, 61 (2010)

[59] Kinetics and selectivity of the FischerTropsch synthesis: A literature review; G.P. van der Laan et al; Catal. Rev. **41**, 255 (1999)

[60] An overview of hydrodesulfurization and hydrodenitrogenation; I. Mochida et al.; Journal of the Japan Petroleum Institute **47**, 3 (2004)

[61] VG Scienta (www.vgscienta.com)

[62] UHV gate valve series 10, VAT (www.vatvalve.com)

[63] Valcon 75 plus, starcell 150/300, Varian (www.varian.com)

[64] Turbomolucular pump TPH 261PC in combination with DUO 20 MC, Pfeiffer (www.pfeiffer-vacuum.com)

[65] Hemi Heating, custom made (www.hemiheating.se)

[66] XPS Phoibos, SPECS (www.specs.de)

[67] Model IG35/70, OCI Vacuum Micro-engineering (www.ocivm.com)

[68] Mini e-beam evaporator EGCO4, Oxford Applied Research (www.oaresearch.co.uk)

[69] SpectaLEED 4 grid optics with Auger, Omicron (www.omicron.de)

[70] Vibration Control System, Newport (www.newport.com)

[71] Custom part, ERIKS (www.eriks.com)

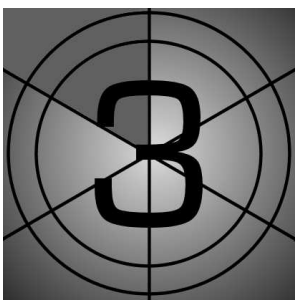

[72] Zerodur (thermal expansion $\sim 0.02 \cdot 10^{-6}$ mK^{-1}), Louwers (www.louwers.nl)

[73] SmCo magnet, IBS Magnet (www.ibsmagnet.com)

[74] EBL2, Boston Piezo Optics (www.bostonpiezooptics.com)

[75] Electronics, Leiden Probe Microscopy (www.leidenprobemicroscopy.com)

[76] Controlling chemical turbulence by global delayed feedback: Pattern formation in catalytic CO oxidation; M. Kim et al.; Science **292**, 1357 (2001)

[77] Microfacetting of a Pt(110) surface during catalytic CO oxidation; S. Ladal et al.; Surf. Sci. **197**, 153 (1988)

[78] CO oxidation on a Pt(110) single crystal surface; H.P. Bonzel et al.; J. Vac. Sci. and Tech. **9**, 663 (1972)

[79] Mechanisms of the catalytic CO oxidation on Pt(110); H.P. Bonzel et al.; Surf. Sci. **33**, 91 (1972)

[80] Subsurface oxygen in the CO-oxidation on Pt(110): Experiment and modeling of pattern formation; A. van Oertzen et al.; J. Phys. Chem B **102**, 4966 (1998)

[81] Kinetic oscillations and facetting during the catalytic CO oxidation on Pt(110); S. Ladas et al.; Surf. Sci. **198**, 42 (1988)

[82] Calorimetric measurement of catalytic surface reaction heat: CO oxidation on Pt(110); C.E. Wartnaby et al.; J. Chem. Phys. **102**, 1855 (1995)

[83] I. Taminiau; Master's thesis, Leiden University (2009)

[84] EL-flow and EL-press series, Bronkhorst (www.bronkhorst.com)

[85] Basisboek Vacuümtechniek; E.P.Th.M. Schuurmeijer et al.; NEVAC (2000)

[86] 37. T-W. Hui, www.chembio.uoguelph.ca

[87] CRC Handbook of Chemistry and Physics, Lide, 88th edition (2007-2008)

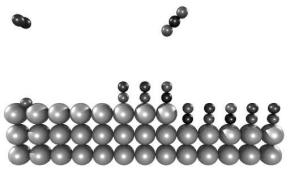

[88] MEMS-based high-speed scanning probe microscopy; E.C.M. Disseldorp et al.; Rev. Sci. Instr. **81**, 043702 (2010)

[89] Relaxations in the missing-row structure of the (1x2) reconstructed surfaces of Au(110) and Pt(110); E. Vlieg et al.; Surf. Sci. **233**, 248 (1990)

[90] Surface diffusion potential energy surfaces from first principles: CO chemisorbed on Pt(110); Q. Ge et al.; Journ. Of Chem. Phys. **111**, 9461 (1999)

[91] Nitric oxide catalysis in automotive exhaust systems; K.C. Taylor; Catal. Rev. **35**, 457 (1993)

[92] Automobile exhaust catalysts; R.M. Heck et al.; Applied Catalysis **221**, 443 (2001)

[93] Catalytic removal of NO; V.I. Pârvulescu et al.; Cat. Today **46**, 233 (1998)

[94] The surface science approach toward understanding automoyive exhaust conversion catalysis at the atomic level; B.E. Nieuwenhuys; Advances in Catalysis **44**, 259 (2000)

[95] The NO+CO reaction on Pt(100); M.W. Lesley et al.; Surf. Sc. **155**, 215 (1985)

[96] A TPD study of NO decomposition on Pt(100), Pt(411) and Pt(211); J.M. Gohndrome et al.; Surf. Sci. **209**, 44 (1989)

[97] Surface restructuring dynamics in CO adsorption, desorption and reaction with NO on Pt(100); A. Hopkinson et al.; Chem. Phys. **177**, 433 (1993)

[98] Bifurcation analysis of the three-variable model for the NO+CO reaction on Pt surfaces; R. Imbihl et al.; J. Chem. Phys. **96**, 6236 (1992)

[99] Energetics and kinetics of CO and NO adsorption on Pt(100): restructuring and lateral interactions; Y.Y. Yeo et al.; J. Chem. Phys. **104**, 3810 (1996)

[100] The temperature dependence of the interaction of NO+CO on Pt(100); J.H. Miners et al.; Surf. Sci. **547**, 355 (2003)

[101] Defects on the Pt(100) surface and their influence on surface reactions – A scanning tunneling microscopy study; W. Hösler et al.; IBM J. Res. Develop. **30**, 403 (1986)

[102] Direct observation of a nucleation and growth process on an atomic scale; E. Ritter et al.; Surf. Sci. **181**, 403 (1987)

[103] Synchrotron XPS and desorption study of the NO chemistry on a stepped Pt surface; C.J. Weststrate et al.; Surf. Sci. **600**, 1991 (2006)

[104] NO reduction by CO over automotive exhaust gas catalysts in the presence of O_2; J.M.A. Harmsen et al.; Cat. Lett. **71**, 81 (2001)

[105] 3D atom probe study of gas adsorption and reaction on alloy catalyst surfaces II: results on Pt and Pt-Rh; P.A.J. Bagot; Surf. Sci. **601**, 2245 (2007)

[106] An experimental test of various models of the active site for NO Reduction on Platinum; R.I. Masel; Cat. Rev. **28**, 335 (1986)

[107] The mechanism of the explosive NO + CO reaction on Pt(100): experiments and mathematical modelling; T. Fink et al.; Surf. Sci. **245**, 96 (1991)

[108] Lattice-gas model mimicking the NO+CO reaction on Pt(100); B. Meng et al.; J. Chem. Phys. **101**, 3234 (1994)

[109] Delay-induced chaos in catalytic surface reactions: NO reduction on Pt(100); N. Khrustova et al.; Phys. Rev. Lett. **75**, 3564 (1995)

[110] NO reduction by CO on a PT(100) surface – a DFT study; A. Eichler et al.; Journal of Catalysis **204**, 118 (2001)

[111] Study of oscillations and pattern formation in the NO+CO reaction on Pt(100) surfaces through dynamic Monte Carlo simulation: Toward a realistic model; S.J. Alas et al.; J. Phys. Chem B **110**, 9499 (2006)

[112] High pressure STM studies of oxidation catalysis; S.C. bobaru; Thesis, Leiden University (2006)

[113] High pressure STM studies of CO + O_2 on Pt(100); S.C. Bobaru et al.; In preparation

[114] Mechanism and dynamics of the CO-induced lifting of the Pt(100) surface reconstruction; P. van Beurden et al.; Phys. Rev. Lett. **90**, 066106 (2003)

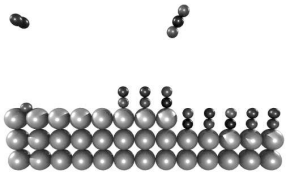

[115] Kinetic oscillations in the NO+CO reaction on Pt(100): Experiments and mathematical modeling; T. Fink et al.; J. Chem. Phys. **95**, 2109 (1991)

[116] The superstructures of the clean Pt(100) and Ir(100) surfaces; P. Heilmann et al.; Surf. Sci. **83**, 487 (1979)

[117] The effect of the surface structure of Pt on its electronic properties and the adsorption of CO, O_2 and H_2: a comparison of Pt(100)-(5x20) and Pt(100)-(1x1); C.R. Helms et al.; J. Chem. Phys. **65**, 1773 (1976)

[118] Density functional theory (DFT) and microcalorimetric investigations of CO adsorption on Pt clusters; R.M. Watwe et al.; Cat. Lett. **51**, 139 (1998)

[119] Direct observation of a nucleation and growth process on an atomic scale; E. Ritter et al.; Surf. Sci. **181**, 403 (1987)

[120] Homoepitaxial growth of Pt on Pt(100)-hex: effects of strongly anisotropic diffusion and finite island sizes; T.R. Linderoth et al.; Phys. Rev. Lett. **77**, 87 (1996)

[121] STM studies of clean, CO and O_2-exposed Pt(100)-hex-R0.7^o; A. Borg et al.; Surf. Sci. **306**, 10 (1994)

[122] Program LH-fits; EK studios (2008)

[123] Data reduction and error analysis for the physical sciences; P.R. Bevington et al.; McGraw-Hill (1992)

[124] Model catalysts in action; B.L.M. Hendriksen; PhD thesis, University of Leiden (2003)

[125] Operando SXRD: a new view on catalysis; M.D. Ackermann; PhD thesis, University of Leiden and ESRF Grenoble (2007)

[126] Direct observations of the (1x2) surface reconstruction on the Pt(110) plane; G.L. Kellogg; Phys. Rev. Lett. **55**, 2168 (1985)

[127] Adsorption-induced step formation; P.Thostrup et al.; Phys. Rev. Lett. **87**, 126102 (2001)

[128] An STM investigation of the structure of the Pt(110) and Au(110) surfaces; T. Gritsch et al.; Surf. Sci. **257**, 297 (1991)

[129] Strong bonding of single C_{60} molecules to (1x2)-Pt(110): an STM/DFT investigation; M. Casarin et al.; J. Phys. Chem. **2007**, 9365 (2007)

[130] Shape and decay of 2 and 3 dimensional islands on Au(110); M.J. Rost et al.; Surf. Sci. **515**, 344 (2002)

[131] Shape and evolution of vacancy islands on a MRR surface: Au(110); M.J. Rost et al.; Surf. Sci. **518**, 21 (2002)

[132] Regulation (EC) No 715/2007 of the European parliament and of the council; Official Journal of the European Union, L 171/1 (2007)

[133] The chemistry and technilogy of petroleum; J.G. Speight; Marcel Dekker (1999)

[134] Present state of the art and future challenges in the hydrodesulphurization of polyaromatic sulfur compounds; D.D. Whitehurst et al.; Adv. in Cat. **42**, 345 (1998)

[135] Advances in deep desulphurization; H. Topsøe et al.; Studies in Surf. Sci. and Cat. **121**, 13 (1999)

[136] The international crude oil market handbook; Energy Intelligence Group (2004)

[137] US Energy Information Administration; http://tonto.eia.doe.gov

[138] Genesis Group; http://www.genesisny.net

[139] Petroleum refining technology and economics; J.H. Gary et al.; Marcel Dekker (1984)

[140] Hydrotreating catalysis, science and technology, vol. 11; H. Topsøe et al.; Springer Verlag Berlin (1996)

[141] Hydrotreating model catalysts: from characterization to kinetics; L. Coulier; PhD Thesis, Eindhoven technical university (TuE) (2001)

[142] Correlating structure and reactivity: MoS_2 nanoparticles for hydrogen evolution; K.P. Jørgensen; PhD thesis, Technical university of Denmark (2007)

[143] Atomic-scale study of a hydrodesulfurization model catalyst; J.V. Lauritsen; PhD thesis, Århus univesity (2002)

[144] EU environmental laws impact fuels' requirements; S.F. Venner et al.; Hydrocarbon Processing **79** (2000)

[145] Scanning tunneling microscopy studies on model systems relevant for heterogeneous catalysis; S. Helveg; PhD thesis, Århus university (2000)

[146] Private communication with Sonja Eijsbouts, Albemarle Catalysts BV

[147] Hydrodesulfurization catalysis by transition metal surfaces; T.A. Pecoraro et al.; Journ. of Cat. **67**, 430 (1981)

[148] The adsorption and binding of thiophene, butene, and H_2S on the basal plane of MoS_2 single crystals; M. Salmeron et al.; Chem. Phys. Lett. **90**, 105 (1982)

[149] Scanning tunneling microscopy investigations of cluster sizes of molybdenum-based catalysts on graphite; H. Permana et al.; Cat. Lett. **24**, 363 (1994)

[150] Interpretation of STM images: the MoS_2 surface; A. Altibelli et al.; Surf. Sci. **367**, 209 (1996)

[151] Mobile promoters on anisotropic catalysts: nickel in MoS_2; J.G. Kushmerick et al.; J. Phys. Chem. B **102**, 10094 (1998)

[152] Atomic-scale structure of single-layer MoS_2 nanoclusters; S. Helveg et al.; Phys. Rev. Lett. **84**, 951 (2000)

[153] Hydrodesulfurization reaction pathways on MoS_2 nanoclusters revealed by scanning tunneling microscopy; J.V. Lauritsen et al.; Journ. of Cat. **224**, 94 (2004)

[154] Identification of active edge sites for electrochemical H_2 evolution from MoS_2 nanocatalysts; T.F. Jaramillo et al.; Science **317**, 100 (2007)

[155] Structure-function relations in molybdenum sulfide catalysts: the "rim-edge" model; M. Daage et al.; Journ. of Cat. **149**, 414 (1994)

[156] The relation between morphology and hydrotreating activity for supported MoS_2 paritcles; E.J.M. Hensen; Journ. of Cat. **199**, 224 (2001)

[157] Adsorption of thiophene on the catalytically active surface of MoS_2: an ab initio local-density-functional study; P. Raybaud et al.; Phys. Rev. Lett. **80**, 1481 (1998)

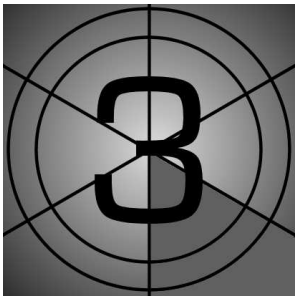

[158] Edge termination of MoS_2 and CoMoS catalyst particles; L.S. Byskov et al.; Cat. Lett. **64**, 95 (2000)

[159] One-dimensional metallic edge states in MoS_2; M.V. Bollinger et al.; Phys. Rev. Lett. **87**, 196803 (2001)

[160] Ab-initio study of the H_2-H_2S/MoS_2 gas-solid interface: the nature of the catalytically active sites; P. Raybaud et al.; Journ. of Cat. **189**, 129 (2000)

[161] Scanning tunneling microscopy observations on the reconstructed Au(111) surface: atomic structure, long-range super structure, rotational domains, and surface defects; J.V. Barth et al.; Phys. Rev. B **42**, 9307 (1990)

[162] Theory of surface stress and surface reconstruction; R.J. Needs et al.; Surf. Sci. **242**, 215 (1991)

[163] Q. Liu et al.; in preparation

[164] Shape and edge sites modifications of MoS_2 catalytic nanoparticles induced by working conditions: a theoretical study; H. Schweiger et al.; Journ. of Cat. **207**, 76 (2002)

[165] Vacancy formation on MoS_2 hydrodesulfurization catalyst: DFT study of the mechanism; J-F. Paul et al.; J. Phys. Chem. B **107**, 4057 (2003)

[166] Electronic structure and scanning-tunneling-microscopy image of molybdenum dichalcogenide surfaces; K. Kobayashi et al.; Phys. Rev. B **51**, 17085 (1995)

[167] Quartz Microbalance, Inficon (www.inficon.com)

[168] RC6 Chemical resistant pump, Vacuubrand (www.vacuubrand.com)

[169] Firerod Cartridge heater; 3 mm diameter, 3 cm long. Watlow bv. (www.watlow.com)

[170] Imaging and modification of Au(111) monatomic steps with atomic force microscopy; C.A. Goss et al.; Langmuir **1993**, 2986 (1993)

[171] Structure and function of the catalyst and the promoter in Co-Mo hydrodesulphurization catalysts; R. Prins et al.; Cat. Rev.-Sci. Eng. **31**, 1 (1989)

[172] Spectroscopy in catalysis; J.W. Niemantsverdriet; 2nd ed (Wiley-VCH Verlag GmbH, Weinheim, 2000)

[173] Genesis, architecture and nature of Co(Ni)-MoS_2 supported hydroprocessing catalysts; J. Grimblot; Cat. Tod. **41**, 111 (1998)

[174] Hydrodesulphurization and hydrogenation; T.K. Qian (Wiley New York, 1999)

[175] Size-dependent structure of MoS_2 nanocrystals; J.V. Lauritsen et al.; Nature Nanotechnology **2**, 53 (2007)

[176] The hydrogenation and direct desulphurization reaction pathway in thiophene hydrodesulphurization over MoS_2 catalysts at realistic conditions: a density functional theory study; P.G. Moses et al.; Journ. Cat **248**, 188 (2007)

[177] Recent STM, DFT and HAADF-STEM studies of sulphide-based hydrotreating catalysts: insight into mechanistic, structural and particle size effects; F. Besenbacher et al.; Cat. Today **130**, 86 (2008)

[178] D. Costa et al.; Edge wetting effects of γ-Al_2O_3 and analase-TiO_2 supports by MoS_2 and CoMoS active phase: A DFT study; J. Cat. **246**, 325 (2007)

[179] Reactivities in deep catalytic hydrodesulfurization: challenges, opportunities, and the importance of 4-methyldibenzothiophene and 4, 6-dimethyldibenzothiophene; B.C. Gates et al.; Polyhedron **16**, 3213 (1997)

[180] Atomic scale insight into structure and morphology changes of MoS_2 nano-clusters in hydrotreating catalysis; J.V. Lauritsen et al.; Journ. Cat **221**, 550 (2004)

[181] Ab inition DFT stufy of H_2 dissociation on MoS_2, NiMoS and CoMoS: mechanism, kinetics and vibrational frequencies; M. Sun et al.; Journ. Cat. **233**, 411 (2005)

[182] An EXAFS study of the structure of supported cobalt molybdate catalysts as a function of sulfiding temperature; T.G. Parham et al.; J. Cat. **85**, 295 (1984)

[183] The crystal structure of molybdenite; R.G. Dickinson et al.; J. Am. Chem. Soc. **45**, 1466 (1923)

[184] A geometrical model of the active phase of hydrotreating catalysts; S. Kasztelan et al.; Appl. Cat. **13**, 127 (1984)

[185] The transition metal dichalcogenides discussion and interpretation of the observed optical, electrical and structural properties; J.A. Wilson et al.; Adv. in Phys. **18**, 193 (1969)

[186] A symmetry principle for epitaxial rotation; F. Grey et al.; Europhys. Lett. **18**, 717 (1992)

[187] On the catalytic significance of a Co-Mo-S phase in Co-Mo/Al_2O_3 hydrodesulfurization catalysts: combined in situ Mössbauer emission spectroscopy and activity studies; C. Wevel et al.; Journ. of Cat. **68**, 453 (1981)

[188] Structure, energetics and electronic properties of the surface of a promoted MoS_2 catalyst: an ab initio local density functional theory study; P. Raybaud et al.; Journ. Cat. **190**, 128 (2000)

[189] Reactivity studies with gold-supported molybdenum nanoparticles; D.V. Potapenko et al.; Surf. Sci. **574**, 244 (2005)

[190] Surface alloying of immiscible metals: Mo on Au(111) studied by STM; M.M. Biener et al.; Surf. Sci. **594**, 221 (2005)

[191] Interaction of CO, O, and S with metal nanoparticles on Au(111): A theoretical study; Ping Liu et al.; Phys. Rev. B **67**, 155416 (2003)

[192] Density Functional Theory study of CO adsorption on Molybdenum Sulfide; Tao Zeng et al.; J. Phys. Chem. B **109**, 2846 (2005)

[193] Number taken from the website of OICA (Organisation Internationale des Constructeurs d'Automobiles), http://oica.net

Index